
Doctoral Dissertations

Student Theses and Dissertations

Fall 2015

Synthesis and characterization of vanadium oxide nanomaterials

Tyler M. Fears

Follow this and additional works at: https://scholarsmine.mst.edu/doctoral_dissertations

 Part of the [Chemistry Commons](#)

Department: Chemistry

Recommended Citation

Fears, Tyler M., "Synthesis and characterization of vanadium oxide nanomaterials" (2015). *Doctoral Dissertations*. 2443.

https://scholarsmine.mst.edu/doctoral_dissertations/2443

This thesis is brought to you by Scholars' Mine, a service of the Missouri S&T Library and Learning Resources. This work is protected by U. S. Copyright Law. Unauthorized use including reproduction for redistribution requires the permission of the copyright holder. For more information, please contact scholarsmine@mst.edu.

SYNTHESIS AND CHARACTERIZATION OF VANADIUM OXIDE
NANOMATERIALS

by

TYLER MARTIN FEARS

A DISSERTATION

Presented to the Graduate Faculty of the
MISSOURI UNIVERSITY OF SCIENCE AND TECHNOLOGY

In Partial Fulfillment of the Requirements for the Degree

DOCTOR OF PHILOSOPHY

in

CHEMISTRY

2015

Approved by:

Jeffrey G. Winiarz (Co-Advisor)

Nicholas Leventis (Co-Advisor)

Richard Dawes

Chariklia Sotiriou-Leventis

Helmut Kaiser

Haskell Taub

Copyright 2015
Tyler Martin Fears
All Rights Reserved

PUBLICATION DISSERTATION OPTION

This dissertation is prepared in the format of the *Journal of Sol-Gel Science and Technology* (Springer), the *Journal of Power Sources* (Elsevier), and the journal *Physical Chemistry Chemical Physics* (Royal Society of Chemistry). This dissertation includes an article published in the *Journal of Sol-Gel Science and Technology* (Paper I, 32-72), an article published in the *Journal of Power Sources* (Paper II, 73-100), and an article in preparation for submission to the journal *Physical Chemistry Chemical Physics* (Paper III, 101-146).

ABSTRACT

This dissertation focuses on the synthesis and characterization of vanadium oxide nanomaterials and neutron-transparent Li-ion battery electrolytes.

Vanadium oxide gels were synthesized via the epoxide-assisted gelation of VOCl_3 using epichlorohydrin in ethanol. This represents the first epoxide-assisted gelation developed for vanadium oxide gels and serves as a potential economical replacement for the fabrication of vanadium oxide gels via the hydrolysis of vanadium alkoxides. Though epoxide-assisted gelation has been demonstrated for a number of transition metal oxides, the gelation mechanism observed here for VOCl_3 appears to be unique.

While investigating the electrochemical and structural properties of lithium vanadates, it became desirable to perform *in situ* neutron diffraction with electrochemical cycling. The inability to perform these experiments prompted the development of a series of perfluorocarboxylate esters which could potentially serve as neutron-transparent electrolyte solvents and help enable *in situ* neutron scattering characterizations. Electrochemical studies were carried out on Si anodes, and the solid-electrolyte-interphase was studied both *ex situ* and *in situ*. Results indicate that these electrolyte solvents improve neutron scattering data when used in place of standard deuterated carbonates and provide insight into fluorinated components proposed for next-generation electrolytes.

ACKNOWLEDGEMENTS

I would like to thank my advisor Dr. Jeffrey G. Winiarz for his scientific and professional guidance; my co-advisor Dr. Nicholas Leventis for his advice; and my committee members Drs. Chariklia Sotiriou-Leventis, Richard Dawes, Helmut Kaiser, and Haskell Taub for their support. I would also like to thank Dr. Gabriel M. Veith for his mentorship at Oak Ridge National Laboratory and Drs. James F. Browning and Mathieu Doucet on Liquids Reflectometer team at the Spallation Neutron Source for their help collecting and analyzing neutron reflectometry data. I would also like to thank Dr. Rex Gerald III for his help performing NMR experiments. I would also like to acknowledge my lab mates Dr. Jong-Sik Moon and Yichen Liang, as well as the other graduate students, undergraduate students, and support staff in the Chemistry Department, who are too numerous to list.

I would like to thank the various sources that provided student and material support: the Army Research Office (W911NF-14-1-0369), the National Science Foundation through a University of Missouri Neutron Scattering IGERT Traineeship (grant DGE-1069091), the U.S. Department of Energy, Office of Science, Office of Workforce Development for Teachers and Scientists, Office of Science Graduate Student Research (SCGSR) program, administered by the Oak Ridge Institute for Science and Education for the DOE under contract number DE-AC05-06OR23100, the Missouri S&T Materials Research Center, and Bayer Corporation.

Finally, I would like to thank my family for their support, love, and forbearance throughout my undergraduate and graduate careers.

TABLE OF CONTENTS

	Page
PUBLICATION DISSERTATION OPTION	iii
ABSTRACT.....	iv
ACKNOWLEDGEMENTS	v
LIST OF ILLUSTRATIONS.....	x
LIST OF TABLES	xiv
 SECTION	
1. INTRODUCTION	1
1.1 SOL-GEL METHOD.....	1
1.2 PROPERTIES OF VANADIUM OXIDES	5
1.2.1 VO ₂ Metal-to-Insulator Transition.....	6
1.2.2 Li Intercalation.....	8
1.3 IN SITU NEUTRON SCATTERING OF BATTERY MATERIALS.....	10
1.3.1 In situ Neutron Diffraction.....	14
1.3.2 In situ Neutron Reflectometry.	17
BIBLIOGRAPHY.....	23
 PAPER	
I. Economical synthesis of vanadia aerogels via epoxide-assisted gelation of VOCl ₃	31
Abstract.....	31
1 Introduction.....	33

2 Results.....	36
2.1 Gelation.....	36
2.1.1 H ₂ O and Epoxide Optimization	39
2.1.2 Mesophase ¹³ C and ¹ H Nuclear Magnetic Resonance (NMR)	41
2.1.3 Epoxide Ring-Opening in H ₂ O-Free Sols.....	43
2.2 Physical Properties.....	47
2.2.1 Nanomorphology, Surface Area, and Porosity	47
2.2.2 Solvent Trapping and H ₂ O Content	49
3 Discussion.....	51
4 Conclusion	55
5 Experimental Section.....	56
5.1 Aerogel and Xerogel Synthesis.....	56
5.2 Materials Characterization	57
Acknowledgements.....	59
References.....	60
Electronic Supplementary Material	64
II. A study of perfluorocarboxylate ester solvents for lithium ion battery electrolytes	73
ABSTRACT.....	73
1. Introduction.....	75
2. Materials and methods	77

2.1 Perfluorocarboxylate esterification	77
2.2. Si Thin Film Fabrication	79
2.3. Electrochemical Characterization	79
2.4. Ex situ Analysis of Cycled Electrodes	80
3. Results	81
3.1 Ester Physical Properties	81
3.2. Galvanostatic Cycling of Si Anode Half-Cells	83
3.3. ATR-IR of Soluble Electrolyte Decomposition Products	89
3.4. XPS of SEIs Formed on Si Anodes	90
4. Discussion	96
5. Conclusion	97
Acknowledgements	98
References	99
III. Evaluating the solid-electrolyte-interphase formed on silicon electrodes: a comparison of ex situ X-ray photoelectron spectroscopy and in situ neutron reflectometry	101
1. Introduction	102
2. Materials and methods	105
2.1. Perfluorocarboxylic acid esterification	106
2.2. Neutron Scattering Profile	107
2.3. Fabrication of electrochemical cell for in situ NR	108
2.4. In situ electrochemistry and NR	110

2.5. Fitting of NR data	112
2.6. Ex situ characterization.....	112
3. Results.....	114
3.1. Ester physical properties	114
3.2. Comparison of ex situ and in situ electrochemistry.....	117
3.3. Neutron reflectometry	119
3.4. Ex situ XPS	126
3.5. Ex situ NMR	132
4. Discussion.....	135
6. Conclusion	139
Acknowledgements.....	139
References.....	141
Electronic Supplementary Material	143
SECTION	
2. CONCLUSION.....	147
VITA.....	149

LIST OF ILLUSTRATIONS

		Page
Figure 1.1.	H ⁺ -catalyzed epoxide ring-opening in the presence of nucleophilic anions utilized for epoxide-assisted gelation of metal oxides.	4
Figure 1.2.	SEM images showing the unique nanomorphology of alkoxide and VOCl ₃ gels.	5
Figure 1.3.	Optical MIT in undoped and W-doped VO ₂ films.	7
Figure 1.4.	I-V curve for an electrodeposited VO ₂ film showing resistance switching hysteresis.	8
Figure 1.5.	The cycling characteristics of NMC and NMC core-shell cathode materials with accompanying SEM images.	10
Figure 1.6.	Wavelength as a function of kinetic energy for X-rays and neutrons.	12
Figure 1.7.	Graphical representation of the relative scattering cross-sections for selected elements.	13
Figure 1.8.	Growth of Ni/Mn ordered phase with annealing in LiNi _{0.5} Mn _{1.5} O ₄ spinel.	15
Figure 1.9.	In situ neutron diffraction of a commercial Li _a Ni _x Mn _y Co _{1-(x+y)} O ₂ vs. graphite cell.	16
Figure 1.10.	Neutron reflectometry of a stack of poly(styrene sulfonate) and poly(allylamine hydrochloride) made via spin-assisted layer-by-layer deposition with regularly placed deuterated layers to provide contrast.	18
Figure 1.11.	Image and diagram of an in situ electrochemical cell used on Beam Line 4B at the Spallation Neutron Source at Oak Ridge National Laboratory.	20
Figure 1.12.	¹ H NMR of deuterated and protiated ethylene carbonate-dimethylcarbonate electrolytes used for in situ neutron reflectometry.	22
 PAPER I		
Scheme 1	Acid-scavenging mechanism for commonly used epoxides and nucleophilic metal salt anions	35

Scheme 2	Fabrication procedure for vanadia aerogels, polymer-crosslinked vanadia aerogels, and vanadia xerogels.....	38
Fig. 1	Mesophase ^{13}C NMR of a wet-gel before and after aging	42
Fig. 2	Reference peak drift in mesophase ^{13}C NMR during gel aging.	43
Fig. 3	^1H NMR of H_2O -free sols shows the inductive effect of V^{V} and exchange broadening in $\text{EtO}^- \text{-V}^{\text{V}}$ chelates and ECH ring-opening in the absence of H_2O and H^+	44
Scheme 3	Formation of 5-coordinate VOCl_3 adducts of EtOH and ECH, $\text{Cl}^- \leftrightarrow \text{EtO}^-$ ligand exchange, and Lewis acid-catalyzed intramolecular epoxide ring-opening in the absence of free Cl^- in CCl_4 observed via ^1H NMR in H_2O -free sols.....	46
Fig. 4	Representative SEM and TEM images of VO_x aerogels.....	47
Fig. 5	N_2 -sorption isotherms for a VO_x xerogel, VO_x aerogel, and X- VO_x aerogel	49
Fig. 6	TGA-MS results for vanadia aerogels and xerogels.....	51
Scheme 4	Proposed reaction mechanism for gelation in the VOCl_3 -ECH-EtOH system involving ligand exchange in EtOH; Lewis-acid-catalyzed ECH ring-opening; neutral 4-, 5-, and 6-coordinate species potentially formed during additional ligand exchange; and a possible mechanism for the polymerization of vanadium oxide via ololation of a 5-coordinate vanadyl hydroxide.....	54
Figure S.1	UV-Vis absorption spectra comparing several VOCl_3 solutions and a wet gel, assuming a 25 μm path length.....	65
Figure S.2	UV-Vis absorption spectra of standard epoxide gel during aging, assuming a 25 μm path length.	66
Figure S.3	Concentration of ECH, MCPDH ₂ , MCEPH and their Sum as a function of time as monitored by ^{13}C NMR	67
Figure S.4	X-ray diffraction pattern of a ground vanadia aerogel monolith.....	68
Figure S.5	Conformally coated cylindrical VO_x nanoworm approximation used to calculate polymer coating density.....	69
Figure S.6	Representative quasi-static compression tests of X- VO_x aerogels with different densities, as controlled by isocyanate concentration in crosslinking solutions	70

Figure S.7	MS signals between $m/z = 15$ and $m/z = 300$ above the detection limit for vanadia aerogels and vanadia xerogels	71
------------	---	----

PAPER II

Fig. 1.	Perfluorocarboxylate esters investigated in this work.....	76
Scheme 1.	Esterification of perfluoroglutaric acid to form dimethyl perfluoroglutarate.	78
Fig. 2.	Electrochemical cycling results on Si thin film electrodes.	85
Fig. 3.	Capacity fade in Si thin film electrodes.	87
Fig. 4.	IR absorption spectra of the PF5M ₂ electrolyte before and after 500 cycles at C/5.	89
Scheme 2.	Electrochemical de-esterification of PF5M ₂	90
Fig. 5.	High-resolution XPS of lithiated Si electrodes.	91
Fig. 6.	High-resolution XPS and atomic fractions of Si electrodes cycled with 0.1 M LiTFSI in PF5M ₂ at the various SOCs shown in Fig. 7.....	93
Fig. 7.	Differential capacity curve with SOCs labeled for XPS data.....	94
Scheme 3.	Electrochemical defluorination of lithium perfluoroglutarate.....	95

PAPER III

Fig. 1	d ₃ -methyl perfluorocarboxylate esters investigated as electrolyte solvents in this study.	105
Scheme 1	Esterification of perfluorobutyric acid to form methyl perfluorobutyrate.	106
Fig. 2	Experimental geometry for collecting NR data.....	110
Fig. 3	Calculated total neutron scattering coefficients and measured neutron scattering profiles for selected electrolyte solvents.....	116
Fig. 4	Differential capacity curve for the first cycle of a Si thin-film half-cell used for ex situ analysis.....	118
Fig. 5	Electrochemical data for in situ NR cell.....	119
Fig. 6	NR data and fits in order of collection.	120

Fig. 7	SLD profiles representing the tabulated fit parameters.....	122
Fig. 8	Potential relaxation and relaxation rate for in situ NR and coin cells stopped at various potentials.	124
Fig. 9	Ex situ Si 2p XPS spectra used to calculate SEI thickness using Eq. 5.....	129
Fig. 10	Atomic compositions of the SEI determined from XPS and used to estimate SLD.	131
Fig. 11	^1H , ^7Li , ^{13}C , and ^{19}F NMR spectra of deuterated and protiated electrolytes before and after cycling.....	133
Fig. 12	SEI thickness and SLD as determined via ex situ XPS and in situ NR.....	136
Fig. S1	High-Q NR data before background subtraction.....	144

LIST OF TABLES

	Page
PAPER I	
Table 1	Results of attempts to fabricate gels at different sol concentrations37
Table 2	Gel quality and gelation time as a function of H ₂ O content and epoxide functionality.....40
Table 3	Physical properties of VO _x and X-VO _x gels.....49
PAPER II	
Table 1.	Electrolyte conductivity as determined by impedance spectroscopy.82
PAPER III	
Table 1	Results of NR fits for electrochemically active components.126
Table 2	Layer thicknesses derived from ex situ XPS.....130
Table S1	Multilayer parameters determined from NR fits.145

1. INTRODUCTION

Like many other transition metal oxides, vanadium oxides possess useful optical,¹⁻
¹¹ electronic,^{1, 2, 12-21} magnetic,^{1, 21-23} and catalytic properties.²⁴⁻²⁷ The redox activity and
typically lamellar molecular structures of crystalline and amorphous vanadium oxides
also makes these materials useful as intercalation cathodes for Li-ion batteries.^{12, 28-39}

Physical vapor deposition (PVD),^{1, 2, 15, 26, 29, 40} chemical vapor deposition
(CVD),^{1, 15} atmospheric pressure chemical vapor deposition (APCVD)^{5, 7, 15, 30} and
electrochemical deposition^{19, 30} are all frequently used to deposit vanadium oxide films.
However, the most effective method for fabricating monolithic structures is the sol-gel
method, a well-studied, versatile technique that has been shown to be effective for
numerous transition metal oxides.⁴¹ This method is well-suited for device fabrication of
many geometries, especially those that require high porosity or surface area.^{1, 3, 4, 6, 9, 12, 18,}
^{20, 27, 32-34, 38, 39, 42-52}

The synthesis of vanadium oxide nanomaterials using sol-gel techniques is
discussed, including synthetic mechanisms and properties of the fabricated samples.
Additional attention will be placed on the development and characterization of neutron-
transparent Li-ion battery electrolytes and the relationship between that work and
vanadium oxide nanomaterials.

1.1 SOL-GEL METHOD

The sol-gel technique is typified by sequential hydrolysis and condensation
steps.⁵³ There are several methods for fabricating vanadium oxide (VO_x) gels,^{42, 48}
including oxide hydrolysis,¹⁸ peroxide-assisted hydrolysis,^{46, 49} cation-exchange,^{4, 32, 47, 50}
and alkoxide hydrolysis.^{3, 12, 20, 31, 33, 44, 51, 52} Variations on these techniques also exist

which utilize templating⁵⁰ and chelating agents.⁶ All of these techniques proceed through the formation of acidic polyvanadates (e.g. $V_{10}O_{28}^{6-}$, $V_6O_{16}^{2-}$, etc.) in solution followed by aggregation into a space-filling gel. The strong anisotropy of polyvanadates leads to fibrous gel morphologies, dissimilar from many inorganic sol-gels, which are typified by random aggregates of spherical particles.⁴¹

The first step in the oxide hydrolysis method is the formation of soluble metal oxide hydrates from vanadium oxide, which speciate as a number of polyvanadates in aqueous solution. This method is employed by quenching molten V_2O_5 (ca. 900 °C) in distilled H_2O , forming a gel on the order of hours to days. It has also been noted that crystalline V_2O_5 powders slowly dissolve in distilled water over the course of weeks to form solutions which undergo gelation through the same process over much longer time periods.^{12, 42, 48}

Peroxide-assisted hydrolysis takes advantage of the chelating power of the peroxide anion (O_2^{2-}). In the presence of aqueous hydrogen peroxide, crystalline V_2O_5 powder forms soluble, metastable vanadium oxy-peroxides, of which several have been identified: $VO(O_2)(H_2O)_3^+$, $VO(O_2)_2(H_2O)_2^-$, $[VO(O_2)_2]_2O(H_2O)_2^{4+}$, and $(O_2)_2OVOVO_2(O_2)^{4+}$ which can take on varying degrees of protonation.⁴⁶ The particular speciation in solution is a function of H^+ , V^V , and O_2^{2-} concentration. As the peroxides decay, forming O_2 and H_2O , polyvanadates are formed, which undergo gelation in the same manner as previously described.^{45, 46, 48, 49}

$NaVO_3$ is the soluble, alkaline vanadate most commonly used in the cation exchange method. A $NaVO_3$ solution is passed through a cation exchange column to acidify the solution and remove unwanted Na^+ ions. The acidified solution undergoes

polymerization and gelation as previously described. In some cases, incomplete ion-exchange is desirable, forming $\text{Na}_{2x}\text{V}_3\text{O}_{8-x}$ ($0 \leq x \leq 0.5$) gels. Similarly, direct acidification of NH_4VO_3 —another soluble, alkaline vanadate—in aqueous solutions leads to gelation.^{4, 32, 39, 42, 47, 48}

Unlike the previous syntheses, the alkoxide method takes place in non-aqueous media, as metal alkoxides are prone to rapid hydrolysis, forming flocculates or precipitates instead, if added directly to H_2O . Vanadia gels are commonly made in acetone with controlled concentrations of H_2O and $\text{VO}(\text{OR})_3$ species (typically vanadium oxytripropoxide or vanadium oxytriisopropoxide). The exothermic nature and speed of hydrolysis necessitates performing the gelation at a reduced temperature, i.e. using a dry ice/acetone bath. The presence of organic species during gelation causes some $\text{V}^{\text{V}} \rightarrow \text{V}^{\text{IV}}$ (red/yellow \rightarrow blue) reduction, which is apparent in the final gel coloration (green). Some alkoxide-derived gels also have a distinct nanomorphology intermediate between the random spherical aggregates of silica gels and monofilament fibers of other vanadium gels, the cause of which has not been investigated.^{1, 3, 4, 31, 33, 39, 51, 52}

Recently, following a trend in other transition metal oxides,^{41, 54} an epoxide-assisted gelation method has been developed for the fabrication of sol-gel vanadium oxides. In this method, acidic hydrated metal salts (typically chlorides or nitrates) protonate the epoxide ring, enabling irreversible ring-opening by nucleophilic anions. This process consumes H^+ and gradually raises the pH of the solution, uniformly inducing gelation (Figure 1.1).⁵⁴

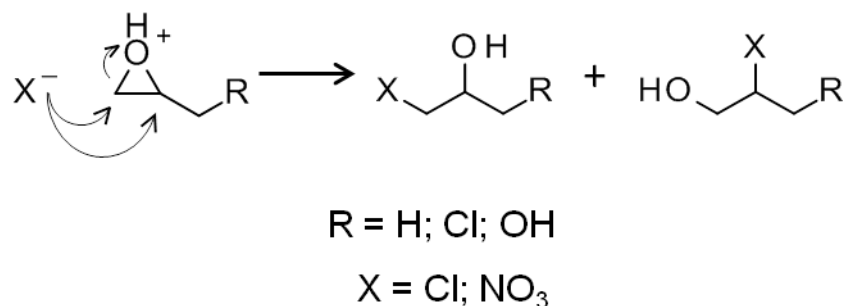


Figure 1.1. H^+ -catalyzed epoxide ring-opening in the presence of nucleophilic anions utilized for epoxide-assisted gelation of metal oxides.

The primary advantage of epoxide-assisted gelation is cost. Aside from a few examples (Si, Ti, Al), transition metal alkoxides are prohibitively expensive or commercially unavailable; whereas their chlorides and nitrates are comparatively inexpensive. The two most common epoxides used are propylene oxide (PPO) and epichlorohydrin (ECH), which are inexpensive and have reactivities which differ sufficiently for useful control over gelation rates. Though this procedure has been developed for a large number of metal oxide systems, the epoxide-assisted gelation of vanadia had been notably unobserved before this work.⁵⁵

An additional advantage of the epoxide method over the alkoxide method is the stability of the precursors. Vanadium oxytriisopropoxide ($VO(O^iPr)_3$), a commonly used vanadium alkoxide, and $VOCl_3$, used in the epoxide method, are both prone to hydrolysis from ambient moisture; however, while the alkoxide forms solid precipitates, the acid chloride forms soluble hydrates, especially stable in alcoholic or ethereal solutions, until the addition of the epoxide. It was also noted that, while the nanomorphology of gels fabricated in-house using the alkoxide and epoxide methods were nominally equivalent

(Figure 1.2), the gels fabricated through the epoxide method were of a superior optical quality (glassy) and significantly sturdier.

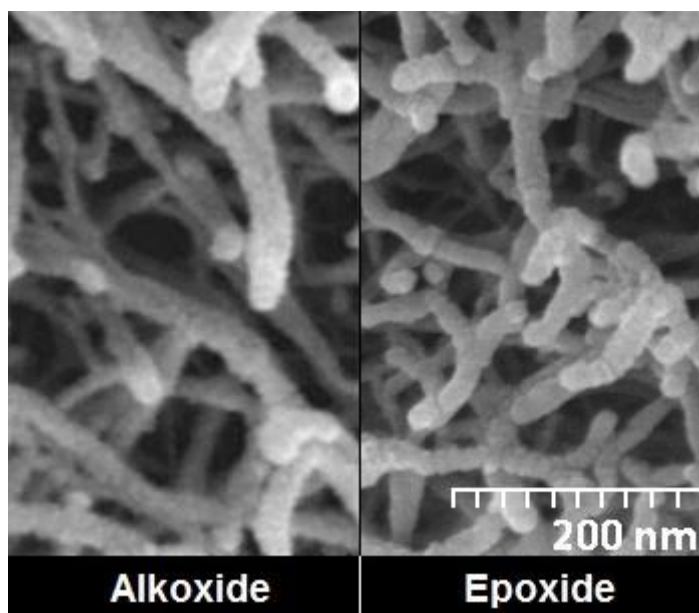


Figure 1.2. SEM images showing the unique nanomorphology of alkoxide⁵¹ and VOCl_3 gels.

1.2 PROPERTIES OF VANADIUM OXIDES

Like many transition metal oxides, vanadium(III, IV, and V) oxides have interesting properties as catalytic^{25, 27, 56} and magnetic materials;^{1, 15, 21, 22} however, those properties and applications will not be discussed here. Instead, two properties of recent interest with immediately apparent commercial application will serve as the motivation for the fabrication of functional vanadium oxide devices: the metal-insulator transition (MIT) of VO_2 and Li-intercalation properties of numerous vanadium oxide phases.

1.2.1 VO₂ Metal-to-Insulator Transition. The MIT of V₂O₃ and VO₂ have been known for half a century.¹³ This transition is characterized by a subtle structural transformation and conductivity change that covers several orders of magnitude and occurs at a well-defined temperature. These and several intermediate vanadium oxides—and a number of other transition metal oxides—possess this property,²¹ but VO₂ is of the most practical importance, as its 68 °C transition is closest by far to ambient temperatures, meaning that it is more easily accessible. This transition can be induced thermally, optically, or electrically, and the efficiency of any device utilizing such interactions is limited in part by the energy input required to induce the transition, which is minimized by transitions which take place near the operating temperature.^{16, 17} It is preferable to operate any device at ambient temperatures, as opposed to liquid N₂ or He temperatures, which are common in the laboratory but difficult to achieve in consumer products.

One recent commercial foray that utilizes the MIT of VO₂ is the development of energy-efficient thermochromic window coatings.^{7, 9-11} Accompanying the MIT is a—predictably—significant change in the optical properties of VO₂. Specifically, the reflectivity of VO₂ in the infrared (IR) region is significantly increased in the high-temperature, metallic phase (Figure 1.3). Using this property, coated windows allow most solar energy to pass when below the transition temperature and reflect a large portion of the radiation when above the transition temperature, creating a passive temperature mediation device. Since humans prefer temperatures below 68 °C, dopants (typically W) are used to lower the transition temperature.¹¹

The MIT in VO_2 can also be utilized in optical limiters and shutters. Optical limiters are used to protect sensors from saturating or becoming damaged by intensities above the dynamic range of devices. VO_2 (IR) limiters work by increasing their reflectivity—as opposed to absorption—at high incident intensity. The speed of this transition (~ 0.5 ps) also makes VO_2 ideal for high-speed optical shutters in which a high-intensity visible writing beam induces the transition and an IR beam reads the state. These optical shutters are of interest as elements in all-optical digital logic devices.^{2, 17}

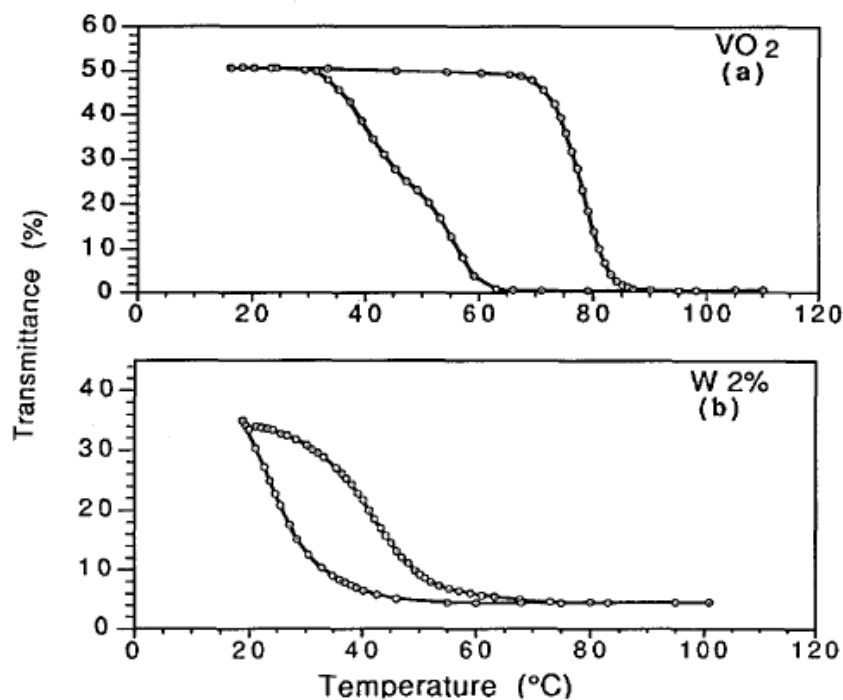


Figure 1.3. Optical MIT in undoped (a) and W-doped (b) VO_2 films. Reproduced from literature.⁴

Electronic logic gates are built on discontinuous changes in conductivity. In current transistor technologies, this is done by modifying the carrier density in a semiconductor contact using a gate voltage, but any material or device geometry which

can reliably alter its conductivity by a significant amount is compatible with current logic architectures. Resistance switching in VO_2 (Figure 1.4) represents one possible mechanism for such devices.¹⁹

Despite the fact that the MIT in VO_2 has been known and studied for over 60 years, the exact nature of the transition is still under debate.^{17, 21} One important contested aspect in optically- and electrically-induced transitions is whether the transition is truly field-induced, as seen in gated Si-based microelectronics, or thermally-induced by local heating from optical absorption and joule heating, respectively.^{2, 17, 19}

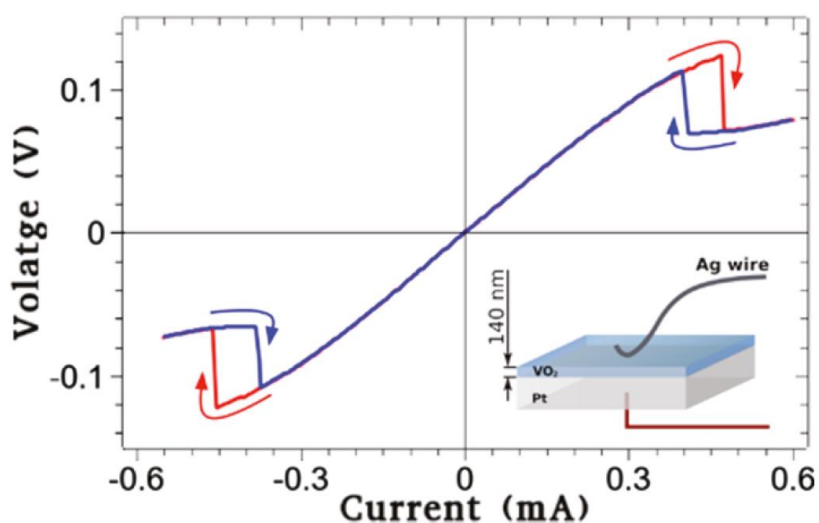


Figure 1.4. I - V curve for an electrodeposited VO_2 film showing resistance switching hysteresis. Reproduced from literature.¹⁹

1.2.2 Li Intercalation. Vanadium oxides have been studied as potential Li-intercalation cathodes. They operate in a reasonable voltage range (1.5-3.5 V vs. Li) and possess high theoretical capacities. Unfortunately, these materials typically exhibit unacceptably poor cycling lifetimes.^{28, 35, 57} Recent studies on nanostructured materials suggest that improvements in cycling fade are possible, suggesting that vanadium oxide materials may be made commercially viable.⁵⁸⁻⁶⁰

Initial efforts focused on $\text{Li}_2\text{V}_6\text{O}_{13}$,³⁵ which has the fortuitous property of metallic conductivity (most intercalation cathodes have poor conductivity, increasing internal resistance at the interface of the cathode and current-collector). However, conductivity decreases with Li insertion and the material does not possess a satisfactory cycling lifetime. Other investigated vanadates (LiV_3O_8 , V_2O_5 , $\text{VO}_2(\text{B})$) also possess poor cycling lifetimes,⁶¹ but studies with nanoparticulate and amorphous vanadates show improved cycling characteristics.^{30-34, 37, 39, 61}

Using nanostructured materials to improve the performance of electrode materials has been proven effective in other systems, including commercially successful materials. LiFePO_4 only became commercially viable after coating the insulating nanocrystals with a conductive carbon coating, greatly improving power density.⁵⁹ $\text{LiNi}_\alpha\text{Mn}_\beta\text{Co}_\gamma\text{O}_2$ (NMC) cathode materials have differing properties depending on their transition metal ratio: a composition which possesses high capacity tends to suffer from degradation at the electrolyte interface, while a lower-capacity composition possesses excellent stability towards the electrolyte. By coating the high-capacity material with a low-capacity material shell, the desired properties of both materials were obtained (Figure 1.5).⁵⁸ AlF_3 and TiO_2 have also been investigated as coatings for surface passivation to improve the cycling characteristics of MnO_2 cathode materials.⁵⁹ Si anodes possess a much higher capacity than graphite anodes, but undergo massive expansion (ca. 300%), leading to extreme strain and fracture during Li insertion. Nanoparticles have inherent resistance to strain fracture, making them ideal for systems plagued by strain fracture, explaining the interest in Si nanowire anodes.⁶⁰

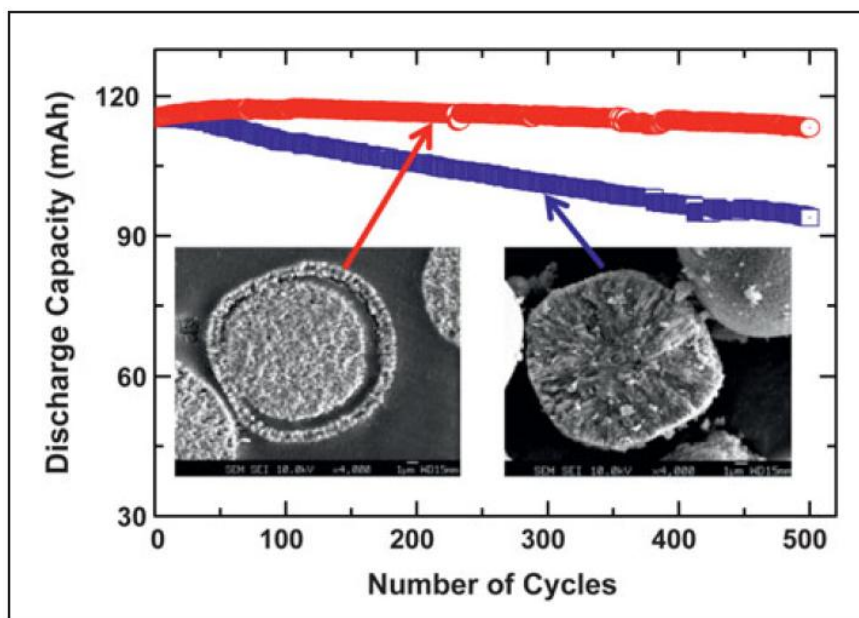


Figure 1.5. The cycling characteristics of NMC (blue) and NMC core-shell (red) cathode materials with accompanying SEM images. Reproduced from literature.⁵⁸

While vanadate cathode materials suffer from poor cycling characteristics, attributed primarily to strain during Li insertion and extraction, their favorable comparisons to commercial cathodes (LiVO_2 - LiCoO_2)—and the potential for very high charge capacity in some cases—cause them to remain subjects of interest. Advances in nanostructured and composite electrode materials suggest that capacity fade in vanadates can be mitigated.

1.3 *IN SITU* NEUTRON SCATTERING OF BATTERY MATERIALS

X-ray scattering and neutron scattering occupy much of the same theoretical domain and can be treated using similar mathematical formalisms, the details of which are covered in detail in other texts.⁶²⁻⁶⁸ While numerous X-ray and neutron scattering techniques are routinely applied in a wide variety of fields, this discussion will focus on

those aspects which differentiate X-ray and neutron scattering and are relevant to the analysis of battery electrodes and interfaces.

There are four practical differences between X-ray scattering and neutron scattering.^{65, 69} (1) The mass of the neutron means that much lower energies are necessary to reach wavelengths on the order of chemical bonds when compared to X-rays (Figure 1.6). This facilitates the investigation of low-energy inelastic phenomena such as molecular diffusion and phonon excitation. (2) Neutrons scatter from atomic nuclei via the (relatively weak) strong force. Since this interaction is isotope dependent, isotopic doping can be used to distinguish between otherwise indistinguishable chemical environments. (3) Neutrons are spin-1/2 particles and can be used to investigate magnetic phenomena. (4) Neutrons can only be produced in significant quantities at dedicated facilities which are $\sim 10^5$ times dimmer than common laboratory X-ray sources. Of these differences, the nuclear scattering dependence (2) and low intensity of neutron sources (4) affect the study of battery materials most.

The weak interaction of neutrons with matter means that they penetrate materials more easily than X-rays and are well-suited for non-destructive characterization of assembled devices. Unfortunately, this also means that large samples are required to obtain data at a comparable rate (additionally complicated by the low brightness of neutron sources).

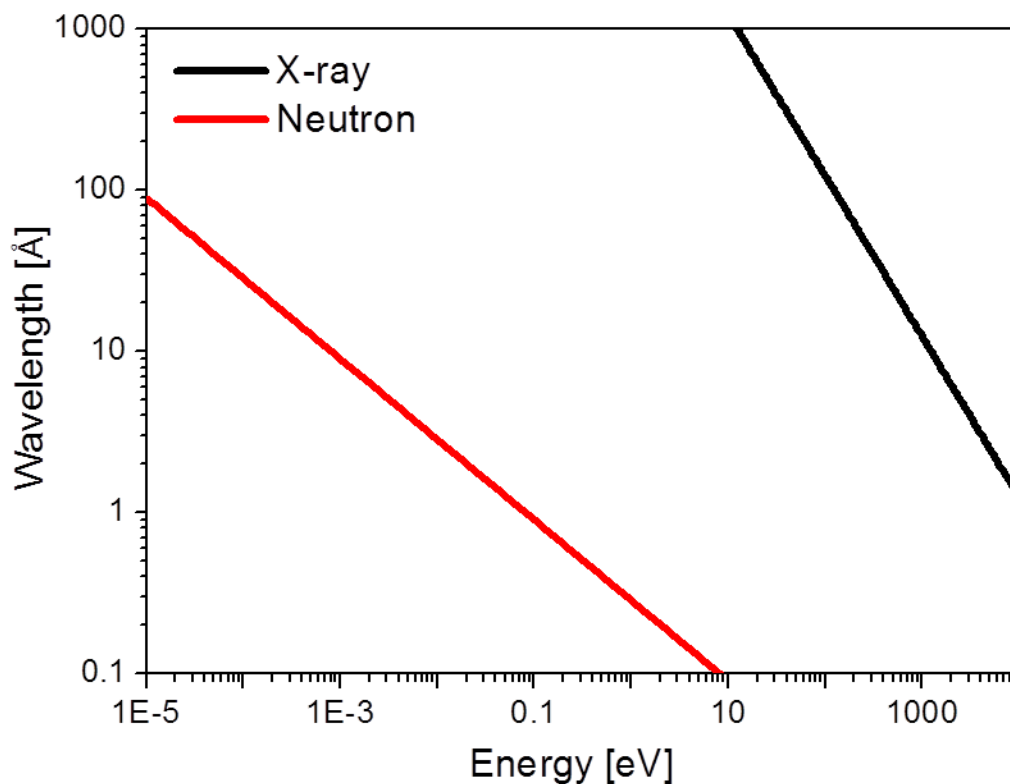


Figure 1.6. Wavelength as a function of kinetic energy for X-rays and neutrons.

Coherent X-ray scattering cross-sections scale approximately with the square of the atomic number ($\sigma_{\text{coh}} \propto Z^2$), so heavy atoms dominate scattering events and atoms of similar Z are difficult to differentiate. Neutron scattering cross-sections do not obey a similarly simple trend (Figure 1.7). As a result, neutrons are much more sensitive to light elements and are often able to differentiate between elements of similar Z .^{62, 65} Additionally, since neutron scattering cross-sections are isotope-dependent, isotopic substitution can provide contrast to chemically or physically distinct features which are otherwise atomically indistinguishable. While X-ray scattering form factors are always positive ($f \propto \sigma_{\text{coh}}^{1/2} > 0$), neutron scattering lengths can be positive or negative ($b \propto \pm\sigma_{\text{coh}}^{1/2}$).⁶⁹ Positive and negative scattering lengths can provide contrast for nuclei with

similar scattering cross-sections or suppress scattering from specific features through isotopic substitution and contrast matching.

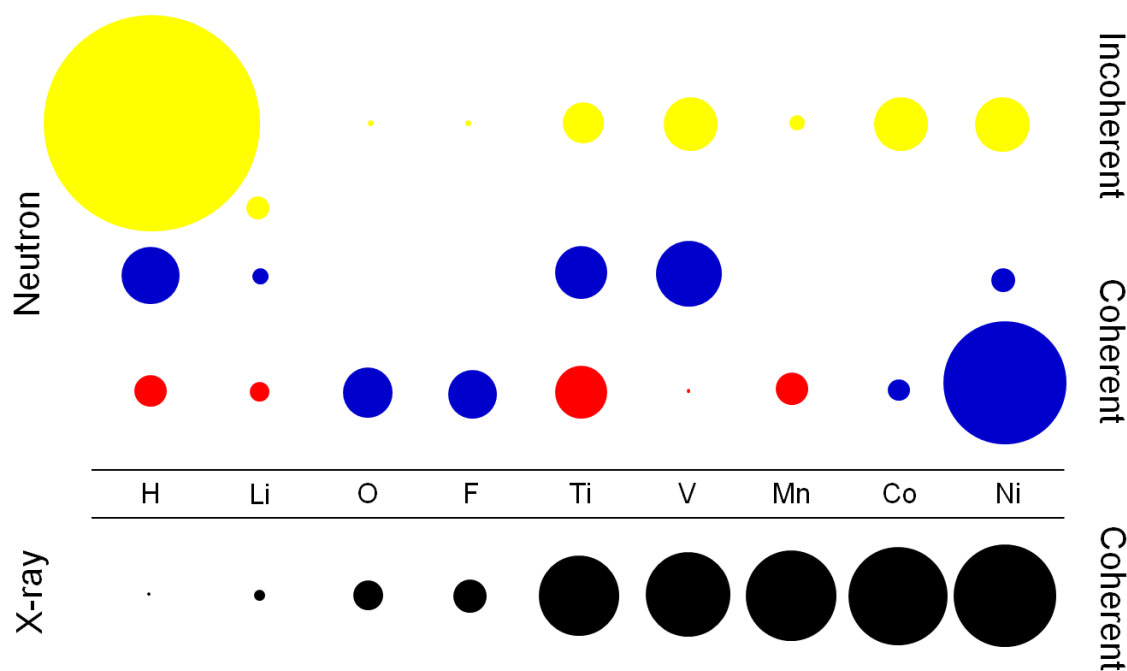


Figure 1.7. Graphical representation of the relative scattering cross-sections for selected elements. Coherent neutron cross-sections are shown for relevant primary (bottom) and secondary (top) isotopes with positive (blue) and negative (red) scattering lengths. (F, Mn, and Co only have a single stable isotope and O isotopes do not have sufficiently different scattering lengths for practical use.) Incoherent scattering cross-sections (yellow) are shown for elements at their natural isotopic abundance.⁶⁹

The primary barrier to performing neutron scattering experiments is the availability of sufficiently luminous sources. Neutron production requires significant infrastructure, e.g., a reactor or accelerator, which is not economically feasible for a typical research group. Even then, sources are typically orders of magnitude less luminous than common laboratory X-ray sources.⁶⁵ This limitation means that neutrons are extremely expensive to produce and must be utilized efficiently. This concern is especially important in *in situ* studies, where material not of interest is often in the

neutron beam, attenuating signal and increasing background, and *in situ* sample modification consumes precious instrument time.

The most common source of interference in neutron scattering experiments is ancillary sources of ^1H in the form of organic material and H_2O . ^1H possesses an enormous incoherent scattering cross-section (Figure 1.7), making it an excellent moderator and radiation shielding component but a serious inconvenience in experimental apparatuses and methodologies. Isotopic (^2H) substitution is common and typically sufficient to enable successful data collection; however, it is not always possible nor desirable.^{62, 64-68, 70-73}

1.3.1 *In situ* Neutron Diffraction. Powder neutron diffraction is the most common neutron scattering technique applied to battery materials.^{64, 70-74} Li sensitivity and transition metal contrast make neutron diffraction ideal for studying these materials, especially cathodes. In particular, powder neutron diffraction has been used to observe Li diffusion pathways in LiFePO_4 ⁷⁵ and Ni/Mn ordering in $\text{LiNi}_{0.5}\text{Mn}_{1.5}\text{O}_4$ cathodes (Figure 1.8),⁷⁶ measurements that are not possible with traditional X-ray diffraction. Given the importance of these structural details in the performance of the materials during cycling, neutron diffraction is an integral tool for understanding and developing state-of-the-art devices.

Typically, neutron diffraction is performed on battery materials as-synthesized. Analysis of cycled materials is carried out by collecting material from electrochemical cells after performing the desired lithiation and delithiation reactions.^{70, 73, 76, 77} Ideally, these diffraction experiments would be performed on materials *in situ*, allowing for the study of dynamic structural changes and the collection of multiple states of charge

without extraction from the electrochemical cell, avoiding the potential for sample contamination.

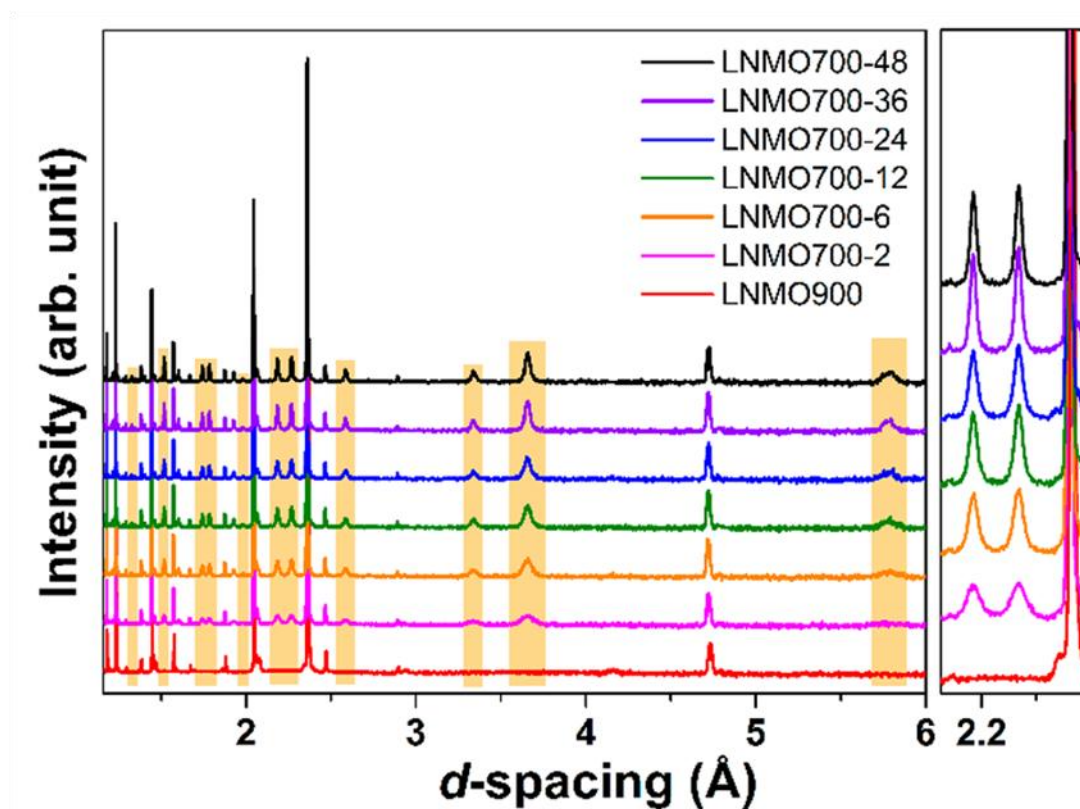


Figure 1.8. Growth of Ni/Mn ordered phase with annealing in $\text{LiNi}_{0.5}\text{Mn}_{1.5}\text{O}_4$ spinel. Peaks due to ordered phase are highlighted in orange. Reproduced from literature.⁷⁶

Neutron diffraction measurements have successfully been performed using specially-designed *in situ* electrochemical cells.^{64, 66, 70, 71, 74} As would be expected, the necessary inclusion of organic components (electrolyte, separator, packaging) significantly impede the collection of high-quality diffraction patterns. Using deuterated electrolytes and replacing other organic components with inorganic components allowed for the collection of full diffraction patterns with *in situ* electrochemical cycling. Diffraction experiments have also been performed on commercial cells with common,

protiated components by limiting Q -space ($Q = 2\pi/d$, where d is the spacing for particular reflection) to obtain sufficient statistics (Figure 1.9).⁷⁸

The development of methodologies for collecting full high-quality diffraction patterns of Li-ion battery materials in *in situ* electrochemical cells is ongoing.

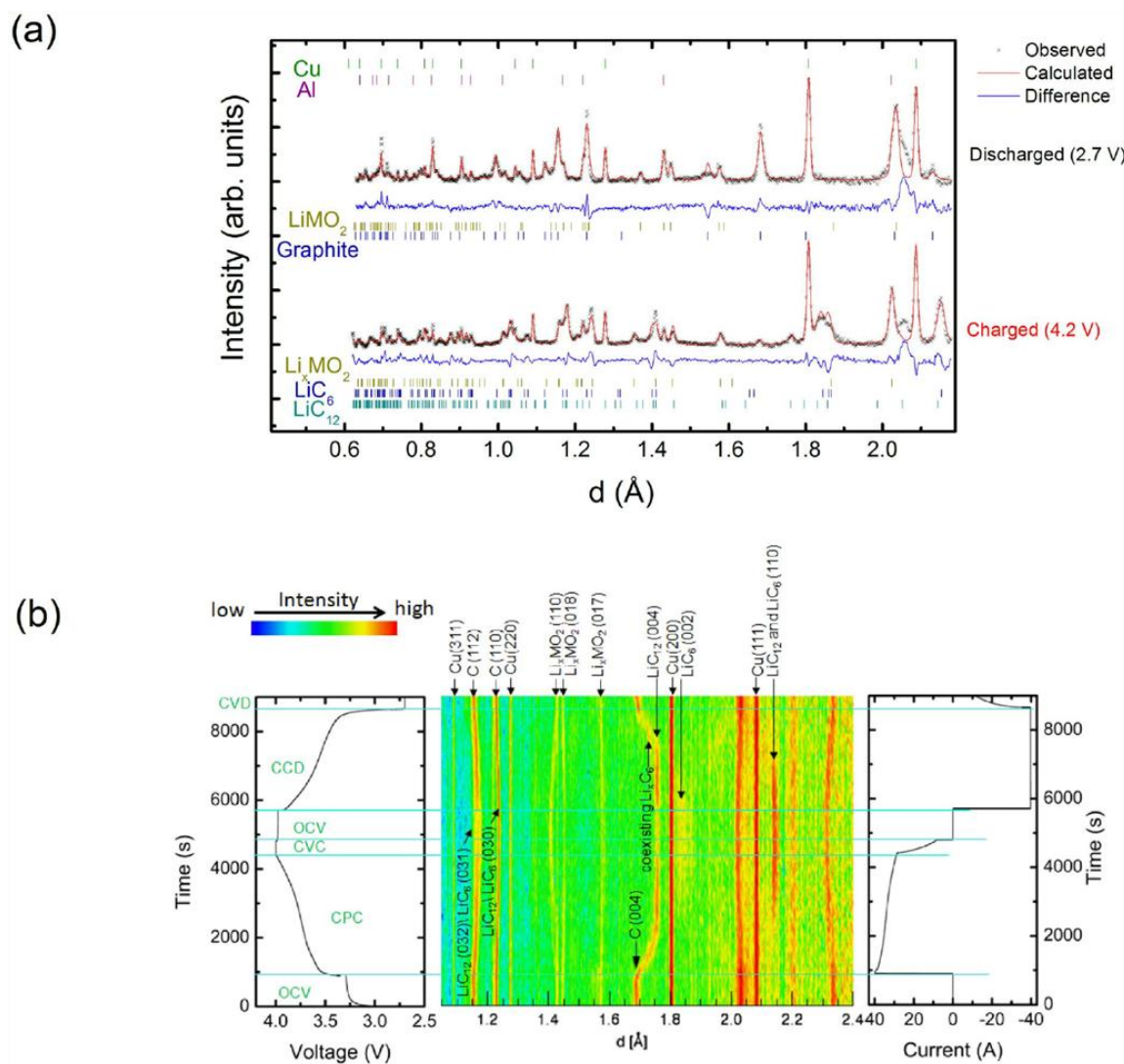


Figure 1.9. *In situ* neutron diffraction of a commercial $\text{Li}_x\text{Ni}_y\text{Mn}_z\text{Co}_{1-(x+y)}\text{O}_2$ vs. graphite cell. Long (1 h) scans of the cell in the charged and discharged state (a) and in-operando diffraction data of the cell during charging and discharging (b). Reproduced from literature.⁷⁸

1.3.2 *In situ* Neutron Reflectometry. While *in situ* neutron diffraction is used to study changes in crystalline and molecular structures with electrochemical cycling, *in situ* neutron reflectometry probes the composition and thickness of electrode interfaces. The neutron reflectivity of a sample is given by:

$$R(Q) = \frac{(4\pi)^2}{Q^4} \left| \int_{-\infty}^{\infty} \frac{d\beta}{dz} e^{iQz} dz \right|^2 \quad (1)$$

where R is the reflectivity of the surface, Q is the magnitude of the neutron wavevector (momentum) transfer, β is the scattering length density (SLD) of the material averaged over the two-dimensional sampling footprint, and z is the direction normal to the surface. SLD is determined by the atomic density and composition of the material,

$$\beta = \sum_a N_{d,a} b_a = N_A M_d \sum_a \chi_a b_a \quad (2)$$

where $N_{d,a}$ is the number density of atom a , b_a is the coherent scattering length of atom a , N_A is Avagadro's number, M_d is the average atomic molar density of the material, and χ_a is the atomic fraction of atom a . SLD is analogous to refractive index, although total reflection occurs at low angles when passing from low SLD to high SLD, the opposite of refractive index.^{62, 65, 79}

The SLD profile along z is determined by fitting experimental profiles to theoretical curves, e.g., using least-squares fits. Uniform layers with sharp interfaces and

large differences in SLD result in well-defined interference fringes. In practice though, each interface has some roughness, and samples with multiple layers that have small differences in SLD (low contrast) can lead to complicated reflectivity patterns which cannot be uniquely fit. Therefore, it is useful to carefully design cells with internal standards and a minimal number of layers with high contrast.^{68, 79, 80}

Isotopic (^1H , ^2H) substitution in layer-by-layer polymer films is the prototypical example as monolayer deposition is relatively simple and ^1H and ^2H have scattering lengths of -3.74 fm and 6.67 fm, respectively, providing large contrast (Figure 1.10).^{62, 69,}

81

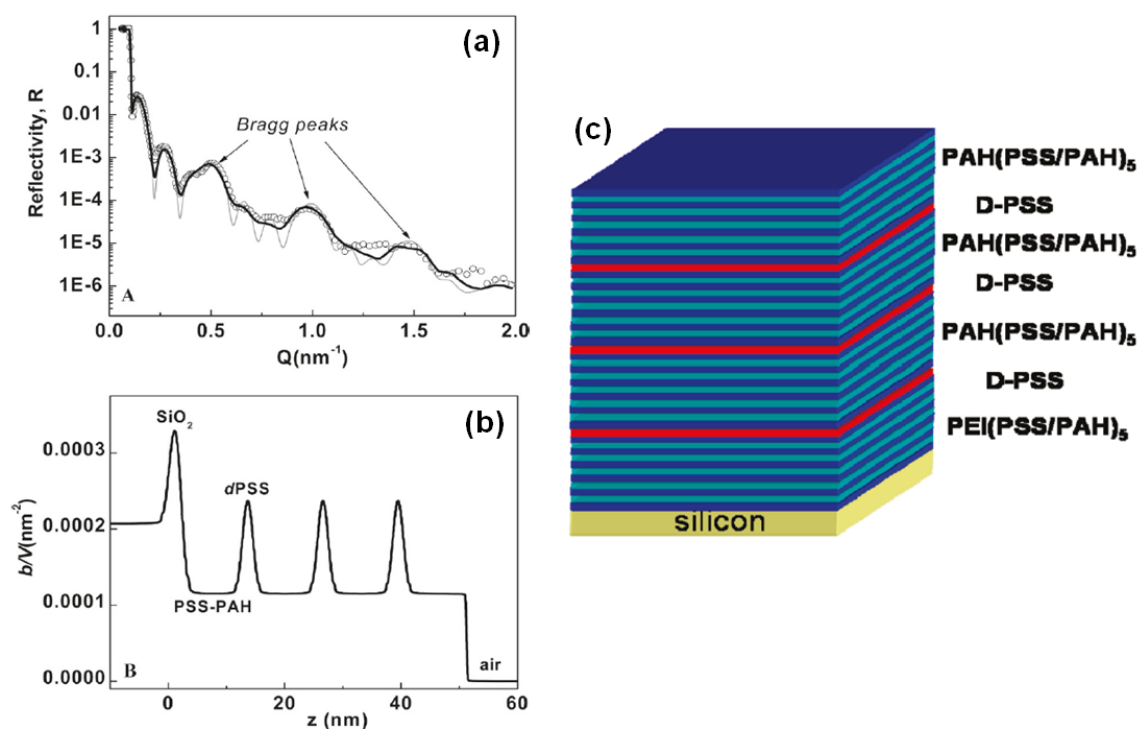


Figure 1.10. Neutron reflectometry of a stack of poly(styrene sulfonate) (PSS) and poly(allylamine hydrochloride) (PAH) made via spin-assisted layer-by-layer deposition with regularly placed deuterated layers to provide contrast. Neutron reflectivity profile with fits (a), SLD profile for best fit (b), and diagram of the layered polymers (c). Reproduced from literature.⁸¹

Thin-film Li-ion batteries for neutron reflectometry are composed of four layers at the investigated electrode: sequentially, a smooth, flat structural support, e.g., single crystal Si; a current collector; the active intercalation material; and the electrolyte. During cycling, a fourth layer forms at the electrode-electrolyte interface, known as a solid-electrolyte-interphase (SEI). This SEI plays an integral role in cell performance and cycling lifetime. *In situ* neutron reflectometry is a non-destructive method that can probe compositional changes in both the electrode and SEI along with swelling and growth during electrochemical cycling.

Since Si has a small incoherent scattering cross-section and data is collected below the diffraction condition for Si, using the Si as the incident medium (fronting) in *in situ* electrochemical cells is preferred to using the electrolyte, which, even when deuterated, has a significant incoherent scattering cross-section, leading to a high background signal. Using the Si as the incident medium also means that data of a reasonable quality can be collected even with a protiated electrolyte, as the neutron beam does not pass through the protiated material, unlike in *in situ* diffraction cells.⁷⁹ This allows for greater experimental flexibility, such as isotopically ($^1\text{H}\rightarrow^2\text{H}$) doping specific electrolyte components to study which species incorporate into the SEI.

The design of a neutron reflectometry experiment involves maximizing contrast between layers while minimizing both background signal, e.g., incoherent scatter from ^1H , and fitting parameters, i.e., the number of undefined layers. It is necessary to identify the most important parameters, as it is often not possible to simultaneously optimize all parameters. For example, when investigating thin layers, high- Q data is required; since signal intensity falls off rapidly with increasing Q ($R(Q) \propto Q^{-4}$), it is necessary to

prioritize a low background intensity. Preliminary optimization of layer thickness is also desirable; layer thicknesses outside the 1-100 nm range are more difficult to model, as are layers of similar thickness (overlapping interference fringes).

An example of an *in situ* neutron cell used to investigate SEI growth on a Si anode, used on Beam Line 4B at the Spallation Neutron Source at Oak Ridge National Lab, is shown in Figure 1.11.^{68, 79, 80} The Cu current collector is impermeable to Li, serving as a layer of constant thickness and SLD to aid in fitting and preventing lithiation of the Si substrate. The Si and Cu thicknesses were chosen to prevent the overlap of interference fringes. Polycrystalline $\text{Ti}_{0.68}\text{Zr}_{0.32}$ was chosen as the current collector for the counter/reference electrode, as it is machinable, chemically inert, does not alloy with Li, and is a null scatterer, meaning that it scatters only incoherently and will not result in aberrant signals in the reflectivity data. The working and counter/reference electrodes are separated by a relatively large distance (0.1-0.5 mm) to prevent electrical shorting in the absence of a porous separator.

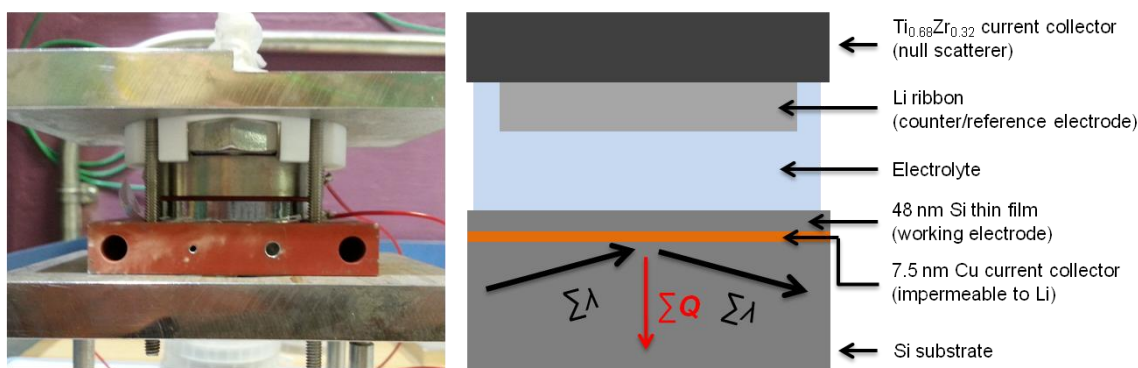


Figure 1.11. Image and diagram of an *in situ* electrochemical cell used on Beam Line 4B (Liquids Reflectometer) at the Spallation Neutron Source at Oak Ridge National Laboratory. O-ring seal/spacer and electrolyte filling ports not shown in diagram.

The use of deuterated carbonate electrolytes to enable *in situ* electrochemistry in neutron reflectometry cells revealed an additional issue. Commercial (protiated) electrolytes are available in a wide variety of formulations and are exceedingly pure to prevent undesirable electrochemical reactions which inhibit extended cycling. Deuterated electrolytes have to be prepared in the lab from their individual components. The deuterated components (organic carbonates) are $\geq 99.5\%$ pure, but ^1H NMR shows that the deuterated carbonates have a number of small impurities, while the protiated electrolyte has no detectable impurities (Figure 1.12). Due to the large electrolyte volume in the *in situ* cell, the electrochemically active impurities represent a significant proportion of the capacity of the Si electrode.⁷⁹ These components must be electrochemically consumed before SEI formation and electrode lithiation can occur. It is unclear whether or not these impurities affect the SEI. The use of protiated electrolytes results in "clean" electrochemistry, but significantly decreases the quality of reflectivity data, due to both a decrease in contrast and increase in background signal. With standard carbonate-based electrolytes, one must choose between high quality reflectivity data or high quality electrochemical data.

Like *in situ* neutron diffraction, *in situ* neutron reflectometry for Li-ion battery materials is a developing technique. Ongoing advancements in materials and methodology will enable the collection of higher quality reflectivity data without sacrificing clean electrochemistry.

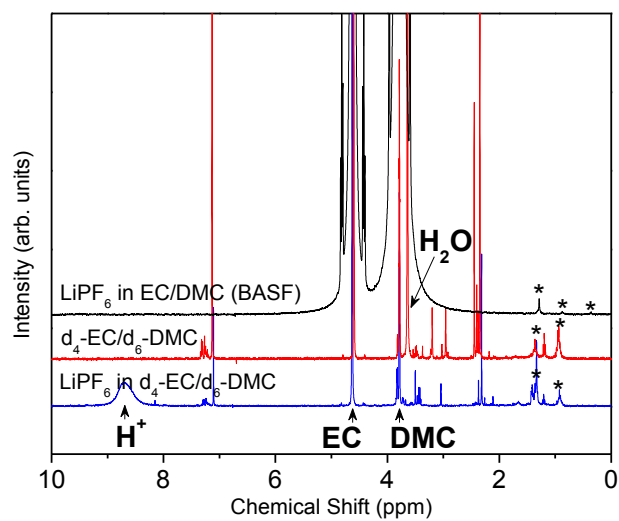


Figure 1.12. ^1H NMR of deuterated and protiated ethylene carbonate-dimethylcarbonate (EC-DMC) electrolytes used for *in situ* neutron reflectometry. Impurity peaks caused by epoxy sealant outgassing are marked (*). Reproduced from literature.⁷⁹

BIBLIOGRAPHY

1. Nag, J.; Haglund, R. F. J., Synthesis of vanadium dioxide thin films and nanoparticles. *Journal of Physics: Condensed Matter* **2008**, *20* (26), 264016.
2. Lysenko, S.; Rua, A. J.; Vikhnin, V.; Jimenez, J.; Fernandez, F.; Liu, H., Light-induced ultrafast phase transitions in VO₂ thin film. *Applied Surface Science* **2006**, *252* (15), 5512-5515.
3. Guzman, G.; Morineau, R.; Livage, J., Synthesis of vanadium dioxide thin films from vanadium alkoxides. *Materials Research Bulletin* **1994**, *29* (5), 509-515.
4. Livage, J.; Guzman, G.; Beteille, F.; Davidson, P., Optical properties of sol-gel derived vanadium oxide films. *Journal of Sol-Gel Science and Technology* **1997**, *8* (1-3), 857-865.
5. Manning, T. D.; Parkin, I. P.; Clark, R. J. H.; Sheel, D.; Pemble, M. E.; Vernadou, D., Intelligent window coatings: atmospheric pressure chemical vapour deposition of vanadium oxides. *Journal of Materials Chemistry* **2002**, *12* (10), 2936-2939; Piccirillo, C.; Binions, R.; Parkin, I. P., Synthesis and Functional Properties of Vanadium Oxides: V₂O₃, VO₂, and V₂O₅ Deposited on Glass by Aerosol-Assisted CVD. *Chemical Vapor Deposition* **2007**, *13* (4), 145-151; Field, M. N.; Parkin, I. P., Atmospheric pressure chemical vapour deposition of vanadium(V) oxide films on glass substrates from reactions of VOCl₃ and VCl₄ with water. *Journal of Materials Chemistry* **2000**, *10* (8), 1863-1866.
6. Pan, M.; Zhong, H.; Wang, S.; Liu, J.; Li, Z.; Chen, X.; Lu, W., Properties of VO₂ thin film prepared with precursor VO(acac)₂. *Journal of Crystal Growth* **2004**, *265* (1-2), 121-126.
7. Binions, R.; Hyett, G.; Piccirillo, C.; Parkin, I. P., Doped and un-doped vanadium dioxide thin films prepared by atmospheric pressure chemical vapour deposition from vanadyl acetylacetonate and tungsten hexachloride: the effects of thickness and crystallographic orientation on thermochromic properties. *Journal of Materials Chemistry* **2007**, *17* (44), 4652-4660; Saeli, M.; Piccirillo, C.; Parkin, I. P.; Ridley, I.; Binions, R., Nano-composite thermochromic thin films and their application in energy-efficient glazing. *Solar Energy Materials and Solar Cells* **2010**, *94* (2), 141-151.
8. Bai, H.; Cortie, M. B.; Maarof, A. I.; Dowd, A.; Kealley, C.; Smith, G. B., The preparation of a plasmonically resonant VO₂ thermochromic pigment. *Nanotechnology* **2009**, *20* (8), 085607.

9. Wu, J.; Huang, W.; Shi, Q.; Cai, J.; Zhao, D.; Zhang, Y.; Yan, J., Effect of annealing temperature on thermochromic properties of vanadium dioxide thin films deposited by organic sol–gel method. *Applied Surface Science* **2013**, *268* (0), 556-560; Zhang, Z.; Gao, Y.; Chen, Z.; Du, J.; Cao, C.; Kang, L.; Luo, H., Thermochromic VO₂ Thin Films: Solution-Based Processing, Improved Optical Properties, and Lowered Phase Transformation Temperature. *Langmuir* **2010**, *26* (13), 10738-10744.
10. Gao, Y.; Luo, H.; Zhang, Z.; Kang, L.; Chen, Z.; Du, J.; Kanehira, M.; Cao, C., Nanoceramic VO₂ thermochromic smart glass: A review on progress in solution processing. *Nano Energy* **2012**, *1* (2), 221-246.
11. Kamalisarvestani, M.; Saidur, R.; Mekhilef, S.; Javadi, F. S., Performance, materials and coating technologies of thermochromic thin films on smart windows. *Renewable and Sustainable Energy Reviews* **2013**, *26* (0), 353-364.
12. Chaput, F.; Dunn, B.; Fuqua, P.; Salloux, K., Synthesis and characterization of vanadium oxide aerogels. *Journal of Non-Crystalline Solids* **1995**, *188* (1–2), 11-18.
13. Morin, F. J., Oxides Which Show a Metal-to-Insulator Transition at the Neel Temperature. *Physical Review Letters* **1959**, *3* (1), 34-36.
14. Mott, N. F., Metal-Insulator Transition. *Reviews of Modern Physics* **1968**, *40* (4), 677-683; Corr, S. A.; Grossman, M.; Furman, J. D.; Melot, B. C.; Cheetham, A. K.; Heier, K. R.; Seshadri, R., Controlled Reduction of Vanadium Oxide Nanoscrolls: Crystal Structure, Morphology, and Electrical Properties. *Chemistry of Materials* **2008**, *20* (20), 6396-6404.
15. Golan, G.; Axelevitch, A.; Sigalov, B.; Gorenstein, B., Metal–insulator phase transition in vanadium oxides films. *Microelectronics Journal* **2003**, *34* (4), 255-258.
16. Hormoz, S.; Ramanathan, S., Limits on vanadium oxide Mott metal–insulator transition field-effect transistors. *Solid-State Electronics* **2010**, *54* (6), 654-659.
17. Whittaker, L.; Patridge, C. J.; Banerjee, S., Microscopic and Nanoscale Perspective of the Metal–Insulator Phase Transitions of VO₂: Some New Twists to an Old Tale. *The Journal of Physical Chemistry Letters* **2011**, *2* (7), 745-758.
18. Pergament, A.; Stefanovich, G.; Berezina, O.; Kirienko, D., Electrical conductivity of tungsten doped vanadium dioxide obtained by the sol–gel technique. *Thin Solid Films* **2013**, *531* (0), 572-576.
19. Koza, J. A.; He, Z.; Miller, A. S.; Switzer, J. A., Resistance Switching in Electrodeposited VO₂ Thin Films. *Chemistry of Materials* **2011**, *23* (18), 4105-4108.

20. Wu, Y. F.; Fan, L. L.; Chen, S. M.; Chen, S.; Zou, C. W.; Wu, Z. Y., Spectroscopic analysis of phase constitution of high quality VO₂ thin film prepared by facile sol-gel method. *AIP Advances* **2013**, 3 (4), -.
21. Pergament, A. L.; Stefanovich, G. B.; Kuldin, N. A.; Velichko, A. A., On the Problem of Metal-Insulator Transitions in Vanadium Oxides. *ISRN Condensed Matter Physics* **2013**, 2013, 6.
22. Lampe-Önnerud, C.; Nordblad, P.; Thomas, J. O., Chemical intercalation of lithium into a V₆O₁₃ host. *Solid State Ionics* **1995**, 81 (3–4), 189-199.
23. Lee, S. H.; Qiu, Y.; Broholm, C.; Ueda, Y.; Rush, J. J., Spin Fluctuations in a Magnetically Frustrated Metal LiV₂O₄. *Physical Review Letters* **2001**, 86 (24), 5554-5557.
24. Albaric, L.; Hovnanian, N.; Julbe, A.; Volle, G., Oxovanadium(V)-1-methoxy-2-propanoxide: synthesis and spectroscopic studies — a molecular precursor for a vanadium–magnesium oxide catalyst. *Polyhedron* **2001**, 20 (18), 2261-2268.
25. Graham, J. L.; Almquist, C. B.; Kumar, S.; Sidhu, S., An investigation of nanostructured vanadia/titania catalysts for the oxidation of monochlorobenzene. *Catalysis Today* **2003**, 88 (1–2), 73-82.
26. Van Overmeere, Q.; Kerman, K.; Ramanathan, S., Energy Storage in Ultrathin Solid Oxide Fuel Cells. *Nano Letters* **2012**, 12 (7), 3756-3760.
27. Brazdil, J. F.; Toft, M. A.; Bartek, J. P.; Teller, R. G.; Cyngier, R. M., Sol–Gel Method for Preparing Vanadium–Antimony Oxide Catalysts. *Chemistry of Materials* **1998**, 10 (12), 4100-4103.
28. Pistola, G.; Pasquali, M.; Tocci, M.; Manev, V.; Moshtev, R. V., Lithium/lithium vanadium oxide secondary batteries: IV. Evaluation of factors affecting the performance of test cells. *Journal of Power Sources* **1985**, 15 (1), 13-25.
29. Navone, C.; Pereira-Ramos, J. P.; Baddour-Hadjean, R.; Salot, R., Electrochemical and structural properties of V₂O₅ thin films prepared by DC sputtering. *Journal of Power Sources* **2005**, 146 (1–2), 327-330.
30. Wang, Y.; Takahashi, K.; Lee, K. H.; Cao, G. Z., Nanostructured Vanadium Oxide Electrodes for Enhanced Lithium-Ion Intercalation. *Advanced Functional Materials* **2006**, 16 (9), 1133-1144.
31. Augustyn, V.; Dunn, B., Vanadium oxide aerogels: Nanostructured materials for enhanced energy storage. *Comptes Rendus Chimie* **2010**, 13 (1–2), 130-141.

32. Lee, C.-Y.; Marschilok, A. C.; Subramanian, A.; Takeuchi, K. J.; Takeuchi, E. S., Synthesis and characterization of sodium vanadium oxide gels: the effects of water (n) and sodium (x) content on the electrochemistry of $\text{Na}_x\text{V}_2\text{O}_5 \cdot n\text{H}_2\text{O}$. *Physical Chemistry Chemical Physics* **2011**, *13* (40), 18047-18054.
33. Li, H.; He, P.; Wang, Y.; Hosono, E.; Zhou, H., High-surface vanadium oxides with large capacities for lithium-ion batteries: from hydrated aerogel to nanocrystalline $\text{VO}_2(\text{B})$, V_6O_{13} and V_2O_5 . *Journal of Materials Chemistry* **2011**, *21* (29), 10999-11009.
34. Zhang, L.; Wu, G.; Gao, G.; Yang, H., Electrochemical Performance of V_2O_5 Nano-Porous Aerogel Film. *Key Engineering Materials*, 2013; Vol. 537, pp 165-168.
35. West, K.; Zachau-Christiansen, B.; Jacobsen, T.; Atlung, S., V_6O_{13} As cathode material for lithium cells. *Journal of Power Sources* **1985**, *14* (1-3), 235-245.
36. Dubarry, M.; Gaubicher, J.; Guyomard, D.; Durupthy, O.; Steunou, N.; Livage, J.; Dupré, N.; Grey, C. P., Sol Gel Synthesis of $\text{Li}_{1+a}\text{V}_3\text{O}_8$. 1. From Precursors to Xerogel. *Chemistry of Materials* **2005**, *17* (9), 2276-2283; Arico, A. S.; Bruce, P.; Scrosati, B.; Tarascon, J.-M.; van Schalkwijk, W., Nanostructured materials for advanced energy conversion and storage devices. *Nat Mater* **2005**, *4* (5), 366-377.
37. Pan, A.; Zhang, J.-G.; Cao, G.; Liang, S.; Wang, C.; Nie, Z.; Arey, B. W.; Xu, W.; Liu, D.; Xiao, J.; Li, G.; Liu, J., Nanosheet-structured LiV_3O_8 with high capacity and excellent stability for high energy lithium batteries. *Journal of Materials Chemistry* **2011**, *21* (27), 10077-10084.
38. Lee, S.-H.; Cheong, H. M.; Seong, M. J.; Liu, P.; Tracy, C. E.; Mascarenhas, A.; Pitts, J. R.; Deb, S. K., Raman spectroscopic studies of amorphous vanadium oxide thin films. *Solid State Ionics* **2003**, *165* (1-4), 111-116.
39. Livage, J., Sol-gel chemistry and electrochemical properties of vanadium oxide gels. *Solid State Ionics* **1996**, *86-88*, Part 2 (0), 935-942.
40. Clavero, C.; Slack, J. L.; Anders, A., Size and composition-controlled fabrication of thermochromic metal oxide nanocrystals. *Journal of Physics D: Applied Physics* **2013**, *46* (36), 362001.
41. Leventis, N.; Vassilaras, P.; Fabrizio, E. F.; Dass, A., Polymer nanoencapsulated rare earth aerogels: chemically complex but stoichiometrically similar core-shell superstructures with skeletal properties of pure compounds. *Journal of Materials Chemistry* **2007**, *17* (15), 1502-1508.
42. Livage, J., Vanadium pentoxide gels. *Chemistry of Materials* **1991**, *3* (4), 578-593.

43. Luca, V.; Hook, J. M., Study of the Structure and Mechanism of Formation through Self-Assembly of Mesoporous Vanadium Oxide. *Chemistry of Materials* **1997**, *9* (12), 2731-2744; Rouhani, R.; Aghabozorg, H. R.; Asadi Asadabad, M.; Aghabozorg, H., Synthesis of Mo, W, and Mo- and W-Doped Multiwall VONTs via Sol-Gel and Hydrothermal Methods. *Journal of Chemistry* **2013**, *2013*, 5.
44. Mege, S.; Verelst, M.; Lecante, P.; Perez, E.; Ansart, F.; Savariault, J. M., Surfactant effects in vanadium alkoxide derived gels. *Journal of Non-Crystalline Solids* **1998**, *238* (1-2), 37-44.
45. Alonso, B.; Livage, J., Synthesis of Vanadium Oxide Gels from Peroxovanadic Acid Solutions: A ^{51}V NMR Study. *Journal of Solid State Chemistry* **1999**, *148* (1), 16-19.
46. Fontenot, C. J.; Wiench, J. W.; Pruski, M.; Schrader, G. L., Vanadia Gel Synthesis via Peroxovanadate Precursors. 1. In Situ Laser Raman and ^{51}V NMR Characterization of the Gelation Process. *The Journal of Physical Chemistry B* **2000**, *104* (49), 11622-11631.
47. Livage, J.; Pelletier, O.; Davidson, P., Vanadium Pentoxide Sol and Gel Mesophases. *Journal of Sol-Gel Science and Technology* **2000**, *19* (1-3), 275-278.
48. Pelletier, O.; Davidson, P.; Bourgaux, C.; Coulon, C.; Regnault, S.; Livage, J., A Detailed Study of the Synthesis of Aqueous Vanadium Pentoxide Nematic Gels. *Langmuir* **2000**, *16* (12), 5295-5303.
49. Fontenot, C. J.; Wiench, J. W.; Pruski, M.; Schrader, G. L., Vanadia Gel Synthesis via Peroxovanadate Precursors. 2. Characterization of the Gels. *The Journal of Physical Chemistry B* **2001**, *105* (43), 10496-10504.
50. Carn, F.; Steunou, N.; Livage, J.; Colin, A.; Backov, R., Tailor-Made Macroporous Vanadium Oxide Foams. *Chemistry of Materials* **2005**, *17* (3), 644-649.
51. Leventis, N.; Sotiriou-Leventis, C.; Mulik, S.; Dass, A.; Schnobrich, J.; Hobbs, A.; Fabrizio, E. F.; Luo, H.; Churu, G.; Zhang, Y.; Lu, H., Polymer nanoencapsulated mesoporous vanadia with unusual ductility at cryogenic temperatures. *Journal of Materials Chemistry* **2008**, *18* (21), 2475-2482.
52. Luo, H.; Churu, G.; Fabrizio, E. F.; Schnobrich, J.; Hobbs, A.; Dass, A.; Mulik, S.; Zhang, Y.; Grady, B. P.; Capececiatro, A.; Sotiriou-Leventis, C.; Lu, H.; Leventis, N., Synthesis and characterization of the physical, chemical and mechanical properties of isocyanate-crosslinked vanadia aerogels. *Journal of Sol-Gel Science and Technology* **2008**, *48* (1-2), 113-134.
53. Hench, L. L.; West, J. K., The sol-gel process. *Chemical Reviews* **1990**, *90* (1), 33-72.

54. Gash, A. E.; Tillotson, T. M.; Satcher, J. H.; Poco, J. F.; Hrubesh, L. W.; Simpson, R. L., Use of Epoxides in the Sol–Gel Synthesis of Porous Iron(III) Oxide Monoliths from Fe(III) Salts. *Chemistry of Materials* **2001**, *13* (3), 999-1007; Gash, A. E.; Tillotson, T. M.; Satcher Jr, J. H.; Hrubesh, L. W.; Simpson, R. L., New sol–gel synthetic route to transition and main-group metal oxide aerogels using inorganic salt precursors. *Journal of Non-Crystalline Solids* **2001**, *285* (1–3), 22-28.
55. Aerogel.org. Metal Oxide Aerogels. <http://www.aerogel.org/?p=44> (accessed July 9, 2015).
56. Lapina, O. B.; Khabibulin, D. F.; Shubin, A. A.; Terskikh, V. V., Practical aspects of ^{51}V and ^{93}Nb solid-state NMR spectroscopy and applications to oxide materials. *Progress in Nuclear Magnetic Resonance Spectroscopy* **2008**, *53* (3), 128-191.
57. Pistoia, G.; Panero, S.; Tocci, M.; Moshtev, R. V.; Manev, V., Solid solutions $\text{Li}_{1+x}\text{V}_3\text{O}_8$ as cathodes for high rate secondary Li batteries. *Solid State Ionics* **1984**, *13* (4), 311-318; Pistoia, G.; Pasquali, M.; Wang, G.; Li, L., Li/ $\text{Li}_{1+x}\text{V}_3\text{O}_8$ Secondary Batteries. *Journal of the Electrochemical Society* **1990**, *137* (8), 2365-2370; Koval'chuk, E. P.; Reshetnyak, O. V.; Kovalyshyn, Y. S.; Blażejowski, J., Structure and properties of lithium trivanadate—a potential electroactive material for a positive electrode of secondary storage. *Journal of Power Sources* **2002**, *107* (1), 61-66.
58. Chen, Z.; Lee, D.-J.; Sun, Y.-K.; Amine, K., Advanced cathode materials for lithium-ion batteries. *MRS Bulletin* **2011**, *36* (07), 498-505.
59. Song, H.-K.; Lee, K. T.; Kim, M. G.; Nazar, L. F.; Cho, J., Recent Progress in Nanostructured Cathode Materials for Lithium Secondary Batteries. *Advanced Functional Materials* **2010**, *20* (22), 3818-3834.
60. Scrosati, B.; Garche, J., Lithium batteries: Status, prospects and future. *Journal of Power Sources* **2010**, *195* (9), 2419-2430.
61. Chernova, N. A.; Roppolo, M.; Dillon, A. C.; Whittingham, M. S., Layered vanadium and molybdenum oxides: batteries and electrochromics. *Journal of Materials Chemistry* **2009**, *19* (17), 2526-2552.
62. Russell, T. P., X-ray and neutron reflectivity for the investigation of polymers. *Materials Science Reports* **1990**, *5* (4), 171-271.
63. Hirayama, M.; Sonoyama, N.; Abe, T.; Minoura, M.; Ito, M.; Mori, D.; Yamada, A.; Kanno, R.; Terashima, T.; Takano, M.; Tamura, K.; Mizuki, J. i., Characterization of electrode/electrolyte interface for lithium batteries using in situ synchrotron X-ray reflectometry—A new experimental technique for LiCoO_2 model electrode. *Journal of Power Sources* **2007**, *168* (2), 493-500.

64. Bianchini, M.; Suard, E.; Croguennec, L.; Masquelier, C., Li-Rich $\text{Li}_{1+x}\text{Mn}_{2-x}\text{O}_4$ Spinel Electrode Materials: An Operando Neutron Diffraction Study during Li+Extraction/Insertion. *The Journal of Physical Chemistry C* **2014**, *118* (45), 25947-25955.
65. Heitmann, T.; Montfrooij, W., *Practical Neutron Scattering at a Steady State Source*. Mizzou Media - University BookStores: 2012.
66. Owejan, J. E.; Owejan, J. P.; DeCaluwe, S. C.; Dura, J. A., Solid Electrolyte Interphase in Li-Ion Batteries: Evolving Structures Measured In situ by Neutron Reflectometry. *Chemistry of Materials* **2012**, *24* (11), 2133-2140.
67. Jerliu, B.; Dorrer, L.; Huger, E.; Borchardt, G.; Steitz, R.; Geckle, U.; Oberst, V.; Bruns, M.; Schneider, O.; Schmidt, H., Neutron reflectometry studies on the lithiation of amorphous silicon electrodes in lithium-ion batteries. *Physical Chemistry Chemical Physics* **2013**, *15* (20), 7777-7784.
68. Browning, J. F.; Baggetto, L.; Jungjohann, K. L.; Wang, Y.; Tenhaeff, W. E.; Keum, J. K.; Wood, D. L.; Veith, G. M., In Situ Determination of the Liquid/Solid Interface Thickness and Composition for the Li Ion Cathode $\text{LiMn}_{1.5}\text{Ni}_{0.5}\text{O}_4$. *ACS Applied Materials & Interfaces* **2014**, *6* (21), 18569-18576.
69. Sears, V. F., Neutron scattering lengths and cross sections. *Neutron News* **1992**, *3* (3), 26-37.
70. Bobrikov, I. A.; Balagurov, A. M.; Hu, C.-W.; Lee, C.-H.; Chen, T.-Y.; Deleg, S.; Balagurov, D. A., Structural evolution in LiFePO_4 -based battery materials: In-situ and ex-situ time-of-flight neutron diffraction study. *Journal of Power Sources* **2014**, *258*, 356-364.
71. Dolotko, O.; Senyshyn, A.; Mühlbauer, M. J.; Nikolowski, K.; Ehrenberg, H., Understanding structural changes in NMC Li-ion cells by in situ neutron diffraction. *Journal of Power Sources* **2014**, *255*, 197-203.
72. Hansen, T. C.; Kohlmann, H., Chemical Reactions followed by in situ Neutron Powder Diffraction. *Zeitschrift für anorganische und allgemeine Chemie* **2014**, *640* (15), 3044-3063.
73. Roberts, M.; Biendicho, J. J.; Hull, S.; Beran, P.; Gustafsson, T.; Svensson, G.; Edström, K., Design of a new lithium ion battery test cell for in-situ neutron diffraction measurements. *Journal of Power Sources* **2013**, *226*, 249-255.
74. Liu, H.; Fell, C. R.; An, K.; Cai, L.; Meng, Y. S., In-situ neutron diffraction study of the $x\text{Li}_2\text{MnO}_3 \cdot (1-x)\text{LiMO}_2$ ($x = 0, 0.5$; $M = \text{Ni}, \text{Mn}, \text{Co}$) layered oxide compounds during electrochemical cycling. *Journal of Power Sources* **2013**, *240*, 772-778.

75. Nishimura, S.-i.; Kobayashi, G.; Ohoyama, K.; Kanno, R.; Yashima, M.; Yamada, A., Experimental visualization of lithium diffusion in Li_xFePO_4 . *Nat Mater* **2008**, 7 (9), 707-711.
76. Kim, J.-H.; Huq, A.; Chi, M.; Pieczonka, N. P. W.; Lee, E.; Bridges, C. A.; Tessema, M. M.; Manthiram, A.; Persson, K. A.; Powell, B. R., Integrated Nano-Domains of Disordered and Ordered Spinel Phases in $\text{LiNi}_{0.5}\text{Mn}_{1.5}\text{O}_4$ for Li-Ion Batteries. *Chemistry of Materials* **2014**, 26 (15), 4377-4386.
77. Mohanty, D.; Huq, A.; Payzant, E. A.; Sefat, A. S.; Li, J.; Abraham, D. P.; Wood, D. L.; Daniel, C., Neutron Diffraction and Magnetic Susceptibility Studies on a High-Voltage $\text{Li}_{1.2}\text{Mn}_{0.55}\text{Ni}_{0.15}\text{Co}_{0.10}\text{O}_2$ Lithium Ion Battery Cathode: Insight into the Crystal Structure. *Chemistry of Materials* **2013**, 25 (20), 4064-4070; Shin, D. W.; Bridges, C. A.; Huq, A.; Paranthaman, M. P.; Manthiram, A., Role of Cation Ordering and Surface Segregation in High-Voltage Spinel $\text{LiMn}_{1.5}\text{Ni}_{0.5-x}\text{M}_x\text{O}_4$ (M = Cr, Fe, and Ga) Cathodes for Lithium-Ion Batteries. *Chemistry of Materials* **2012**, 24 (19), 3720-3731.
78. Wang, X.-L.; An, K.; Cai, L.; Feng, Z.; Nagler, S. E.; Daniel, C.; Rhodes, K. J.; Stoica, A. D.; Skorpenske, H. D.; Liang, C.; Zhang, W.; Kim, J.; Qi, Y.; Harris, S. J., Visualizing the chemistry and structure dynamics in lithium-ion batteries by in-situ neutron diffraction. *Sci. Rep.* **2012**, 2.
79. Veith, G. M.; Doucet, M.; Baldwin, J. K.; Sacci, R. L.; Fears, T. M.; Wang, Y.; Browning, J. F., Direct determination of solid-electrolyte interphase thickness and composition as a function of state of charge on a silicon anode. *Journal of Physical Chemistry C* **2015**, 119, 20339-20349.
80. Veith, G. M.; Baggetto, L.; Sacci, R. L.; Unocic, R. R.; Tenhaeff, W. E.; Browning, J. F., Direct measurement of the chemical reactivity of silicon electrodes with LiPF_6 -based battery electrolytes. *Chemical Communications* **2014**, 50 (23), 3081-3084.
81. Kharlampieva, E.; Kozlovskaya, V.; Chan, J.; Ankner, J. F.; Tsukruk, V. V., Spin-Assisted Layer-by-Layer Assembly: Variation of Stratification as Studied with Neutron Reflectivity. *Langmuir* **2009**, 25 (24), 14017-14024.

PAPER**I. Economical synthesis of vanadia aerogels via epoxide-assisted gelation of VOCl_3**

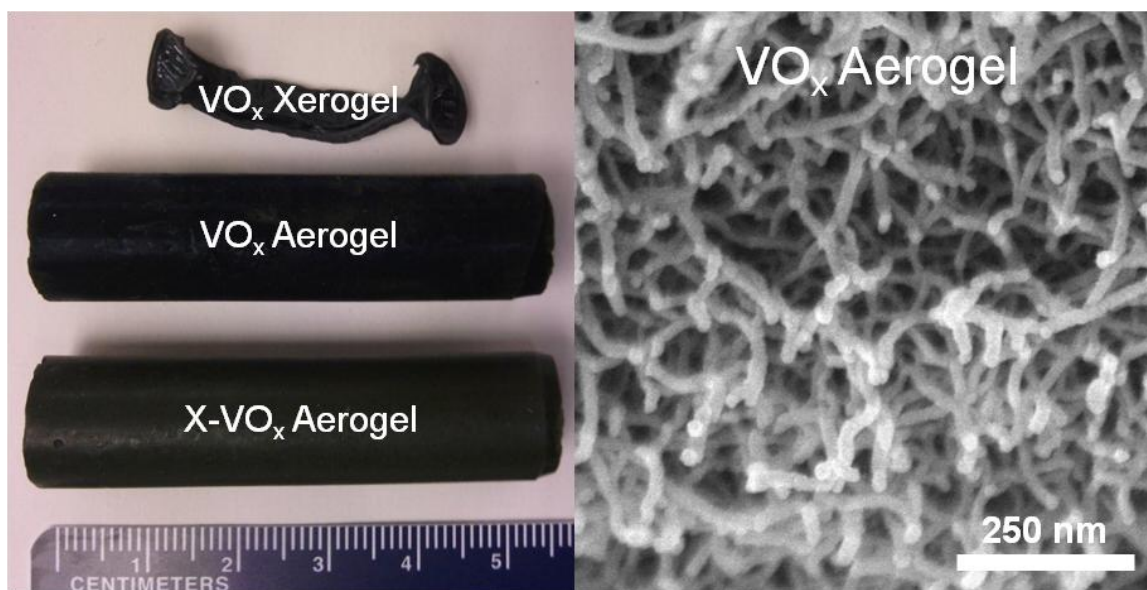
Tyler M. Fears*, Chariklia Sotiriou-Leventis, Jeffrey G. Winiarz, Nicholas Leventis

Department of Chemistry, Missouri University of Science and Technology, 400 W. 11th

St., Rolla, MO 65409, USA

*Email address: tmf9rc@mst.edu

Abstract: Herein is reported the first synthesis of vanadium oxide (vanadia) aerogels via epoxide-assisted gelation. Vanadia aerogels fabricated via epoxide-assisted gelation using VOCl_3 and epichlorohydrin mimic those fabricated via the hydrolysis of vanadium oxytriisopropoxide while reducing cost per mole by a factor of 10, on par with silica gels synthesized from alkyl orthosilicates. Typical vanadia aerogels possess a macroporous nanoworm morphology, a density of 0.103 g/cm^3 , 96.9 % porosity, a specific surface area of $102 \text{ m}^2/\text{g}$, and ~18 % reversible hydration capacity by mass. ^1H and ^{13}C NMR reveal that epoxide ring-opening does not proceed through epoxide protonation, as is the typical case with other transition metal oxide gels, but rather through Lewis-acid-catalyzed ring-opening. A multi-step gelation mechanism is proposed involving a fast initial V^{V} oxide gelation, driven by H^+ and Cl^- consumption during epoxide ring-opening, followed by partial vanadia dissolution, $\text{V}^{\text{V}} \rightarrow \text{V}^{\text{IV}}$ reduction, and secondary gelation of low-valent $\text{V}^{\text{IV/V}}$ oxide.

Graphical Abstract

Keywords: vanadia, vanadium oxide, aerogel, vanadium oxytrichloride, epichlorohydrin, epoxide-assisted gelation

Highlights:

- Developed first epoxide-assisted gelation method for vanadium oxide, using epichlorohydrin and VOCl_3 .
- Gels synthesized via epoxide-assisted gelation are comparable to those fabricated via the hydrolysis of vanadium(V) alkoxides.
- Observed Lewis-acid-catalyzed epoxide ring-opening under both protic and aprotic conditions.
- Observed secondary gelation step after partial dissolution of V^{V} oxide matrix and $\text{V}^{\text{V}} \rightarrow \text{V}^{\text{IV}}$ reduction.

1 Introduction

Aqueous vanadium oxide (vanadia) sol–gel chemistry is well studied and serves as the basis on which all vanadia sol–gel chemistry is modeled. The first step in the synthesis of aqueous vanadium oxide gels is the formation of a supersaturated solution of vanadium oxy-hydrates [1]. This step can be accomplished using a variety of methods, e.g., quenching molten V_2O_5 in H_2O (oxide hydrolysis) [2]; decomposition of soluble vanadium oxy-peroxide hydrates, e.g., $VO(O_2)(H_2O)_3^+$, $VO(O_2)_2(H_2O)^{2-}$ (peroxide-assisted hydrolysis) [3, 4]; or passing a water-soluble vanadate salt such as $NaVO_3$ through a proton-exchange column (cation-exchange) [5–7]. These hydrates evolve into acidic vanadates with varying degrees of hydration (e.g., $VO(OH)_3(H_2O)_2$, $V_{10}O_{28}^{6-}$, $V_6O_{16}^{2-}$), dependent upon pH, temperature, and V^V concentration [1, 8, 9]. The strong anisotropy of the polymerizable, neutral, monomeric $VO(OH)_3(H_2O)_2$ leads to the formation of vanadyl oxo-polymer chains, which then aggregate, leading to fibrous gels [1]. This morphology is markedly dissimilar from common inorganic gels, which are typified by random aggregates of spherical particles [10–12]. Variations on these techniques also exist which utilize templating agents to modify gel morphology [7].

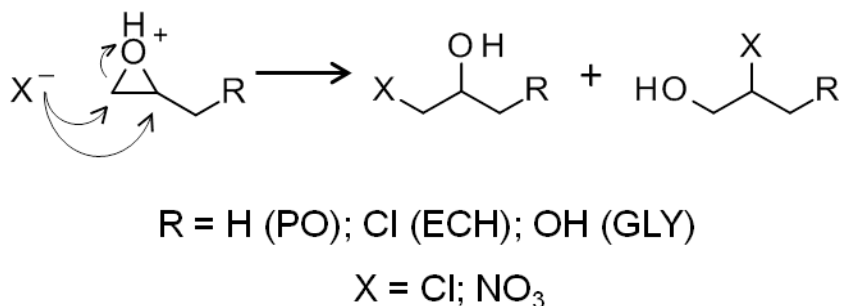
To date, aqueous syntheses have only been shown capable of producing V_2O_5 gels (and related V^V gels such as $Na_{2x}V_2O_{5-x}$). Lower oxidation states are accessible via non-aqueous gelation methods. Thus, hydrolysis of organic V^{IV} and V^V species in non-aqueous solvents is known to produce high-quality vanadia powders, films, and monoliths, e.g., VO_2 films can be made from hydrolysis of vanadyl(IV) acetylacetonate in methanol [13]. Furthermore, while organic V^V species do undergo hydrolysis to form vanadium(V) oxide gels, partial V^V (yellow/ red) \rightarrow V^{IV} (blue/brown) reduction is nearly

universal in organic solvents, resulting in gels with varying degrees of V^{IV} content [1, 14].

The most common method for fabricating non-aqueous vanadia gels is the hydrolysis of vanadyl(V) alkoxides in a water-miscible solvent, e.g., vanadium oxytripropoxide in acetone [15–18]. Reaction proceeds extremely rapidly, is highly exothermic, and yields light green gels. Some alkoxide-derived gels also have a nanoworm morphology intermediate between the random spherical aggregates commonly seen in metal oxide gels and the monofilament fibers typical of aqueous vanadia gels [5, 13–15, 17–20]. Nevertheless, while the gelation mechanism is well studied for aqueous V_2O_5 and $V_2O_5 \cdot xH_2O$ gels, the oxo-polymer formation mechanisms in non-aqueous vanadia gels are less studied, due in part to the increased complexity of the system [1, 8, 9, 21].

Meanwhile, epoxide-assisted gelation has been shown effective for a wide range of metal oxides [10–12, 22]. In this method, an epoxide (typically propylene oxide: PO, epichlorohydrin: ECH, or glycidol: GLY) reacts with an acidic hydrated metal salt (typically a chloride or nitrate), undergoing H^+ -catalyzed irreversible ring-opening by the nucleophilic anions, forming the corresponding alcohol (Scheme 1). Epoxide ring-opening raises the pH of the solution uniformly by scavenging protons from the acidic metal hydrate. This gradual change favors controlled ololation (metal–hydroxy bridge formation) and oxolation (metal–oxide bridge formation) creating a percolating metal oxide network, leading to a gel instead of a precipitate [22]. Ex situ NMR measurements on iron(III) [11] and chrome(III) [12] oxide aerogels made from their chlorides and PO

indicate that S_N2 ring-opening by the nucleophilic anions occurs at both epoxide carbons, consistent with H^+ -catalyzed epoxide ring-opening [23, 24].



Scheme 1 Acid-scavenging mechanism for commonly used epoxides and nucleophilic metal salt anions

Aside from a few examples (Si, Ti, Al), transition metal alkoxides are either prohibitively expensive or commercially unavailable, whereas their chlorides and nitrates which can be used for epoxide-assisted gelation are widely available and comparatively inexpensive. PO and ECH are inexpensive epoxides which have sufficiently different reactivities so as to provide useful control over gelation rates. In addition, by replacing H_2O -sensitive metal alkoxides with air-stable metal salts, precursor sols can be more easily manipulated without degradation. Though this method has been successfully used to synthesize aerogels for a large number of metal oxide systems, epoxide-assisted gelation for vanadium oxides has remained elusive.

In this communication, the formation of vanadia aerogels via epoxide-assisted gelation is demonstrated using $VOCl_3$ and ECH, resulting in gels which replicate the physical properties of those fabricated via the hydrolysis of vanadium oxytriopoxide [17, 18], namely a high surface area, macroporosity (pore size >50 nm), a nanoworm

morphology, and the ability to form extremely strong composite aerogels via isocyanate crosslinking [17, 18]. Replacing vanadium oxytripropoxide with VOCl_3 and ECH for the synthesis of vanadia aerogels represents a >tenfold reduction in reagent cost per mole [25]. From a mechanistic point of view, we observe H^+ -free epoxide ring-opening and a discrete multi-step gelation, processes not previously reported in the literature for epoxide-assisted gelation.

2 Results

2.1 Gelation

Vanadia (VO_x) and isocyanate-crosslinked vanadia (X-VO_x) aerogels and xerogels were prepared as summarized in Scheme 2 and Table 1.

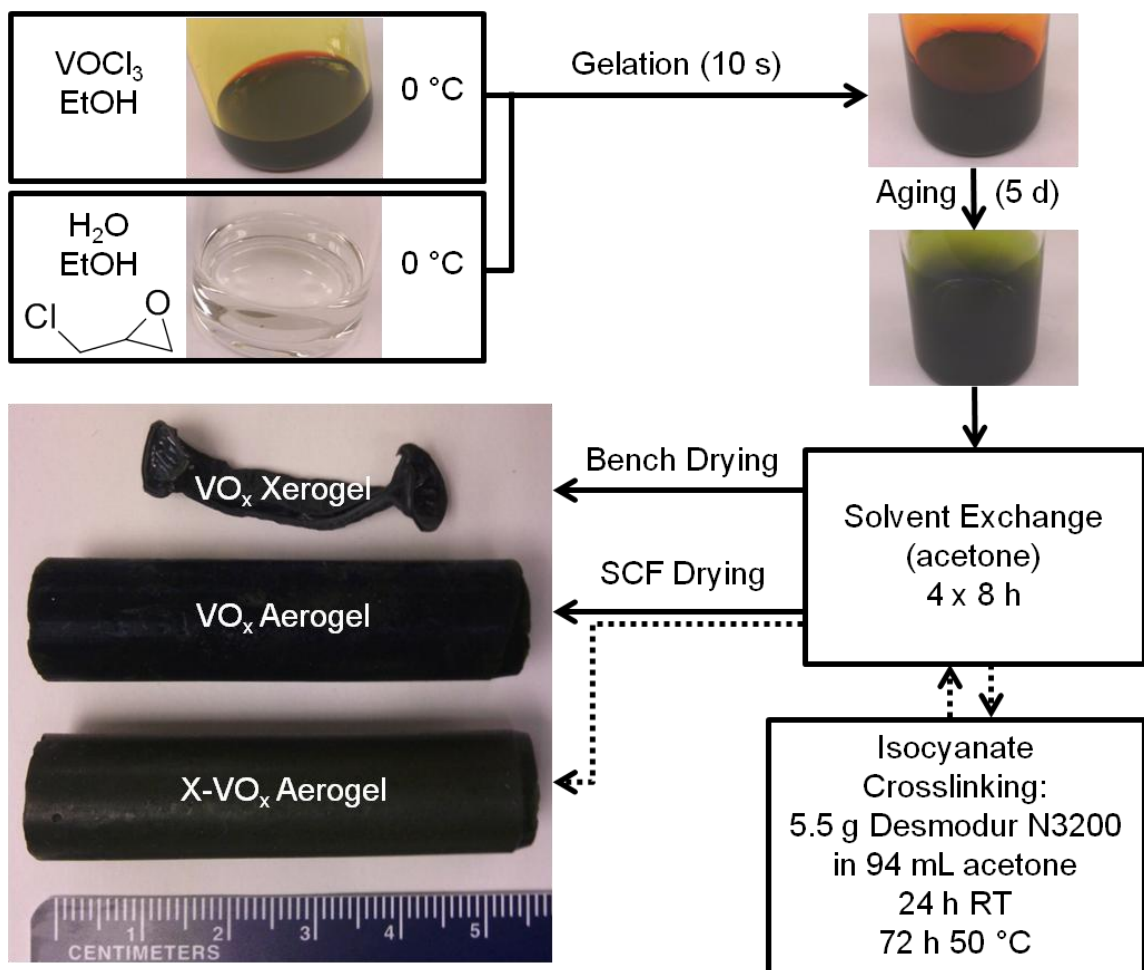
Gelation is highly exothermic and extremely rapid (<10 s), resulting in bright red, glassy monoliths. Cooling precursor sols to $-78\text{ }^\circ\text{C}$ in a dry ice-acetone bath prevented gelation, but upon removal from the cooling bath, i.e., to pour into molds, sols gelled in <1 min as they warmed up.

The precursor sol is red up through gelation; however, while investigating potential precursors formed during gelation, other solution colors were observed. VOCl_3 (orange) forms a red solution in EtOH, which becomes yellow upon the addition of ECH, indicating ECH ring-opening takes place in the absence of H_2O (discussed later in Sect. 2.1.3). Optical absorption by V^{V} species in the visible range is attributed to ligand-to-metal charge-transfer transitions [26–32], which cover from the UV to ~ 350 , ~ 450 , and ~ 500 nm for the yellow, orange, and red species observed here, respectively (Electronic Supplementary Material, Fig. S.1). The addition of 3 equivalents of H_2O (0.308 mL) to the VOCl_3 (0.540 mL)–EtOH (6.00 mL) solution does not effect solid formation and

results in only a slight change in the absorption spectrum, qualitatively attributed to the exchange of Cl^- , EtO^- , and EtOH ligands with HO^- and H_2O . The absorption spectrum of the $\text{VOCl}_3\text{-H}_2\text{O-EtOH}$ solution is indistinguishable from that of the gel immediately after gelation, suggesting that similar coordination spheres exist around V^{V} in both cases. The absorption leading to red V^{V} species is commonly—though neither universally nor exclusively—seen in 5- and 6-coordinate V^{V} chelates with halide, HO^- , and H_2O ligands; however, the shape of the visible absorption spectrum alone is not sufficient for unambiguous determination of ligand arrangement or coordination number [21, 30–33].

Table 1 Results of attempts to fabricate gels at different sol concentrations

Nominal Sol Concentration (target aerogel density)	EtOH [mL]	VOCl_3 [eq.]	ECH [eq.]	H_2O [eq.]	Result (after 5 days aging)
Standard (0.10 g/cm ³)	6.00	1.00 (0.540 mL)	5.00 (2.25 mL)	9.00 (0.925 mL)	translucent, dark green gel
1/2 (0.05 g/cm ³)	6.00	0.50	2.50	4.50	very turbid, green gel
	6.00	0.50	2.50	9.00	turbid, green gel
	6.00	0.50	5.00	4.50	translucent, green gel
	6.00	0.50	5.00	9.00	translucent, dark green gel
1/10 (0.01 g/cm ³)	6.00	0.10	0.50	0.90	red sol
	6.00	0.10	0.50	9.00	green flocc
	6.00	0.10	5.00	0.90	orange sol
	6.00	0.10	5.00	9.00	dark green sol (translucent gel in 7 days)



Scheme 2 Fabrication procedure for vanadia (VO_x) aerogels, polymer-crosslinked vanadia aerogels (X-VO_x), and vanadia xerogels. Wet-gels shown in scintillation vials demonstrate optical transparency

Gels became dark green after several hours of aging. While absorption at short wavelengths decreases, absorption increases across the entire visible spectrum, causing the gels to lose translucency (Fig. S.2). This color change is attributed to the partial reduction of red/yellow V^V to blue V^{IV}, common in non-aqueous vanadia gels. Acetaldehyde ($m/z = 44$), the primary oxidation product of EtOH [34], was identified by its distinctive scent (sour apples), readily apparent in wet-gels before solvent exchange,

but is not easily detected via tandem mass spectrometry methods, due to interference from CO₂ ($m/z = 44$), which is present in the atmosphere at levels 10,000 times the odor threshold of acetaldehyde [35]. Gels underwent minimal syneresis. All solvent-exchange baths were colorless, and no measureable shrinkage was observed during aging or supercritical drying.

Ultra-low-density gels (target densities: 0.05 and 0.01 g/ cm³) were fabricated by reducing the VOCl₃ concentration in the standard formulation (Table 1). Reducing the ECH and H₂O concentrations to maintain stoichiometric ratios reduced the optical quality (translucency) of gels and in some cases prevented gelation. Gels could only be made from sols with nominally constant concentrations of ECH and H₂O. Curiously, the lowest density gels passed through three distinct phases, forming a soft red gel initially (5 min), followed by a dissolution of the solid matrix and the formation of a deep green sol (~24 h), with the eventual formation of a stable deep green gel (7 days). Unfortunately, ultra-low-density aerogels could not be fabricated, as these wet-gels collapsed during supercritical CO₂ drying.

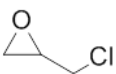

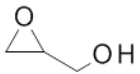

2.1.1 H₂O and Epoxide Optimization

Precursor sol compositions along with the corresponding gelation rates and gel quality are summarized in Table 2.

H₂O content in the standard gel formulation was optimized to lengthen gelation time while maintaining optical transparency. Since optical inhomogeneity, e.g., turbidity, is determined by regions of differing absorption or refractive index and generally visible to the naked eye only when such regions are on the 1m scale, the lack of visible scattering

is indicative of the absence of inhomogeneities above ~1 lm. Increasing the H₂O/VOCl₃ ratio in the precursor sol shortened the gelation time, at the extreme of which (20:1 by mole) gelation occurred faster than the mixing of the precursor solutions, resulting in visibly inhomogeneous gels (colored swirls). Lowering the ratio (6:1 by mole) produced homogeneously turbid gels, implying scattering from lm-scale inhomogeneities.

Table 2 Gel quality and gelation time as a function of H₂O content and epoxide functionality. Optimized gel formulation bolded.

	VOCl ₃ [eq.]	Epoxide [eq.]	H ₂ O [eq.]	Gelation Time	Optical Quality
ECH	1.00	5.00	6.00	10 s	Turbid
	1.00	5.00	9.00	< 10 s	Translucent
	1.00	5.00	12.0	< 10 s	Translucent
	1.00	5.00	20.0	< 3 s	Inhomogeneous
PO					
	1.00	5.00	9.00	<< 1 s	Inhomogeneous
GLY					
	1.00	5.00	15.0	15 min	Translucent (Fragile)
DMO					
	1.00	5.00	12.0	10 min	Very Turbid

The addition of 9 equivalents of H₂O (0.925 mL) to the VOCl₃ (0.180 mL)–EtOH (6.00 mL) solution without ECH formed an orange precipitate with a red supernatant in ~1 h, both of which became green within several hours. Adding ECH to this VOCl₃–H₂O–EtOH solution before precipitation resulted in an inhomogeneous gel in ~10 s. This result is attributed to the poor miscibility of H₂O and ECH, leading to gelation prior to the realization of a homogeneous sol. Adding ECH to VOCl₃ resulted in an indefinitely

stable yellow solution. The addition of H₂O to this solution resulted in the immediate formation of inhomogeneous “gunk.” High-quality gels are only realized upon the simultaneous addition of H₂O and ECH to the VOCl₃ solution.

It has been reported that modifying epoxide functionality at the α -carbon and utilizing less-strained oxetanes can alter gelation rates [22, 36]. Several commercially available alternatives were investigated, as a slower gelation rate would facilitate fabrication. Replacing ECH with PO significantly decreased the gelation time, leading to instantaneous gelation and the formation of inhomogeneous solids in the sol. GLY significantly slowed gelation (15 min), but the resulting gels were extremely fragile and crumbled even with careful handling during solvent exchange. Gels made using GLY also exhibited both a green liquid expelled during syneresis and a green supernatant during solvent exchange, attributed to improved vanadium oxide chelation in polyols formed from glycidol ring-opening [21]. Dimethyl oxetane (DMO) significantly slowed gelation and gels remained robust, though they were entirely opaque, indicating μ m-scale inhomogeneities.

2.1.2 Mesophase ¹³C and ¹H Nuclear Magnetic Resonance (NMR)

While gelation occurs too quickly to monitor spectroscopically, gel aging was successfully monitored via in situ mesophase NMR to identify organic reaction products and their formation rates. All major organic species in the gel effluent were identifiable, as shown in Fig. 1. No redox products were detected via ¹³C or ¹H NMR due to their low concentration and the unavoidably large peak width caused by susceptibility broadening [37]. The spectra confirm that Cl⁻ participated in nucleophilic attack *exclusively* on the

less-substituted carbon of the epoxide ring, unexpected in H^+ -catalyzed epoxide ring-opening [11, 12, 23, 24], forming 1,3-dichloro-2-propanol (DCPH). DCPH peak areas were constant throughout aging, indicating that Cl^- scavenging occurred before the first spectrum could be collected (5–15 min after gelation). Over the course of aging, excess ECH underwent nucleophilic attack by H_2O and $EtOH$, forming 1-chloro-2,3-propane diol (MCPDH₂) and 1-chloro-3(2)-ethoxy-2(3)-propanol (MCEPH), respectively. This experiment is unable to discern the ring-opening mechanism in these cases, as attack on either epoxy carbon by H_2O results in identical products, and the 2-ethoxy-3-ol and 3-ethoxy-2-ol have nearly identical ¹³C and ¹H chemical shifts. Time-dependent concentrations of ECH and its ring-opened products follow exponential behavior (Fig. S.3), indicating that ring-opening follows ECH-limited first-order reaction kinetics.

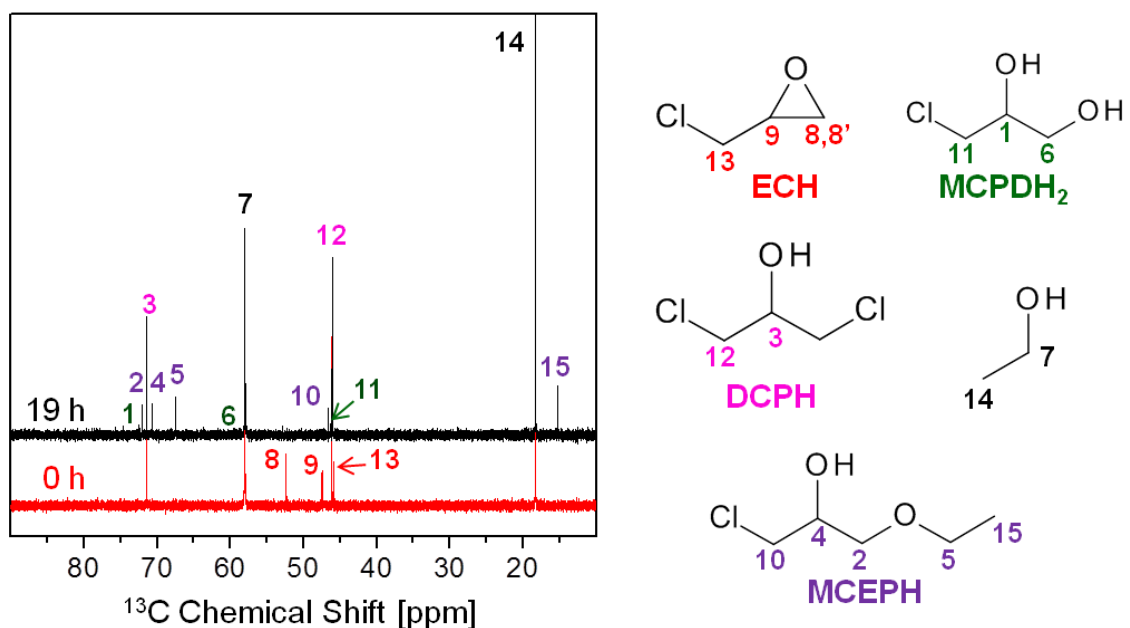


Fig. 1 Mesophase ¹³C NMR of a wet-gel before (0 h) and after (19 h) aging. All observed chemical shifts and peak integrals are consistent with EtOH, ECH, and species produced from ECH ring-opening

$V^V \rightarrow V^{IV}$ reduction was observed by monitoring the reference peak (EtOH: 18.3 ppm in ^{13}C) drift as a function of time (Fig. 2), analogous to the Evans method for measuring solute paramagnetic moments [38]. The large, positive, time-dependent peak drift is consistent with the reduction of diamagnetic V^V to paramagnetic V^{IV} and the observed color change (red to green) during gel aging.

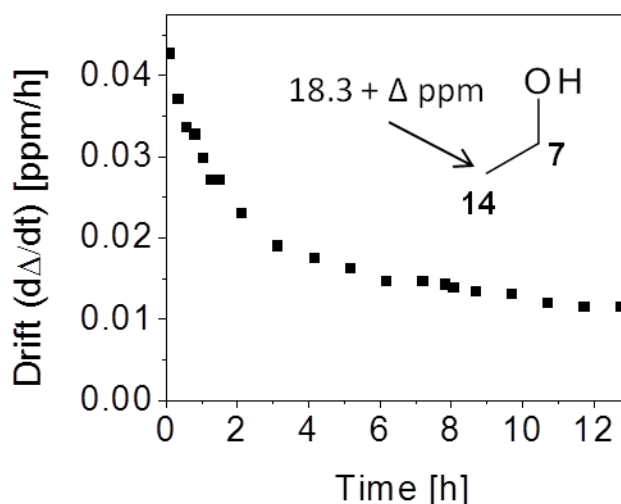


Fig. 2 Reference peak (CH_3 of EtOH: 18.3 ppm vs. TMS) drift in mesophase ^{13}C NMR during gel aging. The final, constant drift is due to the quasi-linear field drift in the superconducting magnet field

2.1.3 Epoxide Ring-Opening in H_2O -Free Sols

^1H NMR of gel precursors *without* H_2O (Fig. 3) shows that epoxide ring-opening *does* occur even in the absence of an acidic metal hydrate at the least-substituted epoxide carbon, consistent with Lewis-acid-catalyzed ring-opening [24]. This reaction is evident in the color changes that occurred when adding ECH to VOCl_3 solutions: orange to yellow in the absence of EtOH (solution b3 and b4 in Fig. 3b) and red to yellow in the

presence of EtOH (solution b1 and b2). Solution b1 (Fig. 3b), a standard sol formulation without H₂O, clearly shows the formation of DCPH, but, while the absence of significant susceptibility broadening improves peak resolution as compared to mesophase NMR, several peaks lay within a small chemical shift range, ca. 3.5–3.7 ppm, overlapping with the intense EtOH methylene (peak 7).

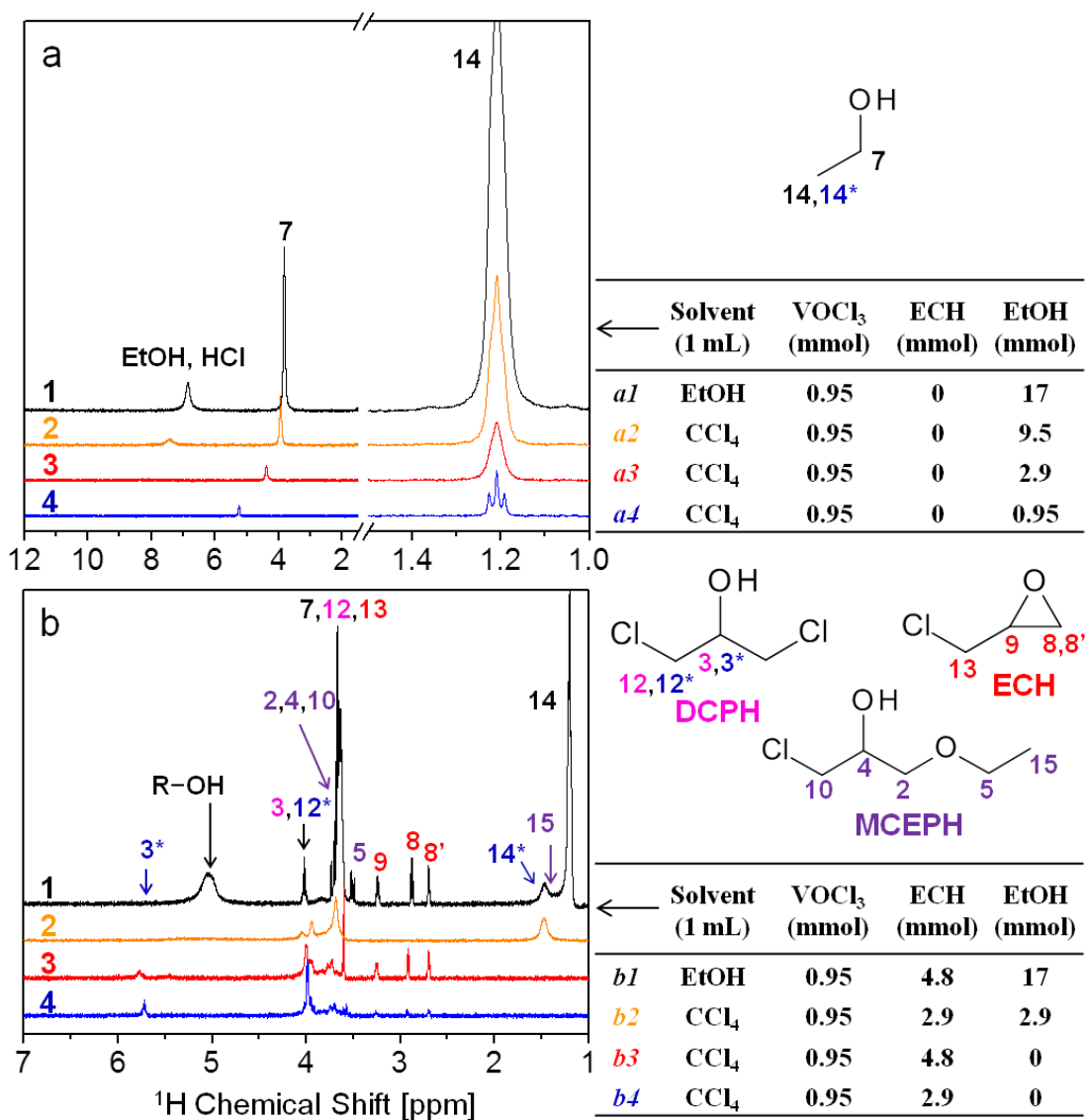
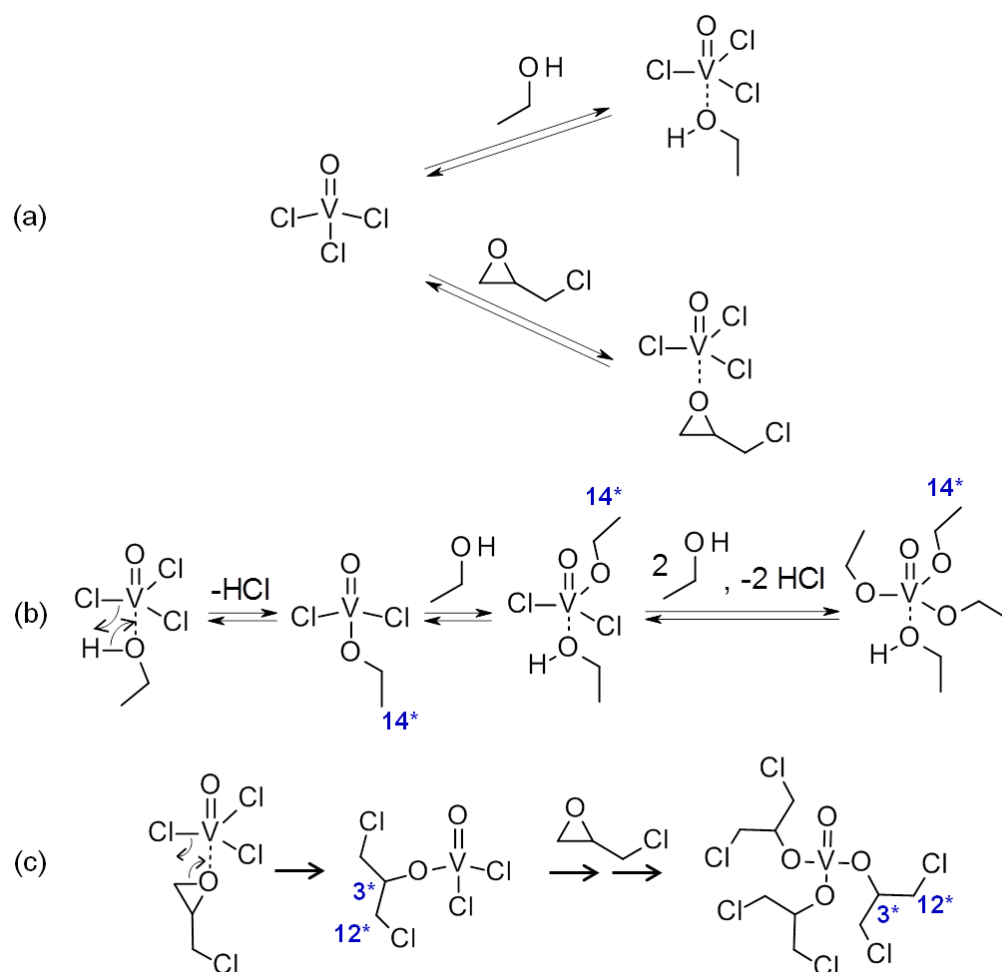


Fig. 3 ¹H NMR of H₂O-free sols shows the inductive effect of V^V and exchange broadening in EtO⁻-V^V chelates (a) and ECH ring-opening in the absence of H₂O and H⁺ (b). Peaks associated with V^V chelates are labeled (3*, 12*, 14*)

Weak, rapidly exchanging V^V chelates, commonly five-coordinate [8, 9, 21], are known to occur in monodentate alcohols and mixed H_2O -alcohol solvent systems, the most pertinent of which here are the EtOH and ECH adducts of $VOCl_3$ (Scheme 3a) which result in $Cl^- \leftrightarrow EtO^-$ ligand exchange (Scheme 3b) and epoxide ring-opening (Scheme 3c). 1H NMR of $VOCl_3$ -EtOH chelates undergoing ligand exchange (Scheme 3b) in CCl_4 , a non-coordinating, 1H -signal-free solvent (Fig. 3a), illustrates the electron-withdrawing effect of V^V on alkoxy ligands [33]. Since alkoxy and halide ligands undergo rapid exchange in solution [8, 21, 33], the observed chemical shift of the EtOH peaks is the time-weighted average of the chemical shift of $EtO^-/EtOH$ ligands and free EtOH. The downfield shift of the EtOH methylene (Fig. 3a, peak 7) relative to the EtOH methyl reference (Fig. 3a, peak 14) is indicative of the inductive effect of the V^V center and increases as each exchangeable EtOH spends more time on average attached to V^V . As expected, this shift is greatest in $VOCl_3$ - CCl_4 solutions with the lowest EtOH/ $VOCl_3$ ratio (Fig. 3a, solution a4), since nearly all of the EtOH is chelated to V^V and undergoing minimal exchange. The fact that the CH_3 triplet (Fig. 3a, peak 14) is only resolved in the solution in which ligands undergo the least amount of exchange (Fig. 3a, solution a4) indicates that exchange broadening, in contrast to electronic or magnetic effects from the V^V center, is the dominant broadening mechanism in these systems. We can then infer that species with well-resolved peaks do not exchange significantly between the bulk solution and V^V ligand shell. This conclusion is consistent with the observed peak resolutions in solutions *b1* (Fig. 3b), where due to its high concentration EtOH is effectively the sole ligand, and *b2* (Fig. 3b), where DCPH and EtOH exchange rapidly. Peak 14* in solutions *b1* and *b2* (Fig. 3b) corresponds to $EtO^-/EtOH$ active in ligand

exchange over the timescale of the experiment. The high resolution of the ECH peaks in all cases suggests that ECH coordinates only weakly to V^V , implying that peak 3* (quintet) and peak 12* (doublet) in solutions *b3* and *b4* (Fig. 3b) are attributable to DCP-/DCPH ligands bound to the electron-withdrawing V^V and not an ECH adduct. Additionally, since free Cl^- is unlikely to exist in CCl_4 (Fig. 3b, solutions *b3* and *b4*), epoxide ring-opening likely proceeds through an intramolecular rearrangement in the transitional $VOCl_{3-x}DCP_x$ -ECH adduct (Scheme 3c).



Scheme 3 Formation of 5-coordinate $VOCl_3$ adducts of EtOH and ECH (a), $Cl^- \leftrightarrow EtO^-$ ligand exchange (b), and Lewis acid-catalyzed intramolecular epoxide ring-opening in the absence of free Cl^- in CCl_4 (c) observed via 1H NMR in H_2O -free sols (Fig. 3). Ligand atoms corresponding to peaks observed in Fig. 3b are labeled (3*, 12*, 14*)

2.2 Physical Properties

2.2.1 Nanomorphology, Surface Area, and Porosity

Dried aerogel and xerogel monoliths appear almost black (Scheme 2) and are dark green when powdered. Upon exposure to air for several months, aerogel monoliths become lighter in color and noticeably green. This change can be temporarily reversed by heating the monoliths to 100 °C under vacuum for 24 h and is attributed to reversible H₂O absorption.

Scanning electron microscopy (SEM) images of VOCl₃/ECH-derived vanadia aerogels (Fig. 4a) show that they are macroporous and possess the same nanoworm micromorphology occasionally seen only in gels fabricated via alkoxide hydrolysis [17, 18]. Transition electron microscopy (TEM) images (Fig. 4b) show small crystalline domains dispersed in an amorphous matrix, consistent with both powder X-ray diffraction (XRD) and electron diffraction (Fig. S.4).

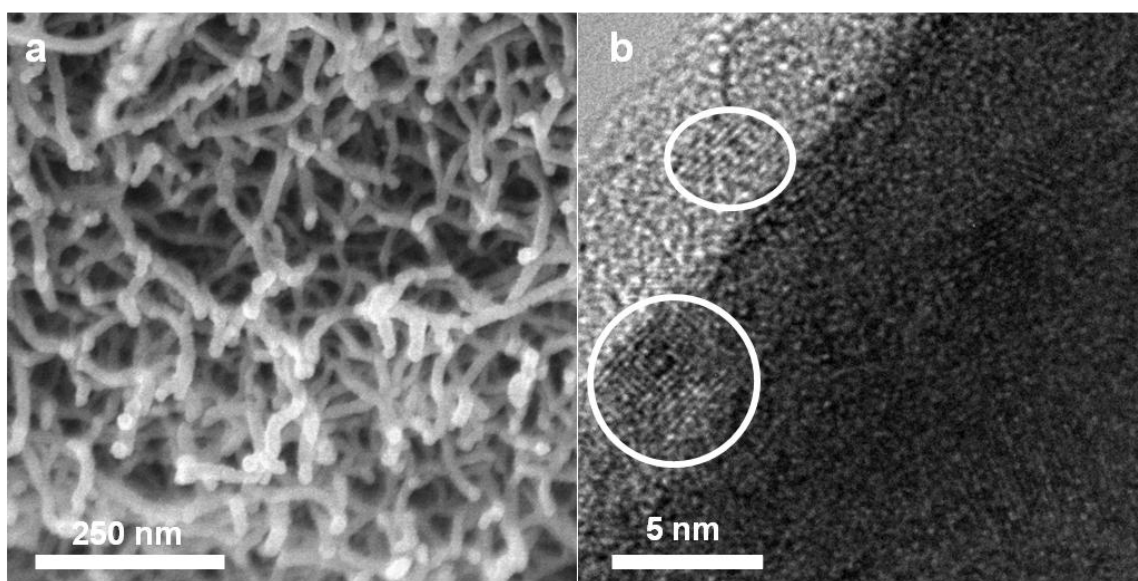


Fig. 4 Representative SEM (a) and TEM (b) images of VO_x aerogels. Several crystalline domains are circled in the TEM image

While the bulk density (ρ_b) of aerogels (Table 3) was easily determined from the sample mass and dimension, the irregular shape of the xerogels made it impossible to determine ρ_b for those samples. The Brunauer–Emmett–Teller (BET) method was used to determine specific surface area (σ_m). BET analysis of N₂-sorption data of aerogels and xerogels (Fig. 5; Table 3) indicates that pores collapse entirely during bench drying. The skeletal density (ρ_s), determined via He pycnometry, of the xerogels is significantly lower than that of the aerogels, indicating the formation of closed pores during ambient drying. X-VO_x aerogels possess a lower BET surface area than their native counterparts, but Barrett–Joyner–Halenda (BJH) analysis suggests that X-VO_x aerogels possess a greater macropore volume. This apparent contradiction is explained by carefully considering the geometric effects of the conformal polymer coating on the VO_x matrix. The conformal coating adds mass, which scales volumetrically, faster than surface area, resulting in a reduced σ_m , while filling in void space, decreasing pore size and shrinking macropores to the point that they exhibit capillary condensation and are observed via BJH analysis. Considering the volumetric surface area of the aerogels ($\sigma_v = \sigma_m \rho_b$), it can be seen that the total surface area of the monoliths increases with crosslinking, as would be expected from a conformal coating. Approximating the VO_x nanoworms as cylinders (Fig. S.5), the width of the nanoworms increases by a factor of 3.21 after crosslinking, sufficient for the observed reduction in macropore size. The density of the polymer coating calculated using this approximation is 1.11 g/cm³, consistent with the skeletal density of polyurea aerogels fabricated from N3200A (1.15 g/cm³) [39], implying that the polymer coating is both conformal and dense.

Table 3 Physical properties of VO_x and X-VO_x gels

	ρ_b [g/cm ³]	ρ_s [g/cm ³]	Porosity ($1-\rho_b/\rho_s$)	σ_m [m ² /g]	σ_v [m ² /cm ³]
VO_x Xerogel	-	2.67	-	0.31	-
VO_x Aerogel	0.103	3.30	0.969	102	10.5
X-VO_x Aerogel	0.412	1.32	0.688	82	34

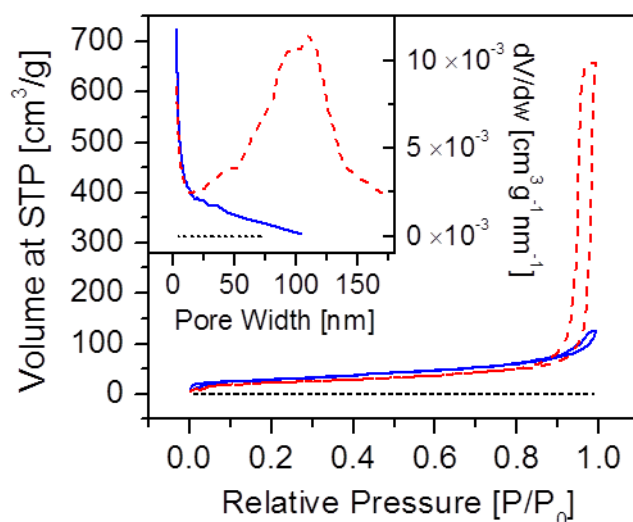


Fig. 5 N₂-sorption isotherms for a VO_x xerogel (black dots), VO_x aerogel (solid blue line), and X-VO_x aerogel (red dashes). Volumetric pore-width (*w*) distribution (*dV/dw*) is determined from BJH analysis inset

2.2.2 Solvent Trapping and H₂O Content

Tandem thermogravimetric analysis–mass spectrometry (TGA-MS) reveals a significant difference between vanadia aerogels and xerogels (Fig. 6). Both gels showed significant mass losses around 100 °C, coincident with the evolution of H₂O (*m/z* = 18), but xerogels show an additional mass loss above 200 °C, corresponding to the release of CO₂ (*m/z* = 44) along with H₂O. Combined with the skeletal density measurements implying closed porosity in the xerogels, it was surmised that these pores are filled with

organic residue, likely acetone, which undergoes complete combustion, possibly catalyzed by vanadia. The possibility that the CO₂ represents physisorbed gas or the decomposition of a carbonate, formed by reaction of CO₂ with the amphoteric oxide, was considered and rejected, as, if that were the case, aerogels (formed by immersion in liquid CO₂) would show a higher relative concentration of CO₂, instead of the negligible amount that is observed. The combustion of residual alkoxide residue commonly seen due to incomplete hydrolysis in vanadia gels [1, 13] made in organic solvents also cannot be the source of CO₂, as in that case aerogels and xerogels would have similar organic content and CO₂ signals. TGA also shows that H₂O content relative to the solid matrix, indicated by the magnitude of the low-temperature mass loss, is the same for both aerogels and xerogels. Since aerogels possess several orders of magnitude higher specific surface area, this H₂O cannot be surface-adsorbed and must be bound *inside* the VO_x skeleton. This H₂O appears to be loosely bound and its removal reversible, as evinced by the color changes observed in aerogel monoliths: dark blue immediately after supercritical fluid drying, green after extended exposure to air, and dark blue again after holding under vacuum at 100 °C.

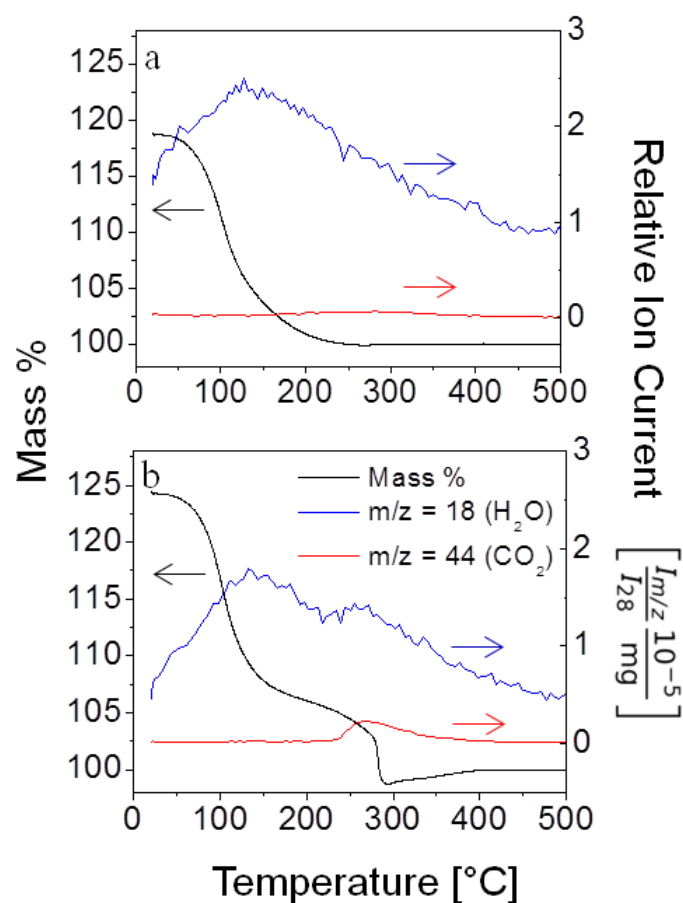


Fig. 6 TGA-MS results for vanadia aerogels (a) and xerogels (b). TGA signal is normalized to the final mass, in order to represent losses as a proportion of the VO_x matrix, which becomes V_2O_5 in all cases.

3 Discussion

The fact that robust, homogeneous gels can be fabricated over a large range of densities only using sols with nominally constant concentrations of ECH and H_2O , which must be added simultaneously, suggests that epoxide ring-opening and hydrolysis occur on similar timescales, unlike what has been previously observed in other metal oxide systems [10–12, 22, 36, 40]. Of perhaps more interest, while it is proposed that acidic transition metal hydrates protonate the epoxide ring before nucleophilic ring-opening

[10–12], ECH ring-opening is observed in the VOCl_3 -ECH system in the absence of H_2O , i.e., absent acidic hydrates, and even in a fully aprotic system, in which protonation is explicitly precluded, implying that epoxide protonation is not necessary for ring-opening. Instead, we propose that V^{V} -Lewis-acid catalysis is responsible for ring-opening in this system even in the presence of H^+ , as evinced by exclusive nucleophilic attack on the less-substituted epoxide carbon. Based on the fact that FeCl_3 also reportedly reacts with PO before the addition of H_2O and the formation of acidic $[\text{Fe}(\text{OH})_6]^{3+}$ during the formation of Fe_2O_3 gels [11], Lewis-acid-catalyzed ring-opening may occur during the epoxide-assisted gelation of other metal oxide gels.

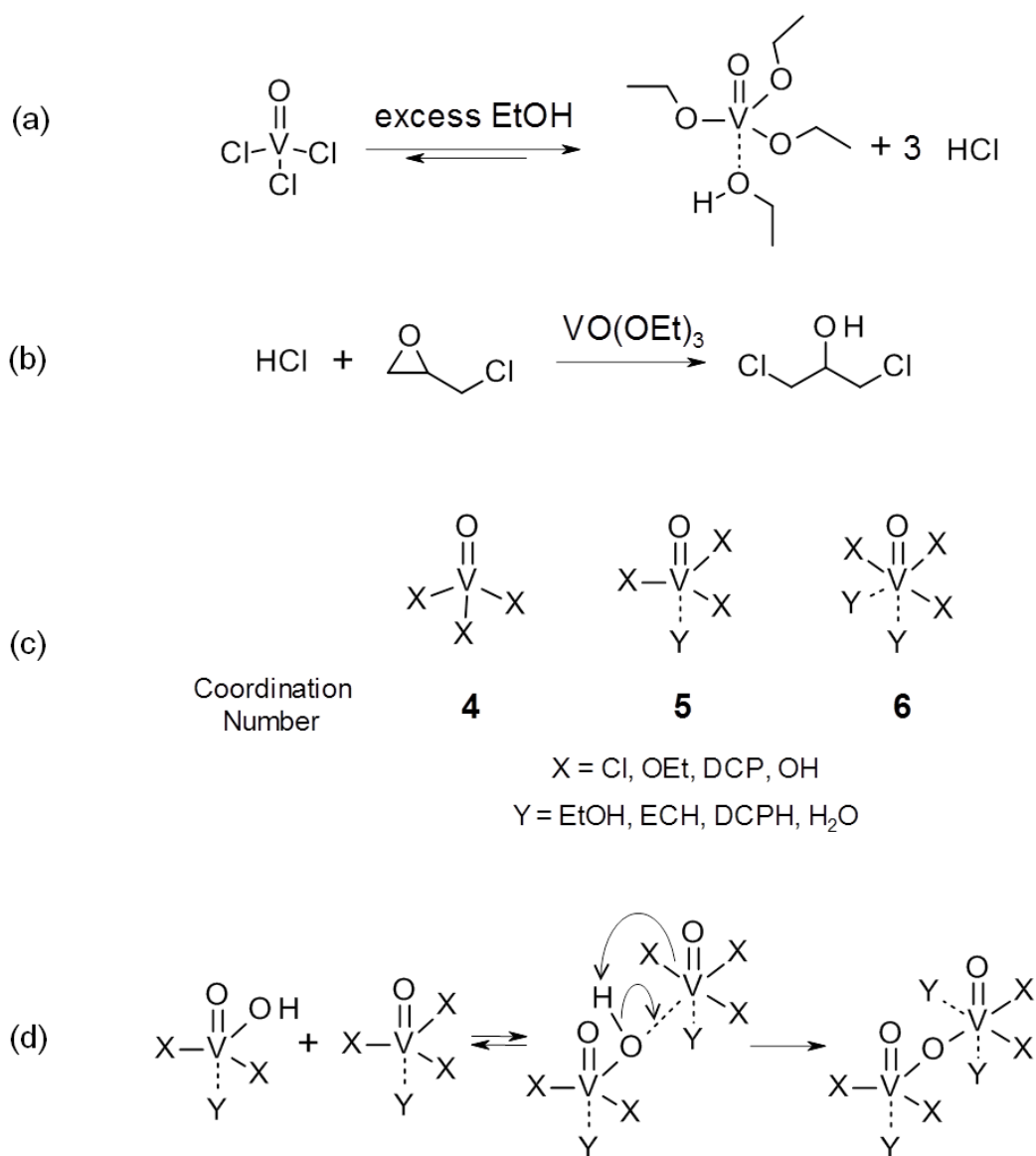
We propose a new gelation sequence (Scheme 4) following four basic steps: (Step 1) $\text{Cl}^- \leftrightarrow \text{EtO}^-$ ligand exchange netting a 5-coordinate vanadyl ethoxide and HCl (Scheme 4a); (Step 2) Lewis-acid-catalyzed ECH ring-opening, consuming H^+ and Cl^- produced during $\text{Cl}^- \leftrightarrow \text{EtO}^-$ exchange (Scheme 4b); (Step 3) additional ligand exchange forming a mixture of 4-, 5-, and 6-coordinate vanadyl(V) species (e.g., $\text{VOX}_3\text{Y}_\alpha$, where X^- is an anionic ligand; Y is a neutral ligand; and α is 0 for 4-coordinate species, 1 for 5-coordinate species, and 2 for 6-coordinate species) (Scheme 4c); and (Step 4) vanadium oxo-polymer formation in the absence of HCl (Scheme 4d). Ligand exchange and V^{V} -adduct formation (Step 1) are well known in H_2O and alcoholic solvents and are directly observed for V^{V} -OEt (Fig. 3b, peak 14*) and V^{V} -DCP (Fig. 3b, peaks 3* and 12*) species through inductive deshielding in ^1H NMR. Lewis-acid-catalyzed ring-opening (Step 2) is observed in CCl_4 , where epoxide protonation is explicitly excluded and can be inferred in EtOH from exclusive nucleophilic attack by Cl^- at the less-substituted epoxide carbon [24]. VOCl_3 - H_2O -EtOH (1:9:18) is stable in the absence of ECH for tens of

minutes and only results in partial precipitation, so gelation (Step 4) which occurs in ~10 s must be driven by the reaction in Step 2. Given that vanadium oxide solubility in H₂O is pH-dependent [1] and vanadyl alkoxides are typically unstable in the presence of water [15–19], we can infer that gelation is driven by the net consumption of HCl as a result of Lewis-acid-catalyzed ECH ring-opening. This mechanism is similar to the hydrolysis of vanadyl alkoxides [15–19], where here the vanadyl alkoxide is generated in situ from VOCl₃ and ECH.

Scheme 4 only accounts for the formation of the initial red V₂O₅•xH₂O gel [1] and comes with several caveats. EtOH, DCPH, and H₂O (and their anionic counterparts) are all competing ligands at relatively high concentrations (6:1:3 by mol, respectively), so VOX₃:Y_α species in solution likely contain a mixture of all three, in addition to the possibility of cationic and anionic V^V species. Dimers and oligomers of V^V species with small ligands are also well known [21, 8], adding mixed-ligand oligomers to the list of species in solution. ECH ring-opening (Step 2) and vanadium oxide polymerization (Step 4) also occur on similar timescales, meaning that the stepwise mechanism proposed above is overly simplistic. The high gelation rate (instability of intermediates) complicates any analyses necessary for such subtle determinations as explicit identification of the V^V species directly responsible for gelation or the precise ring-opening intermediate, which are beyond the scope of this study.

In addition to the primary gelation scheme discussed above, the intermediate fluid phase of the lowest density gel suggests multiple discreet processes take place at disparate timescales in all vanadia gels. After the (fast) formation of a red V₂O₅•xH₂O gel, partial or complete dissolution of the V^V oxide matrix occurs in concert with or

followed by $V^V \rightarrow V^{IV}$ reduction by EtOH. Gelation (and/or precipitation) of a blue-green $V^{IV/V}$ oxide, possibly driven by changes in solvent properties brought on during CH hydrolysis and ethanolysis, results in the final observed wet-gels which were further processed into VO_x and $X-VO_x$ aerogels and xerogels.



Scheme 4 Proposed reaction mechanism for gelation in the $VOCl_3$ -ECH-EtOH system involving ligand exchange in EtOH (a); Lewis-acid-catalyzed ECH ring-opening (b); neutral 4-, 5-, and 6-coordinate species potentially formed during additional ligand exchange (c); and a possible mechanism for the polymerization of vanadium oxide viaolation of a 5-coordinate vanadyl hydroxide (d)

While there is little doubt that $V^V \rightarrow V^{IV}$ reduction occurs, evinced by: (a) the gel color change, (b) the formation of acetaldehyde, and (c) the magnetic susceptibility evolution, the exact degree of reduction has proven difficult to quantify; sol-gel vanadia is not stable under conditions necessary for measurement, e.g., aqueous redox titration [8], XPS, or laser Raman spectroscopy. Nevertheless, the significantly darker color of the dried gels and their dispersed solids (e.g., in preparation for TEM) as compared to previously synthesized gels made from vanadium oxytripropoxide suggests that significantly more reduction occurs in those made from $VOCl_3$ and ECH in EtOH, likely reflective of efficient V^V -EtOH redox chemistry [34].

VO_x gels formed through epoxide-assisted gelation exhibit several other differences from their alkoxide counterparts. Wet vanadia gels synthesized via epoxide-assisted gelation are sturdier (easier to handle during solvent exchange) and exhibit less optical scattering than their alkoxide counterparts. While the X- VO_x aerogels synthesized here possess mechanical properties similar to previously synthesized X- VO_x aerogels (Fig. S.6), mechanical failure occurred at a lower strain in those synthesized via epoxide-assisted gelation. This premature failure is attributed to internal voids, which are not present in aerogels synthesized via the hydrolysis of vanadium oxytripropoxide [17, 18]. It is suspected that these voids are formed by solvent vaporization during exothermic reactions.

4 Conclusion

Vanadia aerogels fabricated via epoxide-assisted gelation utilizing $VOCl_3$ and ECH resemble those fabricated via alkoxide hydrolysis at approximately one-tenth of the cost. The gels synthesized via epoxide-assisted gelation in fact appear superior to their

alkoxide counterparts in both optical quality and robustness (as wet-gels), though they are prone to the formation of internal voids and likely possess a different average oxidation state [17, 18]. Results also indicate that ECH ring-opening occurs through Lewis-acid catalysis, unlike what is seen in other transition metal oxide gels.

5 Experimental Section

All reagents were used as received without further purification.

5.1 Aerogel and Xerogel Synthesis

A typical gel was fabricated as follows: 0.540 mL (5.71 mmol) of VOCl_3 (99 %, Strem Chemicals) was dissolved in 3.00 mL (51.4 mmol) of absolute ethanol (EtOH) (LyondellBasell) and cooled to 0 °C in an ice bath. In a separate container, 2.25 mL (28.6 mmol) of ECH (99 %, Acros Organics) and 0.925 mL (51.4 mmol) of deionized H_2O were dissolved in the same amount of EtOH (3.00 mL) and cooled to 0 °C in an ice bath. The two solutions were mixed and swirled vigorously before immediately pouring into syringe molds. Within 10 s, solid red gels were formed, which were aged for 5 days at ambient temperature before further processing. PO (C99 %, Sigma-Aldrich), GLY (96 %, Acros), and DMO (98 %, Sigma-Aldrich) were substituted for ECH in some cases to investigate their effects on gelation rate.

Solvent exchange and isocyanate crosslinking procedures were followed according to those previously reported in the literature [17, 18]. Gels were placed in acetone (Technical Grade, Univar) for 8 h to exchange residual solvent. Solvent exchange was repeated 3 times. Xerogels were formed by drying acetone-exchanged wet-gels under

ambient conditions for several days followed by placing samples under vacuum for 6 h at 50 °C to remove residual acetone. Aerogels were prepared by placing acetone-exchanged wet-gels in an autoclave, exchanging residual solvent with liquid CO₂, taking the autoclave above the supercritical point of CO₂, and finally venting the CO₂ isothermally at 40 °C. Mechanically strong X-VO_x aerogels (Fig. S.6) were formed using a solution of 5.5 g Desmodur N3200A (courtesy of Bayer Corp.) in 94 mL of dry acetone (CHROMASOLV for HPLC, Sigma-Aldrich), followed by solvent exchange in acetone baths and supercritical CO₂ drying.

5.2 Materials Characterization

Absorption spectra of wet-gels and precursor sols were on an Ocean Optics Chem 2000 UV–Vis spectrometer with a deuterium lamp source. Short-path-length cuvettes (to limit absorption) were fabricated using two glass microscope slides (Corning) affixed with epoxy, using a plastic sheet (20–30 μm) as a temporary spacer during epoxy curing. Cuvettes were sealed with Parafilm after filling with sols to prevent solvent evaporation and hydrolysis.

Mesophase ¹H (400 MHz) and ¹³C (100 MHz) NMR was performed on wet-gels using a Varian Unity Inova spectrometer without ²H locking, due to the absence of a deuterated solvent. An inverse-gated ¹H decoupling sequence was used for ¹³C NMR in order to obtain quantitative peak integrals. The terminal CH₃ on EtOH [18.3 ppm (¹³C) and 1.21 ppm (¹H) vs. tetramethylsilane (TMS)] was used as an internal reference. Peak assignments were determined using experimental data from the Spectral Database for Organic Compounds [41].

H₂O-free CCl₄ and EtOH solutions of VOCl₃ with various amounts of ECH for ¹H NMR were made by dissolving 0.090 mL (0.95 mmol) of VOCl₃ in 1.00 mL of the appropriate solvent (CCl₄ or EtOH) to which ECH (0, 2.95, 4.75 mol) and/or EtOH (0, 0.95, 2.85 mol) was added. The terminal CH₃ on EtOH (1.21 ppm vs. TMS) and the highfield proton on ECH (2.70 vs. TMS) were used as internal references.

Nanomorphology was analyzed using cross sections mounted in a Hitachi S-4700 SEM. Monoliths were ground to a fine powder using a mortar and pestle before performing XRD with a PANalytical X'Pert Pro Multi-Purpose Diffractometer, using a Cu K_α (λ = 1.54 Å) radiation source. Ground powders were dispersed in acetone and deposited onto a silky-carbon-coated Cu grid for TEM and electron diffraction on a Technai F20 STEM.

The bulk density (ρ_b) of aerogels was determined from sample mass and dimensions. The skeletal density (ρ_s) was determined via He pycnometry using a Micromeritics AccuPyc II 1340. N₂-sorption porosimetry was carried out on a Micromeritics ASAP 2020 surface area and porosity analyzer using monoliths broken into small chunks. Specific surface area was determined using the BET method, and the pore size distribution was determined using the BJH method. Prior to pycnometry and porosimetry measurements, samples were dried for 12 h at 80 °C under vacuum.

Quasi-static compression tests were conducted on an MTS-810 servo-hydraulic testing machine, following the testing procedures and specimen length-to-diameter ratio in ASTM D1621-04a (Standard Test Method for Compressive Properties of Rigid Cellular Plastics). The specimens had a diameter of 13.75 mm and a length/diameter ratio of one.

TGA-MS was carried out on a Netzsch STA 409 C thermogravimetric analyzer connected via a fused silica capillary to a QMS 403 C mass spectrometer under air at a heating rate of 5 °C/min. Ion currents were monitored for $15 < m/z < 300$. Signals were normalized by carrier gas ion current (N_2 , $m/z = 28$) and sample mass for comparison between runs. Only signals for $m/z = 18$ and $m/z = 44$ were detectable above background (Fig. S.7).

Acknowledgements T. M. F. would like to thank Dr. Shruti Mahadik-Khanolkar for her expertise in synthesizing vanadia aerogels, Dr. H. Lu (of The University of Texas-Dallas) for quasi-static compression measurements, and Dr. Chakkaravarthy Chidambareswarapattar for N_2 porosimetry measurements. The authors would also like to thank Bayer Corporation, USA, for their generous supply of Desmodur N3200A isocyanate.

Funding This project was funded by the Army Research Office (W911NF-14-1-0369). The Materials Research Center of Missouri S&T provided partial support with materials characterization. Student support was provided in part by the National Science Foundation through a University of Missouri Neutron Scattering IGERT Traineeship (Grant DGE-1069091).

Conflict Of Interest The authors declare that they have no conflict of interest.

References

1. Livage J (1991) Vanadium pentoxide gels. *Chemistry of Materials* 3:578-593.
2. Pergament A, Stefanovich G, Berezina O, Kirienko D (2013) Electrical conductivity of tungsten doped vanadium dioxide obtained by the sol-gel technique. *Thin Solid Films* 531:572-576.
3. Fontenot CJ, Wiench JW, Pruski M, Schrader GL (2000) Vanadia Gel Synthesis via Peroxovanadate Precursors. 1. In Situ Laser Raman and ^{51}V NMR Characterization of the Gelation Process. *The Journal of Physical Chemistry B* 104:11622-11631.
4. Fontenot CJ, Wiench JW, Pruski M, Schrader GL (2001) Vanadia Gel Synthesis via Peroxovanadate Precursors. 2. Characterization of the Gels. *The Journal of Physical Chemistry B* 105:10496-10504.
5. Livage J, Guzman G, Beteille F, Davidson P (1997) Optical properties of sol-gel derived vanadium oxide films. *Journal of Sol-Gel Science and Technology* 8:857-865.
6. Lee C-Y, Marschilok AC, Subramanian A, Takeuchi KJ, Takeuchi ES (2011) Synthesis and characterization of sodium vanadium oxide gels: the effects of water (n) and sodium (x) content on the electrochemistry of $\text{Na}_x\text{V}_2\text{O}_5 \cdot n\text{H}_2\text{O}$. *Physical Chemistry Chemical Physics* 13:18047-18054.
7. Carn F, Steunou N, Livage J, Colin A, Backov R (2005) Tailor-Made Macroporous Vanadium Oxide Foams. *Chemistry of Materials* 17:644-649.
8. Crans DC, Tracey AS (1998) The Chemistry of Vanadium in Aqueous and Nonaqueous Solution. *Vanadium Compounds*, vol 711. ACS Symposium Series, vol 711. American Chemical Society, pp 2-29.
9. Crans DC (2005) Fifteen years of dancing with vanadium. *Pure and Applied Chemistry* 77:1497-1527.
10. Leventis N, Vassilaras P, Fabrizio EF, Dass A (2007) Polymer nanoencapsulated rare earth aerogels: chemically complex but stoichiometrically similar core-shell superstructures with skeletal properties of pure compounds. *Journal of Materials Chemistry* 17:1502-1508.
11. Gash AE, Tillotson TM, Satcher JH, Poco JF, Hrubesh LW, Simpson RL (2001) Use of Epoxides in the Sol-Gel Synthesis of Porous Iron(III) Oxide Monoliths from Fe(III) Salts. *Chemistry of Materials* 13:999-1007.
12. Gash AE, Tillotson TM, Satcher Jr JH, Hrubesh LW, Simpson RL (2001) New sol-gel synthetic route to transition and main-group metal oxide aerogels using inorganic salt precursors. *Journal of Non-Crystalline Solids* 285:22-28.

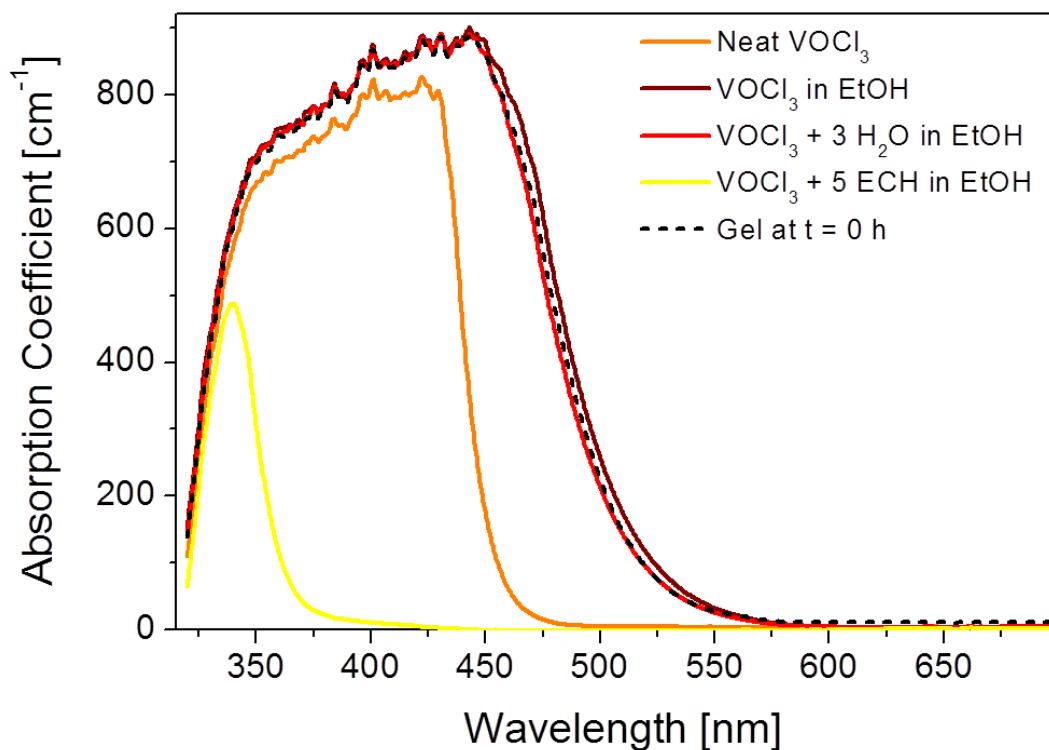
13. Guzman G, Morineau R, Livage J (1994) Synthesis of vanadium dioxide thin films from vanadium alkoxides. *Materials Research Bulletin* 29:509-515.
14. Livage J (1996) Sol-gel chemistry and electrochemical properties of vanadium oxide gels. *Solid State Ionics* 86–88, Part 2:935-942.
15. Augustyn V, Dunn B (2010) Vanadium oxide aerogels: Nanostructured materials for enhanced energy storage. *Comptes Rendus Chimie* 13:130-141.
16. Chaput F, Dunn B, Fuqua P, Salloux K (1995) Synthesis and characterization of vanadium oxide aerogels. *Journal of Non-Crystalline Solids* 188:11-18.
17. Leventis N, Sotiriou-Leventis C, Mulik S, Dass A, Schnobrich J, Hobbs A, Fabrizio EF, Luo H, Churu G, Zhang Y, Lu H (2008) Polymer nanoencapsulated mesoporous vanadia with unusual ductility at cryogenic temperatures. *Journal of Materials Chemistry* 18:2475-2482.
18. Luo H, Churu G, Fabrizio EF, Schnobrich J, Hobbs A, Dass A, Mulik S, Zhang Y, Grady BP, Capeceelatro A, Sotiriou-Leventis C, Lu H, Leventis N (2008) Synthesis and characterization of the physical, chemical and mechanical properties of isocyanate-crosslinked vanadia aerogels. *Journal of Sol-Gel Science and Technology* 48:113-134.
19. Li H, He P, Wang Y, Hosono E, Zhou H (2011) High-surface vanadium oxides with large capacities for lithium-ion batteries: from hydrated aerogel to nanocrystalline VO₂(B), V₆O₁₃ and V₂O₅. *Journal of Materials Chemistry* 21:10999-11009.
20. Nag J, Haglund RFJ (2008) Synthesis of vanadium dioxide thin films and nanoparticles. *Journal of Physics: Condensed Matter* 20:264016
21. Crans DC, Felty RA, Chen H, Eckert H, Das N (1994) Oxovanadium(V) Alkoxide Derivatives of 1,2-Diols: Synthesis and Solid-State ⁵¹V NMR Characterization. *Inorganic Chemistry* 33:2427-2438.
22. Baumann T, Gash A, Satcher J, Jr. (2011) A Robust Approach to Inorganic Aerogels: The Use of Epoxides in Sol–Gel Synthesis. In: Aegerter MA, Leventis N, Koebel MM (eds) *Aerogels Handbook. Advances in Sol-Gel Derived Materials and Technologies*. Springer New York, pp 155-170.
23. Parker RE, Isaacs NS (1959) Mechanisms Of Epoxide Reactions. *Chemical Reviews* 59:737-799.
24. Carey FA, Sundberg RJ (2007) *Advanced Organic Chemistry: Part B: Reaction and Synthesis*. *Advanced Organic Chemistry / Part B: Reactions and Synthesis*. Springer.

25. Sigma-Aldrich. <https://www.sigmaaldrich.com/united-states.html>. Accessed March 10, 2015
26. Anderson WP, Edwards WD, Zerner MC (1986) Calculated spectra of hydrated ions of the first transition-metal series. *Inorganic Chemistry* 25:2728-2732.
27. So H, Pope MT (1972) Origin of some charge-transfer spectra. Oxo compounds of vanadium, molybdenum, tungsten, and niobium including heteropoly anions and heteropoly blues. *Inorganic Chemistry* 11:1441-1443.
28. Cornman CR, Colpas GJ, Hoeschele JD, Kampf J, Pecoraro VL (1992) Implications for the spectroscopic assignment of vanadium biomolecules: structural and spectroscopic characterization of monooxovanadium(V) complexes containing catecholate and hydroximate based noninnocent ligands. *Journal of the American Chemical Society* 114:9925-9933.
29. Rehder D, Weidemann C, Duch A, Pribsch W (1988) Vanadium-51 shielding in vanadium(V) complexes: a reference scale for vanadium binding sites in biomolecules. *Inorganic Chemistry* 27:584-587.
30. Crans DC, Felty RA, Anderson OP, Miller MM (1993) Structure and solution properties of a dimeric tetrahedral vanadium(V) chloride alkoxide complex. *Inorganic Chemistry* 32:247-248.
31. Carrano CJ, Mohan M, Holmes SM, de la Rosa R, Butler A, Charnock JM, Garner CD (1994) Oxovanadium(V) Alkoxo-Chloro Complexes of the Hydridotripyrazolylborates as Models for the Binding Site in Bromoperoxidase. *Inorganic Chemistry* 33:646-655.
32. Abernethy CD, Codd GM, Spicer MD, Taylor MK (2003) A Highly Stable N-Heterocyclic Carbene Complex of Trichloro-oxo-vanadium(V) Displaying Novel Cl-Ccarbene Bonding Interactions. *Journal of the American Chemical Society* 125:1128-1129.
33. Crans DC, Chen H, Felty RA (1992) Synthesis and reactivity of oxovanadium(V) trialkoxides of bulky and chiral alcohols. *Journal of the American Chemical Society* 114:4543-4550.
34. Bobtelsky M, Glasner A (1942) The Rate of Reduction of Vanadium Pentoxide in Concentrated Acid Solutions. Reduction of Vanadium Pentoxide by Arsenious Acid, Oxalic Acid, Formaldehyde and Ethyl Alcohol. *Journal of the American Chemical Society* 64:1462-1469.
35. Fritsch HT, Schieberle P (2005) Identification Based on Quantitative Measurements and Aroma Recombination of the Character Impact Odorants in a Bavarian Pilsner-type Beer. *Journal of Agricultural and Food Chemistry* 53:7544-7551.

36. Gash AE, Satcher JH, Simpson RL (2003) Strong akaganeite aerogel monoliths using epoxides: Synthesis and characterization. *Chemistry of materials* 15:3268-3275.
37. Pemberton C, Hoffman R, Aserin A, Garti N (2011) New insights into silica-based NMR “chromatography”. *Journal of Magnetic Resonance* 208:262-269.
38. Evans DF (1959) 400. The determination of the paramagnetic susceptibility of substances in solution by nuclear magnetic resonance. *Journal of the Chemical Society (Resumed)*:2003-2005.
39. Leventis N, Sotiriou-Leventis C, Chandrasekaran N, Mulik S, Larimore ZJ, Lu H, Churu G, Mang JT (2010) Multifunctional Polyurea Aerogels from Isocyanates and Water. A Structure–Property Case Study. *Chemistry of Materials* 22:6692-6710.
40. Baumann TF, Gash AE, Chinn SC, Sawvel AM, Maxwell RS, Satcher JH (2005) Synthesis of High-Surface-Area Alumina Aerogels without the Use of Alkoxide Precursors. *Chemistry of Materials* 17:395-401.
41. Debbie CC, Alan ST (1998) The Chemistry of Vanadium in Aqueous and Nonaqueous Solution. *Vanadium Compounds*, vol 711. ACS Symposium Series, vol 711. American Chemical Society, pp 2-29.
42. SDBSWeb. National Institute of Advanced Industrial Science and Technology. <http://sdb.sriodb.aist.go.jp>. Accessed 06/15/15

Electronic Supplementary Material

Contents:		Page
Figure S.1	UV-Vis absorption spectra of VOCl_3 solutions	65
Figure S.2	UV-Vis absorption spectra collected during gel aging	66
Figure S.3	Concentration study from time-resolved ^{13}C NMR collected during gel aging	67
Figure S.4	XRD and electron diffraction patterns of aerogel powders	68
Figure S.5	Concentric cylinder model used to calculate crosslinking polymer density	69
Figure S.6	Quasi-static compression of X- VO_x aerogels	70
Figure S.7	Full mass spectrometry data from tandem TGA-MS	71
References		72



Spectrum	EtOH [mL]	VOCl ₃ [mmol]	H ₂ O [mmol]	ECH [mmol]	Apparent Color
Neat VOCl ₃	-	Neat	-	-	Orange
VOCl ₃ in EtOH	6.0	5.70	-	-	Red
VOCl ₃ + 3 H ₂ O in EtOH	6.0	5.70	17.1	-	Red
VOCl ₃ + 5 ECH in EtOH	6.0	5.70	-	28.5	Yellow
Gel at t = 0	6.0	5.70	51.3	28.5	Red

Figure S.1 UV-Vis absorption spectra comparing several VOCl₃ solutions and a wet gel, assuming a 25 μm path length. The major absorption in the visible spectrum is due to a metal-to-ligand charge-transfer transition.

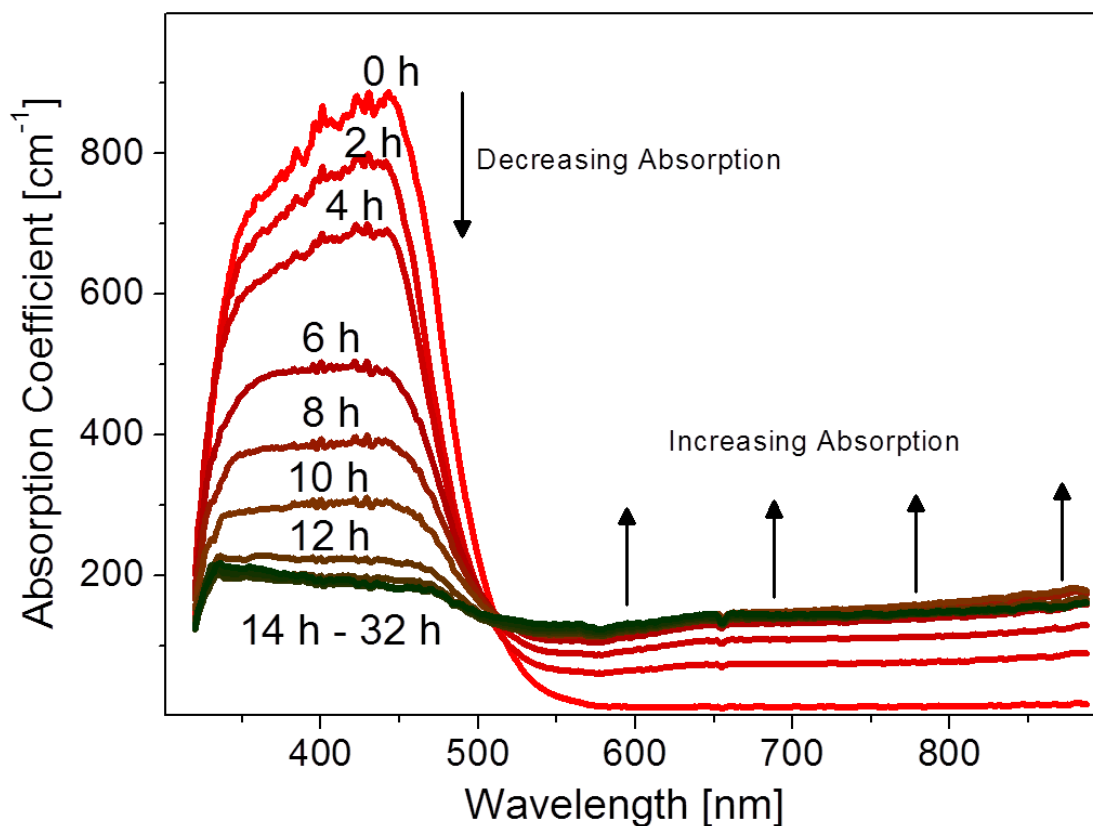
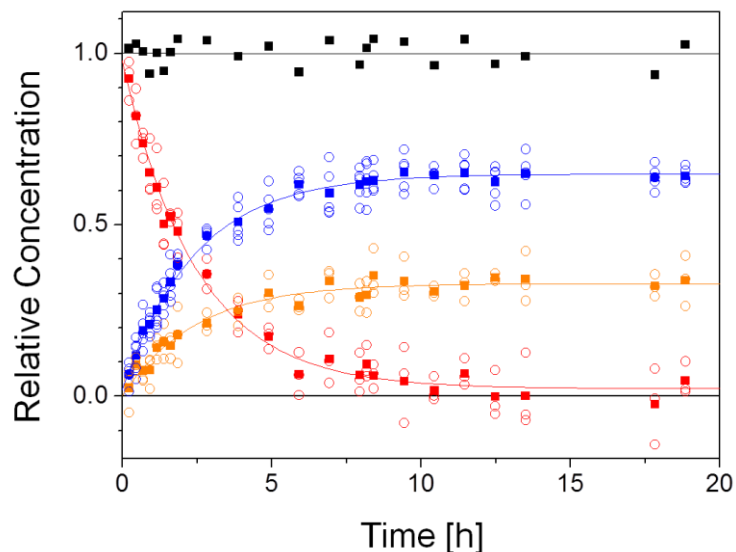


Figure S.2 UV-Vis absorption spectra of standard epoxide gel during aging, assuming a 25 μm path length. No significant changes to absorption were detected after ~ 16 h. Strong absorption in the near UV gives rise to the initial red gel color. The onset of intense gel color causes gels to lose transparency.



$C = A_0 + Ae^{-kt}$				
	k [h^{-1}] (Independently Fit)	k [h^{-1}] (Constrained Fit)	Initial Relative Concentration (A $+A_0$)	Final Relative Concentration (A_0)
ECH	0.400		0.977	0.022
MCPDH₂	0.364		0.003	0.329
MCEPH	0.433	0.406	0.021	0.649
Sum	2.83×10^{-30}		1.001	1.000

Figure S.3 Concentration (C) of ECH (red), MCPDH₂ (orange), MCEPH (blue) and their Sum (black) as a function of time (t) as monitored by ¹³C NMR. Individual peak intensities (open circles) were averaged (solid squares) to determine the concentration of each species. All intensities were normalized to the time-averaged **Sum** to determine relative concentration. Data for each species was initially fit independently to an exponential decay. Noting that each of the rate constants (k) was similar—excepting the **Sum** series, for which $k \approx 0$ —this parameter was constrained to be identical for each species and the data was refit. The fits (solid line) are excellent ($R^2 = 0.994$) and physically consistent, i.e., the sum of the fitted concentrations matches the fit of **Sum**, which has negligible ($A = 8.81566 \times 10^{-4}$) exponential character. This result indicates that ECH ring-opening is first-order with respect to ECH concentration. As both H₂O and EtOH are present in large excess, changes in their concentration by consumption during ring-opening would have little effect on the observed kinetics.

This demonstrates that concentration curves can be determined via *in situ* mesophase ¹³C NMR for analysis of slow gelation kinetics, even in the presence of poor signal to noise caused by low concentrations and anisotropic susceptibility broadening.

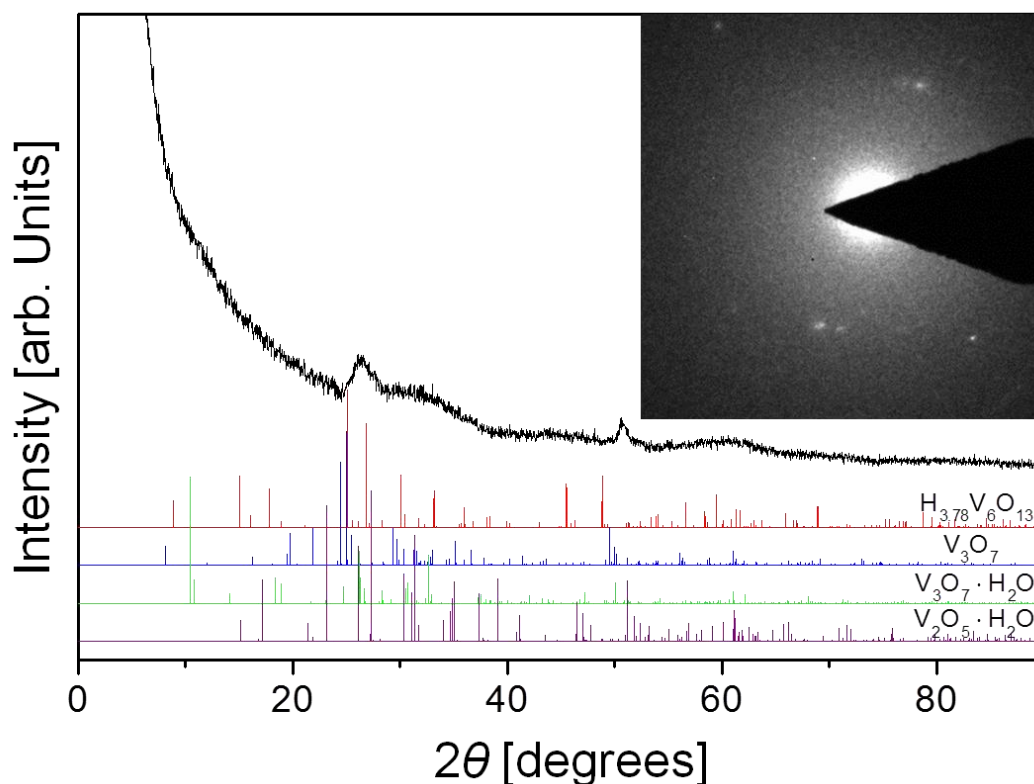


Figure S.4 X-ray (Cu- K_{α}) diffraction pattern of a ground vanadia aerogel monolith. Stick patterns for a series of potential $\text{VO}_x \cdot n\text{H}_2\text{O}$ species are included for comparison: $\text{V}_2\text{O}_5 \cdot \text{H}_2\text{O}$ (PDF# 01-074-3093), $\text{V}_3\text{O}_7 \cdot \text{H}_2\text{O}$ (01-085-2401), V_3O_7 (01-71-0454), $\text{H}_{3.78}\text{V}_6\text{O}_{13}$ (01-088-1753 38-8). Electron diffraction pattern inset.

The peaks in the X-ray diffraction pattern are in locations similar to several known VO_x materials, but the broad low-intensity peaks are more consistent with an amorphous material. (A detailed analysis of the diffuse scattering and determination of a model pair distribution function (PDF) is beyond the scope of this study.) The electron diffraction pattern and TEM image (Fig. 4B) suggest that some intermittent nanocrystalline domains are present. A good single-crystal electron diffraction pattern was not obtainable, due in part to multiple scattering from the amorphous matrix. The scarcity of the nanocrystals also precludes the collection of a quality powder electron diffraction pattern.

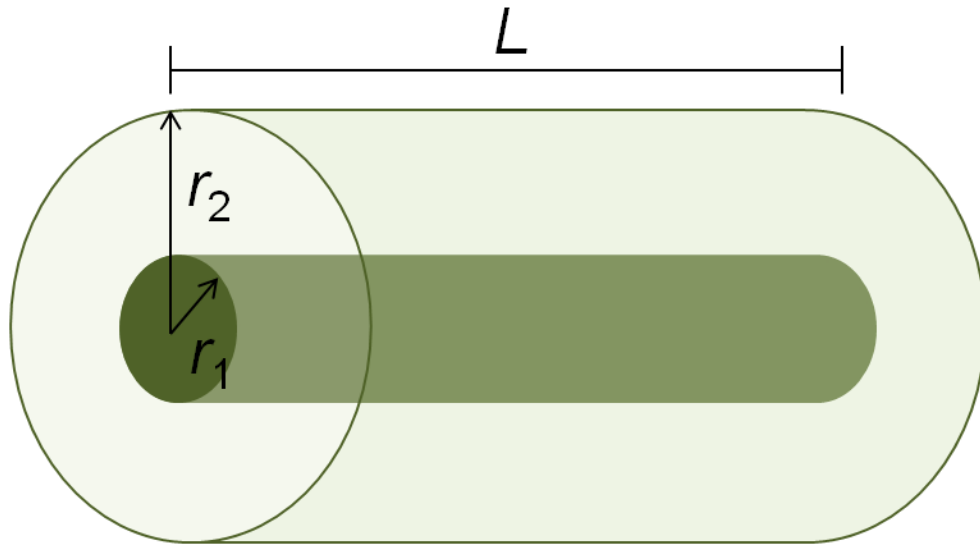


Figure S.5 Conformally coated cylindrical VO_x nanoworm approximation used to calculate polymer coating density, where r_1 and r_2 are the radii of the nanoworms and before and after isocyanate crosslinking, respectively and L is the length of the nanoworms. Since conformal crosslinking only adds onto existing nanoworms, the ratio of the radii can be determined from the ratio of the volumetric surface area, σ_v :

$$\frac{r_2}{r_1} = \frac{2\pi r_2 L}{2\pi r_1 L} = \frac{\sigma_{v,2}}{\sigma_{v,1}} = \frac{33.7}{10.5} = 3.21$$

The skeletal density of the composite nanoworm, $\rho_{s,T}$, is the average of the skeletal density of the composite parts, $\rho_{s,1}$ and $\rho_{s,2}$, weighted by their respective volumes, V_1 and V_2 :

$$\begin{aligned} \rho_{s,T} = 1.32 &= \frac{\rho_{s,1}V_1 + \rho_{s,2}V_2}{V_1 + V_2} = \frac{\rho_{s,1}2\pi r_1^2 L + \rho_{s,2}2\pi(r_2^2 - r_1^2)L}{2\pi r_2^2 L} \\ &= \frac{3.30r_1^2 + \rho_{s,2}((3.21r_1)^2 - r_1^2)}{(3.21r_1)^2} = \frac{3.30 + 9.30\rho_{s,2}}{10.3} \Rightarrow \rho_{s,2} \\ &= 1.11 \text{ [g/cm}^3\text{]} \end{aligned}$$

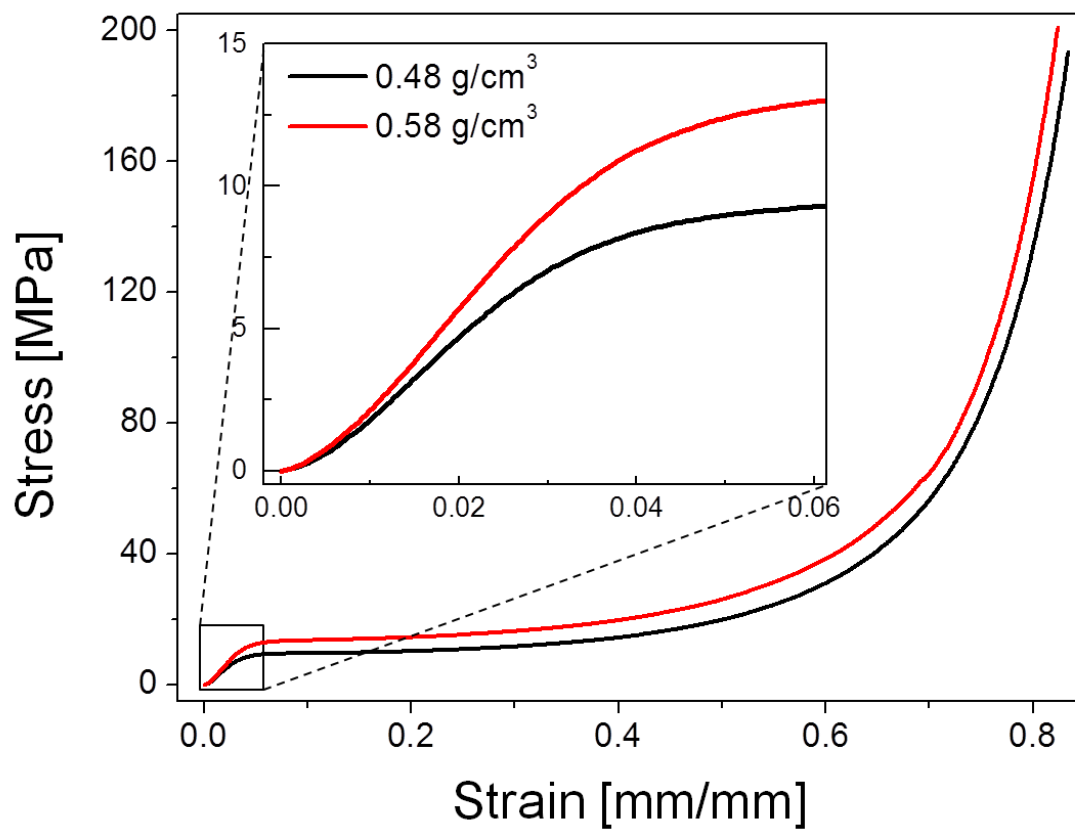


Figure S.6. Representative quasi-static compression tests of X-VO_x aerogels with different densities, as controlled by isocyanate concentration in crosslinking solutions. Elastic region expanded in inset. Protocols were followed as previously reported [17,18].

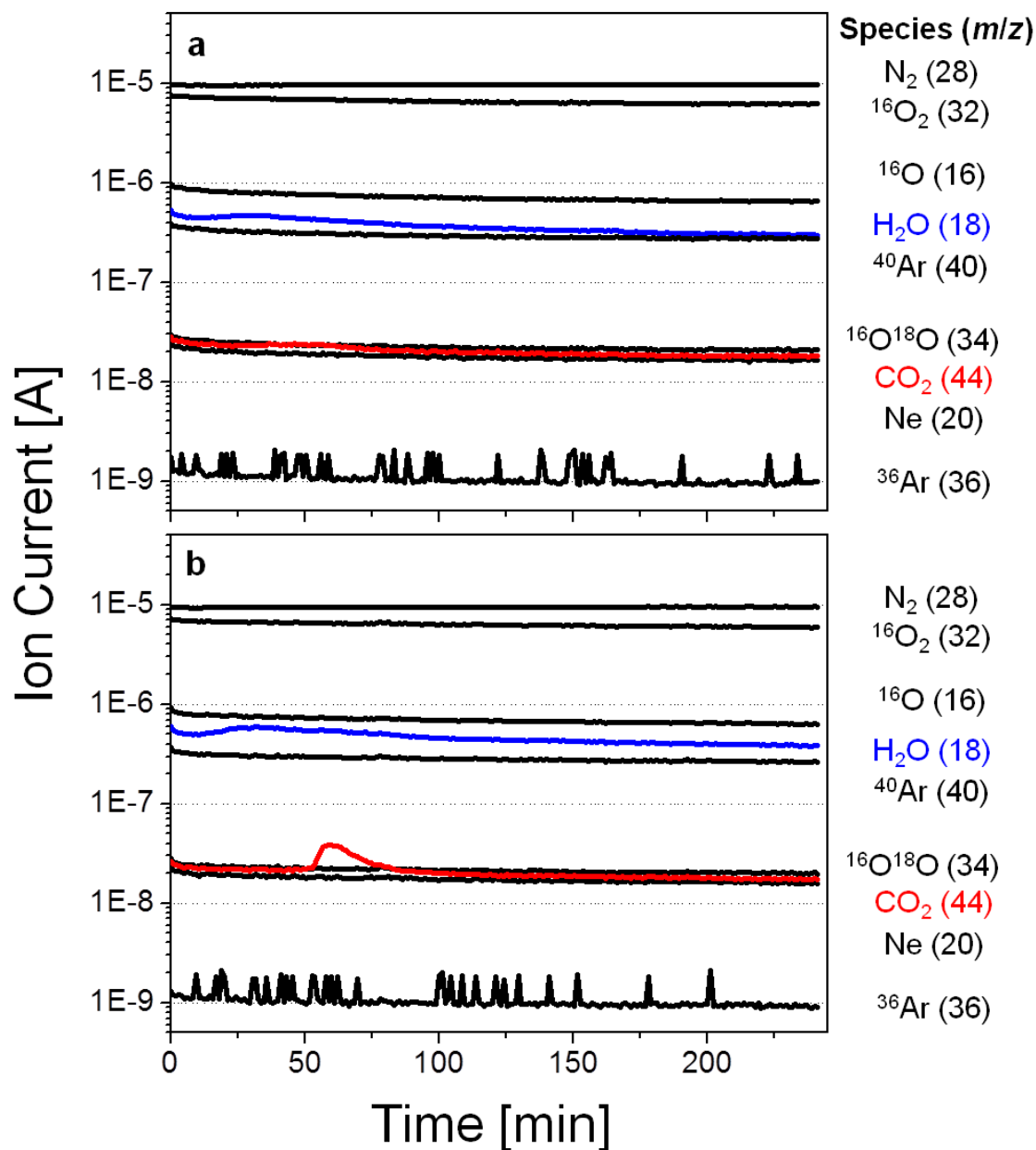


Figure S.7. MS signals between $m/z = 15$ and $m/z = 300$ above the detection limit ($\sim 10^{-10}$ A) for (a) vanadia aerogels and (b) vanadia xerogels. All identified signals are listed and identified in order of intensity at right, with isotopes labeled where more than one is observed. The ratios of the species are consistent with both typical concentrations in air and natural isotopic abundancies. For TGA-MS analysis, signals due to air were removed by subtracting the $m/z = 36$ signal multiplied by the final measured ratio between each species. Only $m/z = 18$, H_2O , (blue) and $m/z = 44$, CO_2 , (red) show a statistically significant deviation from the background. These signals were normalized by sample mass and N_2 carrier gas ($m/z = 28$) ion current, to account for variations in carrier gas flow. Latency between TGA and MS signals was determined to be 6 min by matching maxima in the mass-loss derivatives to maxima in the H_2O and CO_2 ion currents.

References:

1. Leventis N, Sotiriou-Leventis C, Mulik S, Dass A, Schnobrich J, Hobbs A, Fabrizio EF, Luo H, Churu G, Zhang Y, Lu H (2008) Polymer nanoencapsulated mesoporous vanadia with unusual ductility at cryogenic temperatures. *Journal of Materials Chemistry* 18:2475-2482.
2. Luo H, Churu G, Fabrizio EF, Schnobrich J, Hobbs A, Dass A, Mulik S, Zhang Y, Grady BP, Capecelatro A, Sotiriou-Leventis C, Lu H, Leventis N (2008) Synthesis and characterization of the physical, chemical and mechanical properties of isocyanate-crosslinked vanadia aerogels. *Journal of Sol-Gel Science and Technology* 48:113-134.

II. A study of perfluorocarboxylate ester solvents for lithium ion battery electrolytes

Tyler M. Fears^{a,b,†,*}, Robert L. Sacchi^b, Jeffrey G. Winiarz^a, Helmut Kaiser^{c,d}, Haskell Taub^{c,d}, Gabriel M. Veith^{b,*}

^a*Department of Chemistry, Missouri University of Science and Technology, 400 W. 11th St., Rolla, MO 65409, USA*

^b*Materials Science and Technology Division, Oak Ridge National Laboratory, 1 Bethel Valley Rd., Oak Ridge, TN, 37830, USA*

^c*University of Missouri Research Reactor, University of Missouri, 1513 Research Park Dr., Columbia, MO 65211, USA*

^d*Department of Physics and Astronomy, University of Missouri, Columbia, MO 65211, USA*

[†]*U.S. Department of Energy, Office of Science Graduate Student Research Program Fellow, Oak Ridge National Laboratory*

*Corresponding author

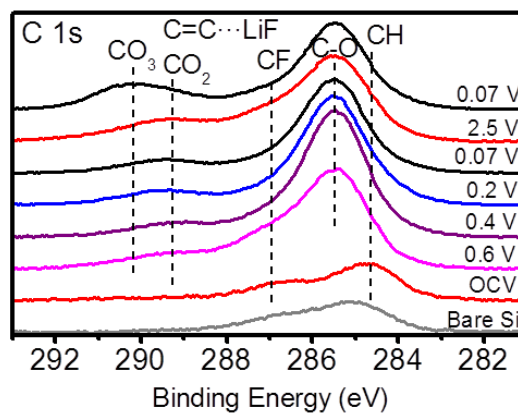
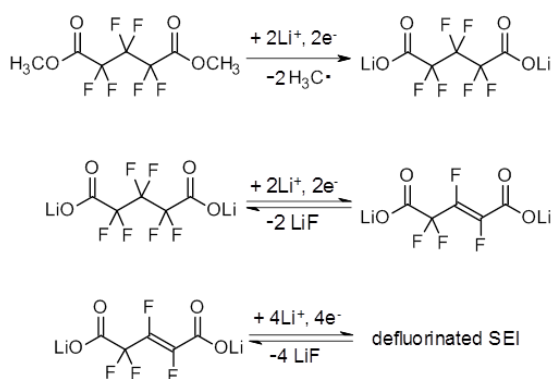
Email address: tmf9rc@mst.edu (T.M. Fears)

Email address: veithgm@ornl.gov (G.M. Veith)

ABSTRACT

Several high-purity methyl perfluorocarboxylates were prepared (>99.5% purity by mole) and investigated as potential fluorine-rich electrolyte solvents in Li-ion batteries. The most conductive electrolyte, 0.1 M lithium bis(trifluoromethanesulfonyl)imide (LiTFSI) in dimethyl perfluoroglutarate (PF5M₂) (ionic conductivity = 1.87×10^{-2} mS cm⁻¹), is investigated in Si thin-film half-cells. The solid-electrolyte-interphase (SEI) formed by the PF5M₂ electrolyte is composed of similar organic and inorganic moieties and at comparable concentrations as those formed by ethylene carbonate/dimethyl carbonate electrolytes containing LiPF₆ and LiTFSI salts. However, the SEI formed by the PF5M₂ electrolyte undergoes reversible electrochemical defluorination, contributing to the reversible capacity of the cell and compensating in part for capacity fade in the Si electrode. While far from ideal, these electrolytes provide an opportunity to further develop predictions of suitable fluorinated molecules for use in battery solvents.

GRAPHICAL ABSTRACT



HIGHLIGHTS

- Prepared fluorine-rich methyl perfluorocarboxylates electrolyte solvents.
- Perfluorinated electrolytes supported reversible Li-ion chemistry on Si electrodes.
- Perfluorinated electrolyte SEIs are similar to carbonate electrolyte SEIs.
- Reversible electrochemical defluorination mitigated Si capacity fade.

KEYWORDS: SEI, LiTFSI, silicon thin-film, fluorinated electrolyte

1. Introduction

The fluorination of organic electrolyte components typically decreases the energy (increases the molecular electrostatic potential) of both the highest occupied molecular orbital (HOMO) and lowest unoccupied molecular orbital (LUMO), shifting the usable voltage window of electrolyte components to higher potentials [1-6]. This shift increases the stability to oxidative decomposition at the cathode but decreases stability to reductive decomposition at the anode. By controlling the oxidation and reduction potentials of each species in the electrolyte, one can theoretically control which species decompose at each electrode during the initial discharge cycle and fine-tune the properties of the solid-electrolyte-interphase (SEI), which plays a vital role in extending the lifetime of Li-ion batteries [5-10].

Zhang et al. have shown that electrolytes composed entirely of fluorinated components are capable of supporting high-voltage (>5.0 V) Li-ion chemistry with minimal electrolyte degradation [1] and demonstrated that passivation issues with low-voltage anode materials can be overcome with the judicious use of fluorinated additives [2]. For example, the use of fluoroethylene carbonate (FEC) as an electrolyte additive has been shown to form a dense, robust, polymeric SEI that ameliorates fade in Si electrodes caused by fracture due to large volume changes during Li alloying and dealloying [4,10-12].

To better understand the role of fluorinated species in Li-ion battery chemistry, a series of methyl perfluorocarboxylate esters (Fig. 1) were prepared and their electrochemical performance investigated. We observe that the conductivity in these neat solvents is limited largely by Li^+ salt solubility (≤ 0.1 M). The electrochemical properties

of the most conductive electrolyte were studied using idealized Si thin-film half-cells. We observe via X-ray photoelectron spectroscopy (XPS) that the SEI formed by this perfluorocarboxylate electrolyte on a Si electrode is composed of chemical moieties, e.g., organic carbonates and LiF, similar to those formed by traditional carbonate-based electrolytes at remarkably similar concentrations. However, electrochemical defluorination, well-known in poly(tetrafluoroethylene) (PTFE) [13,14], in combination with the high reduction potential (1.0e1.5 V) of the fluorinated solvent prevents effective electrode passivation, limiting the use of such fluorine-rich species as neat electrolyte solvents in Li-ion battery cells that require extended cycling.

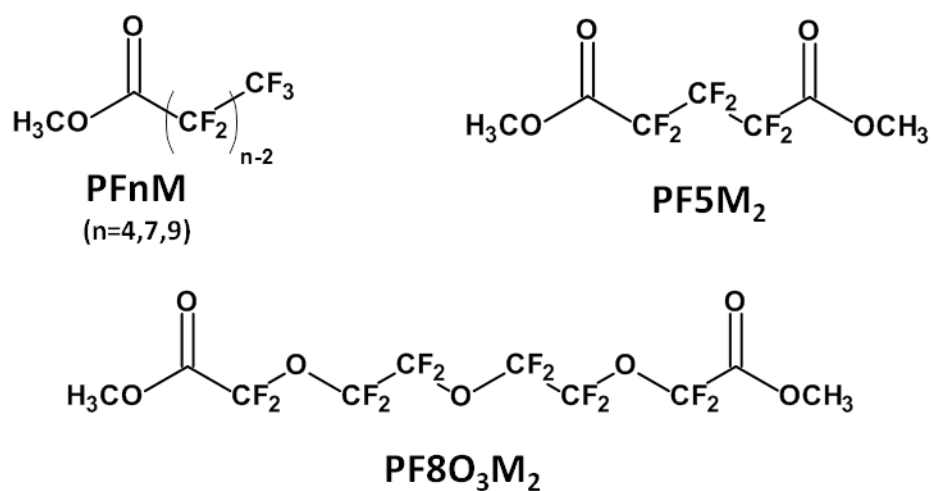


Fig. 1. Perfluorocarboxylate esters investigated in this work.

Beyond adjusting the stability window, lowering the flammability [6,15], and improving the SEI characteristics of common electrolytes, fluorinated organic compounds are also one family of solvents that can be largely hydrogen-free. This lack of H makes them prime candidates for alternative solvents in *in situ* neutron scattering

experiments, where it is desirable to minimize the background signal due to incoherent scattering from ^1H [16-24].

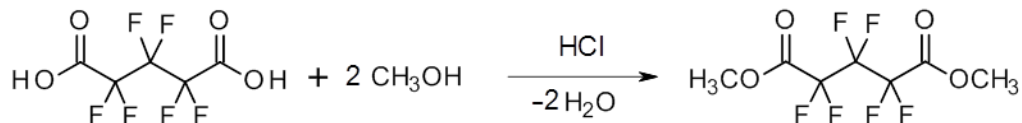
2. Materials and methods

All reagents were used as received unless otherwise noted. Those used in Li-ion battery cells were stored in a dry Ar glovebox (<5.0 ppm O_2 , <100 ppb H_2O) prior to cell fabrication.

The perfluorocarboxylates investigated here will be referenced according to the shorthand $\text{PF}_n\text{O}_x\text{Z}_y$, where n is the number of carbons on the perfluorocarboxylate, x is the number of ethereal oxygens in the perfluorocarboxylate, Z identifies the terminal group (A for carboxylic acid and M for methyl carboxylate), and y is the number of terminal groups.

2.1 Perfluorocarboxylate esterification

Perfluorobutyric acid (PF4A) (Acros, 99%), perfluoroheptanoic acid (PF7A) (Alfa Aesar, 98+%), perfluorononanoic acid (PF9A) (Alfa Aesar, 97%), perfluoroglutaric acid (PF5A₂) (Exfluor, 98%), and perfluoro-3,6,9-trioxaundane-1,11-dioic acid (PF8O3A₂) (Exfluor, 98%) were esterified with methanol (MeOH) (Sigma-Aldrich, $\geq 99.8\%$) to form the corresponding methyl esters, PF4M, PF7M, PF9M, PF5M₂, and PF8O3M₂ (Fig. 1) respectively (Scheme 1).



Scheme 1. Esterification of perfluoroglutaric acid (PF5A₂) to form dimethyl perfluoroglutarate (PF5M₂).

In a typical synthesis, 25 mmol perfluorocarboxylic acid was dissolved in 50 mmol MeOH in a 20 mL scintillation vial. HCl, prepared by passing concentrated aqueous HCl (Sigma-Aldrich, 37%) vapor through a Drierite (Sigma-Aldrich) column, was bubbled through the solution, while stirring with a PTFE stir bar, until it became turbid. This solution was then sealed and stirred overnight. After allowing the reaction mixture to settle into two phases, the lower, colorless layer was collected and transferred to a 50 mL round-bottom flask and distilled under dry N₂ (PF4M, B.P. = 80 °C; PF7M, B.P. = 140 °C) or vacuum (PF9M, B.P. = 140 °C; PF5M₂, B.P. = 120 °C; PF8O3M₂, B.P. = 160 °C) as appropriate. For dicarboxylic acid esters, 100 mmol MeOH was used.

¹H (400 MHz) nuclear magnetic resonance (NMR) and ¹³C (100 MHz) NMR with inverse-gated ¹H decoupling were performed on a Varian Unity Inova and used to verify ester synthesis. Purity was determined using the integral of the CH₃ peak in the ¹H spectrum for the ester and trace MeOH, the only detectable impurity (ester: 4.0 ppm in ¹H and 54.2 ppm in ¹³C vs. tetramethylsilane (TMS); MeOH: 3.3 ppm in ¹H and 48.6 ppm in ¹³C vs. TMS).

As-distilled esters were dried by storing over 3A molecular sieves (Alfa Aesar) in an Ar-filled glovebox for two weeks. A series of dry electrolyte salts (LiPF₆, LiClO₄,

lithium triflate, lithium bis(oxalato)borate) was investigated, and only LiTFSI (3M, Battery Grade) was found to be appreciably soluble in the synthesized esters.

2.2. *Si Thin Film Fabrication*

Si thin-film electrodes were prepared via radio-frequency (RF) magnetron sputtering using an undoped Si target (99.999%, Kurt J. Lesker) under Ar (99.9995%, Air Liquide) at 7.5 mTorr and 90 W RF power. The deposition rate was determined to be 8 nm/min using a quartz crystal microbalance (Inficon). Si was deposited for 10 min onto a rough electrochemical-grade Cu foil (Oak-Mitsui) and cut into 13-mm diameter electrodes with a kerfless punch (EL-CELL).

2.3. *Electrochemical Characterization*

Four electrolytes were evaluated in this work: 1.2 M LiPF₆ in 3:7 (by volume) ethylene carbonate/dimethyl carbonate (EC/DMC) (BASF), 0.1 M LiTFSI in 3:7 EC/DMC (Reagent Grade solvents, Aldrich, dried over 3A molecular sieves, <1 ppm H₂O), 0.1 M LiTFSI in PF5M₂, and saturated 0.1 M LiTFSI in PF8O₃M₂. Given that the PF5M₂-based electrolyte possessed the highest conductivity of the perfluorocarboxylate esters, it was exclusively used for electrochemical cycling studies.

Impedance spectroscopy was performed using a Biologic SP200 with an Accumet two-point Pt conductivity probe (#13-620-155) possessing a 1.0 cm⁻¹ cell constant in an Ar-filled glovebox. Electrolyte conductivity was obtained by fitting the impedance spectra to a typical RC circuit.

CR2023 stainless steel coin cells (Pred Materials) were prepared using Li ribbon (99.9% Alfa Aesar), porous polypropylene separators (Treopore) wetted with electrolyte, and 13-mm diameter Si thinfilm electrodes. Coin cells were galvanostatically cycled on a Maccor 4000 battery cycler at $10\ \mu\text{A}$ with voltage cutoffs 0.07 V upon lithiation and 2.5 V upon delithiation with a 10 min equilibration period between steps, corresponding to a nominal cycling rate of C/10. Rate performance was probed using galvanostatic currents of $5\ \mu\text{A}$ (C/20), $10\ \mu\text{A}$ (C/10), $20\ \mu\text{A}$ (C/5), and $50\ \mu\text{A}$ (C/2). Capacity data were normalized to the first delithiation capacity for each cell to account for slight variability in thin film thickness across the Cu foil.

2.4. Ex situ Analysis of Cycled Electrodes

After galvanostatic cycling, coin cells were transferred into an Ar-filled glovebox for decrimping. Electrodes were rinsed with 2mL DMC to remove excess electrolyte, dried under vacuum, and sectioned for *ex situ* analysis of insoluble SEI components.

Attenuated total reflectance infrared absorption (ATR-IR) spectroscopy was performed on the PF5M₂-based electrolyte as prepared and on residue collected from a separator after extensive cycling (500 cycles at C/5) without exposure to air. ATR-IR was performed on a Bio-Rad 575c with a 4 mm × 4 mm diamond ATR crystal (Golden Gate, Specac) with a reactive sample anvil and KBr beam splitter.

XPS data were collected on Si electrodes cycled in 0.1MLiTFSI in PF5M₂ electrolyte to various states of charge (SOC). Electrodes cycled in 1.2MLiPF₆ in 3:7 EC/DMC and 0.1MLiTFSI in 3:7 EC-DMC were stopped at their 7th discharge (0.07 V) for comparison. Electrodes were transferred from the glovebox to the XPS sample stage

under vacuum in a specially developed transfer chamber to prevent errant decomposition upon exposure to air. XPS data were collected on a PHI 3056 with an Al anode source operating at 15 kV and 23.3 mA. High-resolution spectra were collected using a pass energy of 5.85 eV with 0.05 eV steps. Peak fitting and quantitative elemental analysis was performed using the PHI Multipak analysis suite and standard sensitivity factors. Binding energies were referenced to the C 1s C-H peak (284.8 eV). Intensity (counts per second) was normalized to the measured total atomic composition to prevent systematic errors in signal intensity.

3. Results

3.1 Ester Physical Properties

Specific perfluorocarboxylate esters were chosen to investigate the effects of perfluorinated chain length, mono- versus dicarboxylate esters, and the effect of ethereal functional groups (Fig. 1). Despite the relatively low purity of the carboxylic acid starting reagents, ^{13}C and ^1H NMR revealed that the esterified products were highly pure: 0.5 mol% MeOH was detected in PF4M and <0.1 mol% MeOH in all other cases. This trend is explained by the fact that increasing the boiling point of an ester allows easier separation from volatile compounds; esters that were vacuum distilled above 100 °C can be held under vacuum at room temperature with no observable sample loss and contained no detectable methanol impurity. No additional impurities were detected above 0.01 mol% via ^1H or ^{13}C NMR in any sample. All distilled esters were colorless; however, the upper phase discarded during synthesis was often pale yellow. We believe that impurities

in the starting materials dissolve selectively in the MeOH/H₂O/HCl phase, resulting in high product purity without excessive processing.

LiTFSI solubility in the synthesized esters qualitatively follows the trend PF5M₂ ≥ 0.1 M >> PF8O₃M₂ ≥ PF4M > PF7M > PF9M. Solubility appears to depend primarily upon the molar density of ester functional groups (PF5M₂ = 11.1 M; PF8O₃M₂ = 6.78 M; PF4M = 6.45 M; PF7M = 4.39 M; PF9M = 3.62 M), consistent with previous reports [15]. It appears that the perfluorinated ether functionality, as in PF8O₃M₂, contributes negligibly to solubility, presumably due to the low net polarity of competing C-O and C-F dipoles. The low solubility of LiTFSI limits electrolyte conductivity (Table 1). As a result, only PF5M₂ can be utilized as a neat electrolyte solvent. While the conductivity of 0.1 M LiTFSI in PF5M₂ is inferior to both EC-DMC-based electrolytes, it is sufficient for operation at the low current densities necessary to investigate SEI formation on thin-film electrodes.

Table 1. Electrolyte conductivity as determined by impedance spectroscopy.

Electrolyte	Conductivity (mS/cm)
1.2 M LiPF ₆ in 3:7 EC/DMC	11.0
0.1 M LiTFSI in 3:7 EC/DMC	2.51
0.1 M LiTFSI in PF5M ₂	1.87×10^{-2}
Sat. LiTFSI in PF8O ₃ M ₂	5.89×10^{-4}

3.2. Galvanostatic Cycling of Si Anode Half-Cells

Fig. 2 (left) shows the normalized galvanostatic discharge (Si reduction/lithiation) and charge (Si oxidation/delithiation) curves for Si thin film half-cells as a function of electrolyte composition and cycling rate up to 25 cycles. Based on a theoretical Si capacity of 3578 mAh g^{-1} ($\text{Li}_{15}\text{Si}_4$) and a target film thickness of 80 nm, these electrodes are expected to possess a capacity of 90 mAh; however, due to electrolyte limitations and non-uniform Si deposition, due to thinning at the edges during film growth from the larger deposition distances, the capacities are highly variable. To account for these effects, the capacity was normalized to that of the first delithiation capacity, which depends only upon the total Si mass and degree of lithiation. As a result the discharge profiles are plotted with respect to 100% of the discharge capacity. The actual capacities are reported within the figures. The advantage of this approach is that we can more clearly identify changes in capacity with cycling. The corresponding differential capacity curves (Fig. 2, right) highlight the major electrochemical reactions taking place: reversible lithiation (\dagger), irreversible lithiation (\ddagger), and SEI formation (*). Lithiation steps occur at 0.25 and 0.10 V in the carbonate-based electrolytes (Fig. 2, \dagger). In the PF_5M_2 electrolyte, lithiation occurs at lower potentials, due to appreciable resistive losses. Increasing cycling rate exacerbates this potential drop. At C/5, only a single lithiation step is apparent above the 0.07 V cutoff.

All electrolytes exhibited two major irreversible reduction features at 0.5 V and 0.3 V during the first cycle (Fig. 2, \ddagger). The fact that the reduction potentials for these features are independent of the electrolyte used is evidence that these peaks are related to electrode—rather than electrolyte—chemistry. Work by Mullins et al. on partially

oxidized Si electrodes suggests that the sharp reduction feature around 0.5 V is related to the lithiation of SiO_x while the feature at 0.3 V is related to the irreversible lithiation of Si^0 [25]. The capacity corresponding to the SiO_x peak is 2.8 ± 0.2 mAh, equivalent to a 4.5 ± 0.3 nm layer of SiO_2 ($4\text{Li} + \text{SiO}_2 \rightarrow \text{Si} + 2\text{Li}_2\text{O}$, 1.59 nm μAh^{-1} for 13 mm electrodes). The fact that the capacity of this feature is independent of the bulk lithiation capacity is consistent with a surface phenomenon. Because the Cu substrate is rough, resulting in an increased surface area, this calculation overestimates the thickness of a SiO_2 film. The location of the reduction peak at 0.3 V prevents accurate integration. However, beyond asserting that these two reduction peaks are unique to the electrode and not associated with electrolyte chemistry, a detailed interpretation of these features is beyond the scope of this study.

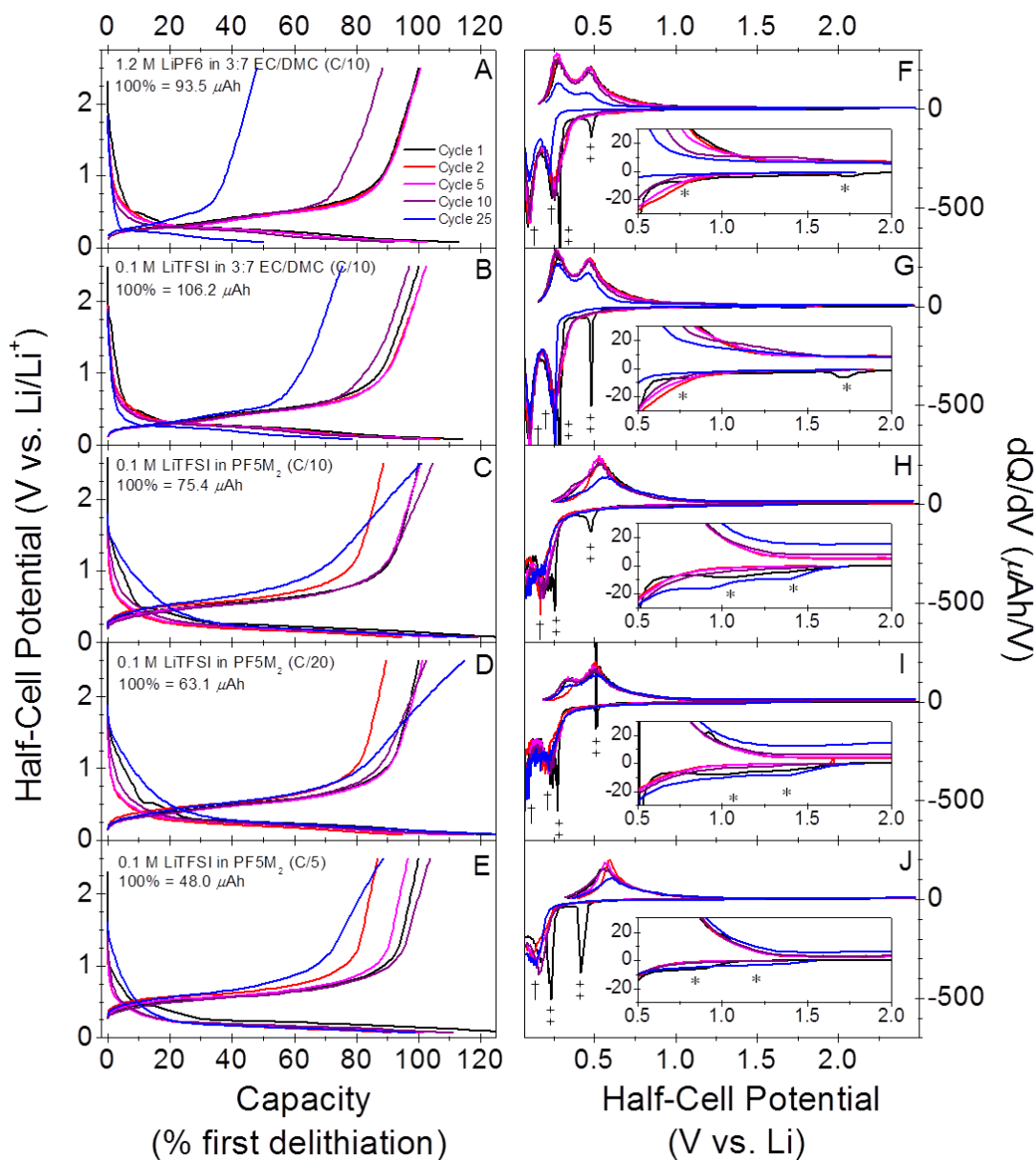


Fig. 2. Electrochemical cycling results on Si thin film electrodes. (A-E) Charge-discharge curves for investigated electrolytes at several cycling rates, normalized to initial delithiation capacity to account for fluctuations in Si thin film thickness, and (F-J) their respective differential capacity curves with an expanded inset to show SEI formation. Reduction peaks related to reversible lithiation (†), irreversible lithiation (‡), and SEI formation (*) are labeled.

SEI formation is most likely related to small irreversible peaks that can be seen in the differential capacity curve insets (Fig. 2, *). Specifically, carbonate-based electrolytes

(Fig. 2F and G) show reduction peaks at 1.75 and 0.75 V, while the PF5M₂ electrolyte (Fig. 2H,I, and 2J) shows a pair of broad peaks between 1.5 and 1.0 V. These features disappear after the first cycle, but similar features reappear around cycle 10 in the PF5M₂ electrolyte and grow steadily in intensity, suggesting that the SEI formed in this electrolyte does not effectively passivate the electrode.

The charge-discharge curves for the PF5M₂ electrolyte (Fig. 2C,D, and 2E) change in shape in later cycles. The linear region in the charge (Si delithiation) curve adopts a gentler slope, compensating in part for a decrease in the capacity of the Si lithiation peaks at 0.25 V and 0.10 V (Fig. 2H,I, and 2J), leading to a relatively stable capacity. Given that the change in the charge curve coincides with the reemergence of the SEI reduction peaks during discharge (Fig. 2H,I, and 2J, *), it is likely that these features are due to electrochemical reactions within the SEI. The fact that these changes do not occur in the carbonate electrolytes is further evidence that these changes are related to PF5M₂ and not electrode chemistry.

Si anodes cycled with the PF5M₂ electrolyte suffer a ~12% loss in capacity after the first cycle (Fig. 3A) but regain it over the next 5 cycles. The initial loss in capacity is attributed to thermodynamic changes in the lithiation potential, e.g., structural relaxation, and increased cell resistance due to SEI formation during the first few cycles. Because high resistive losses due to the low conductivity of the electrolyte place the lithiation potential very near the voltage cutoff, electrodes cycled in the PF5M₂ electrolyte are exquisitely sensitive to changes in the lithiation thermodynamics and cell resistance. The high cell resistance is illustrated by the greater voltage shift in the differential capacity curves with higher cycling rates (lower lithiation voltage and higher delithiation voltage)

(Fig. 2H,I, and 2J). At C/2 these small changes are enough to move the lithiation potential below the voltage cutoff, resulting in immediate and catastrophic capacity fade (Fig. 3A).

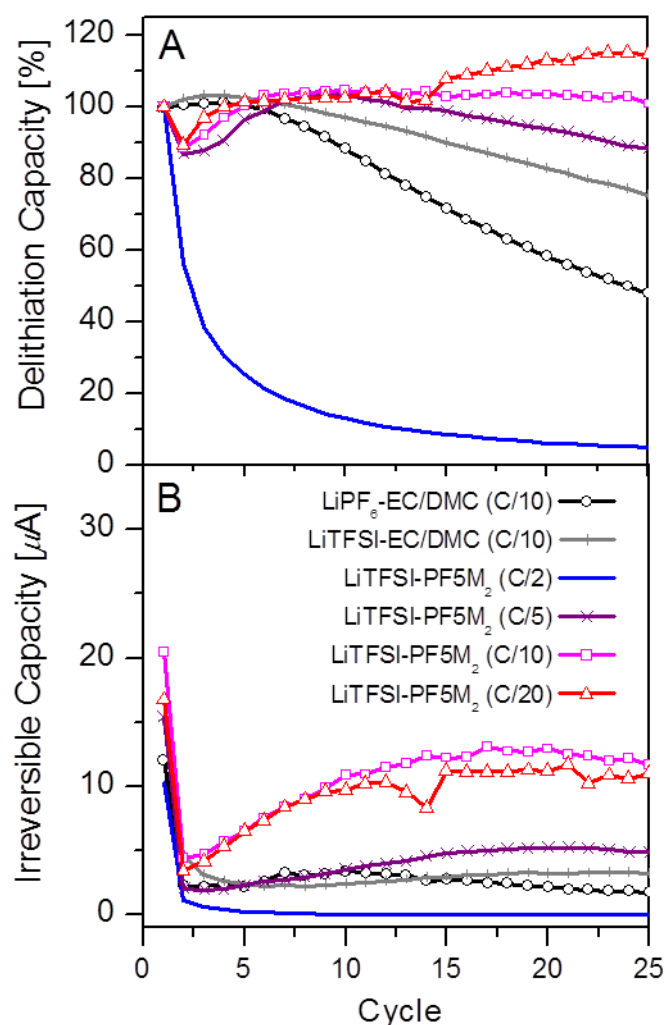


Fig. 3. Capacity fade in Si thin film electrodes: (A) normalized delithiation capacity and (B) absolute irreversible capacity (lithiation capacity - delithiation capacity). The anomalous capacity drop at cycles 13 and 14 in the PF5M₂ electrolyte (C/20) is due to a decrease in electrolyte conductivity caused by a drop in ambient temperature.

The initial drop and subsequent recovery in the delithiation capacity appears invariant when normalized to the initial delithiation capacity (Fig. 3A), implying that the reaction(s) responsible for this capacity are associated with the bulk of the Si film, consistent with silicon lithiation. By contrast, the irreversible reduction in capacity during lithiation appears invariant at low currents ($C/10$ and $C/20$) with respect to absolute current (Fig. 3B), suggesting a surface phenomenon. At high current densities ($C/2$), this irreversible loss drops to zero after only a few cycles, reflective of kinetic limitations on the reaction, consistent with electrochemical reactions taking place away from the Si electrode, i.e., electrolyte decomposition instead of Si lithiation. The observed irreversible capacity is qualitatively consistent with the magnitude of reduction peaks attributed to SEI formation (Fig. 2H,I, and J, *).

Si anodes cycled in the carbonate electrolytes do not show the early capacity loss-recovery behavior and fade much more quickly than those cycled in the PF5M₂ electrolyte (Fig. 3A). This latter effect is attributable to the higher conductivity of the carbonate electrolytes which allows for deep lithiation of the Si electrode, where extreme volume changes speed Si fracture, the primary source of capacity fade in Si electrodes [11,26,27]. The irreversible reductive capacity (Fig. 3B) of electrodes cycled in the carbonate electrolytes is relatively constant (2-3 μAh) and much less than that observed in the PF5M₂ electrolyte (>12 μAh), implying that electrochemical decomposition of the electrolyte is more significant in the PF5M₂ electrolyte.

3.3. ATR-IR of Soluble Electrolyte Decomposition Products

To investigate soluble species produced as a result of electrolyte decomposition, ATR-IR was performed on the PF5M₂ electrolyte before and after extensive cycling (Fig. 4). ATR-IR spectra show no major changes in the PF5M₂ electrolyte with extended cycling (500 cycles at C/5) except for a small feature that appears around 1700 cm⁻¹, consistent with a carbonyl stretch. This stretch is most likely due to a partially soluble lithium perfluorocarboxylate created via electrochemical de-esterification of PF5M₂ during SEI formation (Scheme 2). The lack of changes in the regions of 3000 cm⁻¹ to 3600 cm⁻¹ (COOH, OH) and 2850 cm⁻¹ to 3000 cm⁻¹ (CH) suggest that no protic or alkyl species are formed at detectable levels. Unfortunately, since the TFSI⁻ anion is undetectable due to its low concentration and interference from PF5M₂, it is unlikely that any of its decomposition products, if decomposition occurs, would be observed.

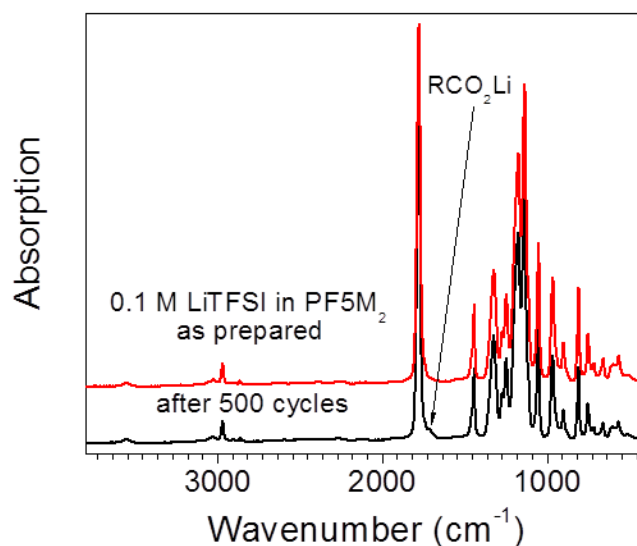
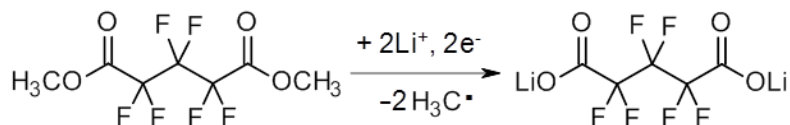


Fig. 4. IR absorption spectra of the PF5M₂ electrolyte before and after 500 cycles at C/5. All peaks are attributable to PF5M₂ in both spectra except for the small shoulder in the cycled electrolyte at 1700 cm⁻¹, attributed to the carbonyl stretch in the corresponding lithium carboxylate.



Scheme 2. Electrochemical de-esterification of PF5M₂.

3.4. XPS of SEIs Formed on Si Anodes

High resolution XPS data were collected on Si electrodes (0.07 V) after 7 lithiations with 1.2 M LiPF₆ in 3:7 EC/DMC and 0.1 M LiTFSI in 3:7 EC/DMC and compared to one lithiated twice in 0.1 M LiTFSI in PF5M₂ to investigate the effects of both electrolyte salt and solvent on SEI characteristics. Despite their significantly differing chemistries, SEIs formed from PF5M₂-based and carbonate-based electrolytes are remarkably similar (Fig. 5), containing LiF and Li₂CO₃ in addition to organic carbonates (C 1s: CO₃, 289 eV; O 1s: C=O, 532 eV, and C-O, 533 eV), carboxylates (C 1s: CO₂, 289 eV; O 1s: C=O and C-O), ethers/esters (C 1s: CO, 285.5 eV; O 1s: C-O), and fluorides (C 1s: CF, 287 eV; F 1s: CF 689 eV) in similar concentrations. The greatest compositional differences between the three electrolyte systems is the presence of the PF peak for the LiPF₆-EC/DMC electrolyte (F 1s, 688 eV) and the absence of the Li₂O peak for the PF5M₂ electrolyte (O 1s, 528 eV, and Li 1s, 54 eV).

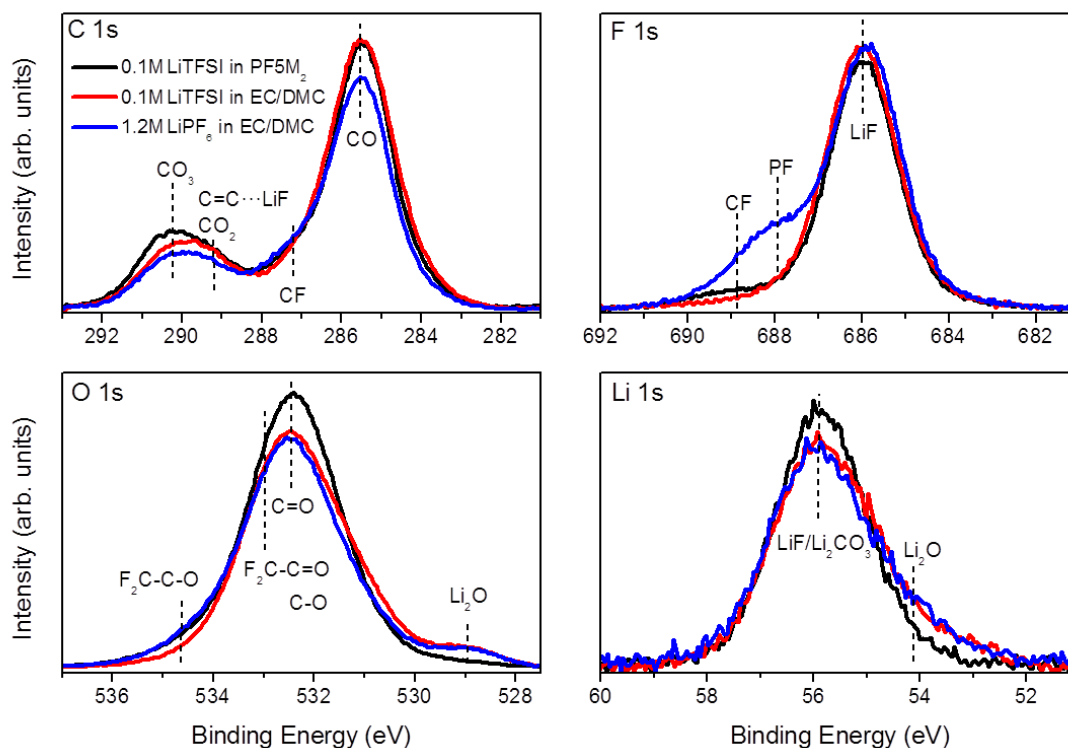


Fig. 5. High-resolution XPS of lithiated (0.07 V) Si electrodes after 7 (1.2 M LiPF_6 in EC/DMC and 0.1 M LiTFSI in EC/DMC) and 2 (0.1 M LiTFSI in EC/DMC) lithiations with nominal peak identifications.

The P 2p and N 1s spectra (not shown) indicate the presence of 1.6 at% P in the electrolyte with LiPF_6 and 0.2 at% N in the electrolytes with LiTFSI, suggesting that decomposition products of PF_6^- are a more significant (though still small) part of the SEI formed in LiPF_6 -based electrolytes when compared to those utilizing LiTFSI. However, because TFSI $^-$ is the only source of F in the 0.1 M LiTFSI in EC/DMC electrolyte, the presence of LiF at a significant concentration (10.0 at% of the SEI) implies that TFSI decomposition occurs readily, possibly with the formation of soluble S and N species.

To investigate the compositional changes of the PF5M₂ SEI during formation, XPS data (Fig. 6) were collected at several SOCs (Fig. 7). While Li₂O appears to form only in the carbonate electrolytes (Fig. 5), analysis of the SEI formed by the PF5M₂ electrolyte during the first cycle (Fig. 6) does show the formation of Li₂O. This finding is consistent with the observation that Li₂O is produced from the lithiation of SiO_x at the electrode surface [10,28]. Continued SEI growth buries this interface, reducing its intensity and making it undetectable. The fact that it is detectable in electrodes cycled with the carbonate electrolytes but not the PF5M₂ electrolyte after repeated cycling suggests that the SEI formed by the PF5M₂ electrolyte is thicker than that formed by the carbonate electrolytes, consistent with the increased and continued electrolyte decomposition observed in the PF5M₂ electrolyte during galvanostatic cycling (Fig. 2).

XPS data collected for the bare Si electrode and electrode held at open circuit voltage (OCV) vs. Li/Li⁺ for 10 min under the PF5M₂ shows only adventitious C 1s and F 1s signals, indicating no SEI is formed in the absence of a reduction current. A slight broadening and increase in the binding energy of the 103 eV peak in the Si 2p peak is consistent with the conversion of SiO₂ to SiO_{2-x}F_{2x}, suggesting that some chemical reaction does take place before SEI formation. In both cases, the peak areas indicate that 27% of the Si within the sampling depth is SiO₂/SiO_{2-x}F_{2x}. Assuming a sampling depth of 10 ± 2 nm, we estimate a SiO₂ thickness of 5.4 ± 1.1 nm, consistent with that determined from the SiO₂ lithiation capacity (Fig. 2, 0.5 V). These Si peaks can be used as a qualitative estimate for the SEI thickness (lower intensity implies a thicker SEI). Using this measure, we can see that the SEI forms above 0.6 V and continues to grow during lithiation. It then appears to shrink during delithiation and swell during lithiation. This

“breathing” phenomenon has been previously observed through similar techniques [22,23,28].

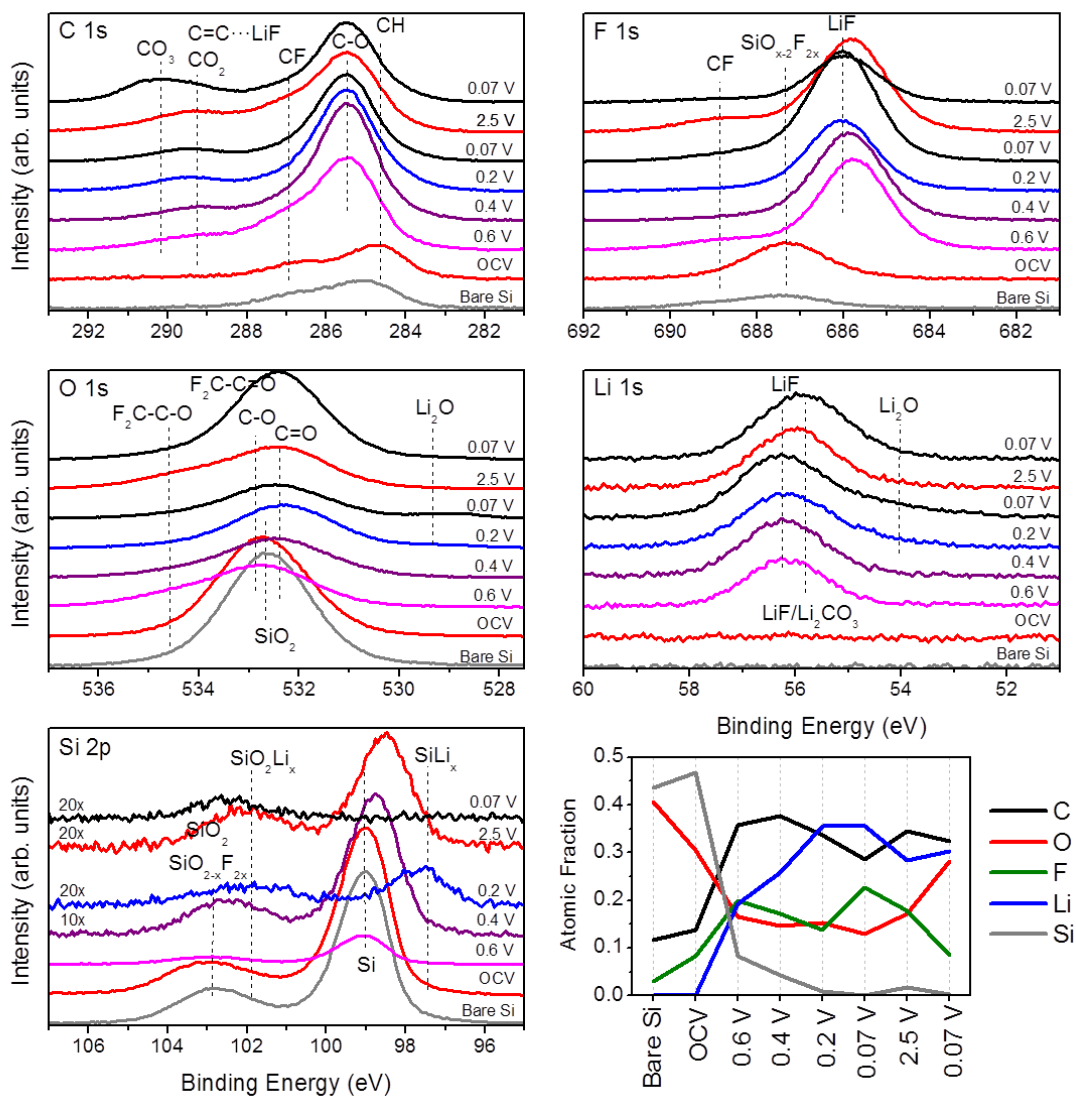


Fig. 6. High-resolution XPS and atomic fractions of Si electrodes cycled with 0.1 M LiTFSI in PF5M₂ at the various SOC_s shown in Fig. 7. A delithiation and second lithiation step was performed to determine SEI stability.

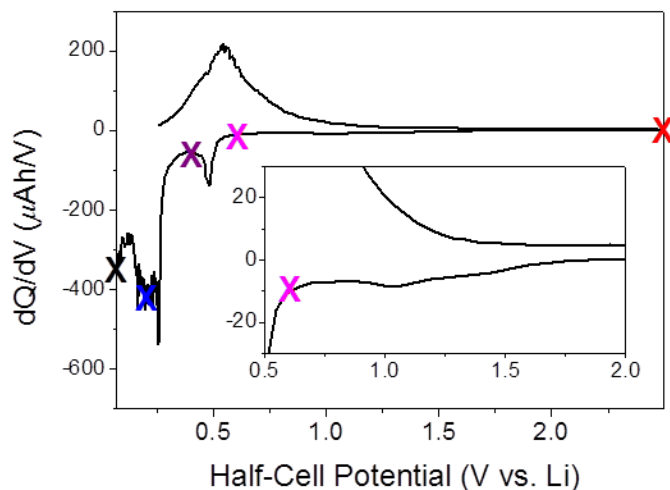
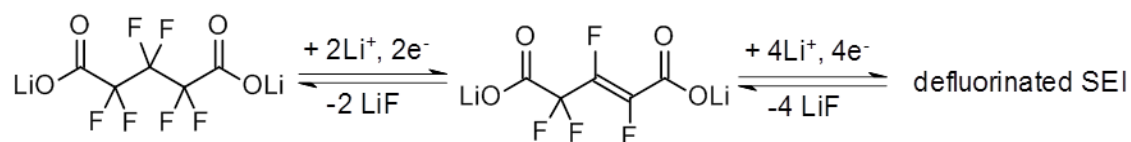


Fig. 7. Differential capacity curve with SOCs labeled for (and color-coded to match) XPS data.

XPS data show that the initial formation of the SEI in the PF5M₂ electrolyte occurred between OCV and 0.6 V upon discharge, suggesting that the small electrochemical reaction(s) around 1.5-1.0 V (Fig. 2H,I, and 2J, *) corresponds to SEI formation. This initial SEI appears to be composed primarily of fluorinated carboxylates (CO₂, CO, CF) and LiF (Fig. 6). Electrochemical defluorination of adjacent CeF bonds by Li⁺ is known to occur (C=C⁺LiF: C 1s, 289 eV), meaning that the presence of LiF (Li 1s, 56 eV, and F 1s, 686 eV) in the initial SEI could be due to either LiTFSI decomposition, shown to occur in the carbonate electrolyte, or partial electrochemical defluorination of the perfluorocarboxylate component of the SEI (Scheme 3). The pronounced CF signal (C 1s, 287 eV, and F 1s, 689 eV) disappears with additional electrochemical reduction (between 0.6 and 0.2 V), indicating that electrochemical defluorination goes to completion. Upon delithiation, these peaks reappear, meaning that either additional SEI forms during delithiation or electrochemical defluorination is

reversible. The intensity of the Si 2p peaks makes it unlikely that any significant SEI growth takes place during delithiation, the perfluorocarboxylate defluorination must be at least partially reversible.



Scheme 3. Electrochemical defluorination of lithium perfluoroglutarate.

After the second discharge, a significant change in the SEI composition took place, most dramatically seen in the atomic fractions (Fig. 6, bottom right). While the C and Li atomic fractions remained relatively unchanged, the O content increased drastically at the expense of F. No additional soluble F compounds were detected via IR, so it is unlikely that F is lost from the SEI. Instead, we find it probable that partially soluble defluorinated carboxylate and carbonate moieties segregated towards the surface of the SEI during the cycling, increasing their observed intensity via XPS. This interpretation is consistent with the formation of a CO_3 peak in the C 1s spectrum (290 eV) and the ~ 0.3 eV decrease in the binding energy (and slightly lower intensity) of the primary Li 1s peak. Such changes have been observed previously in other studies [9,28]. We are unable to explain the systematic change in the binding energy of the LiF F 1s peak, but, since the shift appears reversible (686.0 eV at 0.07 V on the first and second discharge and 685.8 eV at 0.6 V and 2.5 V), it may be related to the electrochemical defluorination reaction.

4. Discussion

While these studies investigated a number of new battery solvent molecules we found significant similarities in the atomic and functional composition of SEIs formed from carbonate-based and perfluorocarboxylate-based electrolytes. This is surprising given the significant chemical differences between the solvent molecules indicating the SEI formation reactions drive to specific low energy chemical species, e.g. LiF, Li₂CO₃ etc. These apparent similarities, though, do not prevent the systems from possessing quite different electrochemical properties, i.e., defluorination and passivation, suggesting that important subtleties in SEI composition are not captured via XPS [29]. Additionally, *ex situ* analysis only captures *insoluble* SEI components possibly missing species essential to SEI function.

The decreased capacity fade of the Si electrodes in the PF5M₂ electrolyte (110% (C/20), 100% (C/10), and 90% (C/5) compared to 75% (0.1M LiTFSI in EC/DMC, C/10) and 50% (1.2 M LiPF₆ in EC/DMC, C/10) after 25 cycles) can be partially attributed to shallower lithiation and the accompanying reduction in electrode strain [11]; however, the anomalous (yet repeatable) change in the voltage profile at later cycles partially compensates for the observed capacity losses in the lithiation and delithiation peaks. This capacity is most likely related to reversible electrochemical defluorination within the SEI. Unfortunately, we believe that these reactions increase the electronic conductivity of the SEI through the formation of an extended conjugated network, inhibiting effective passivation, as evinced by the large (>9.0 μAh/cm²) irreversible capacity and growth of SEI reduction peaks.

While this study focused on the use of perfluorocarboxylate esters as neat electrolyte solvents to reduce experimental complexity, there is no reason to limit their use to such simple systems. Additives, such as EC or fluorinated components, e.g., those investigated by Zhang et al. [1,2], which chelate Li⁺ more strongly would almost certainly improve conductivity and may improve SEI stability without sacrificing beneficial properties like nonflammability, oxidative stability, and neutron transparency.

5. Conclusion

Perfluorocarboxylate esters can be easily and inexpensively synthesized in high purity; however, as neat solvents, they do not possess the necessary conductivity to compete with more traditional electrolytes in commercial Li-ion batteries. Interestingly, the SEI formed from these electrolytes appears to undergo reversible electrochemical defluorination, contributing to the cycling capacity and compensating in part for fade due to electrode fracture and delamination. The low inherent stability of the electrolyte towards reduction, possibly combined with the electronic conductivity of an extended conjugated network formed in the SEI during electrochemical defluorination, leads to continual electrolyte decomposition. These properties may also apply to similar heavily fluorinated species proposed for next generation Li-ion electrolytes [1,2,5,30,31]. In particular the defluorination reaction, which may impart unwanted electronic conductivity in the SEI, has been shown in poly(tetrafluoroethylene) to be related to neighboring C-F bonds [13,14], an issue that can be ameliorated with careful synthetic design.

Conflicts of interest

The authors declare no conflicts of interest.

Acknowledgements

Student support and materials for ester synthesis were provided by the U.S. National Science Foundation under Grant No. DGE-1069091. Student support for the electrochemical, XPS, and ATR-IR studies performed at Oak Ridge National Laboratory provided by the U.S. Department of Energy, Office of Science, Office of Workforce Development for Teachers and Scientists, Office of Science Graduate Student Research (SCGSR) program. The SCGSR program is administered by the Oak Ridge Institute for Science and Education for the DOE under contract number DE-AC05-06OR23100. The equipment, materials and technical guidance at ORNL was supported by the Materials Sciences and Engineering Division, Office of Basic Energy Sciences, U.S. Department of Energy under contract with UT-Battelle, LLC (GMV—XPS, ATR-IR, electrochemical) and the Fluid Interface Reactions, Structures, and Transport (FIRST) Center, an Energy Frontier Research Center funded by the Office of Science, Office of Basic Energy Sciences (RLS—Conductivity, ATR-IR). T.M.F. would also like to thank Dr. C. Sotiriou-Leventis for help in formulating the perfluorocarboxylate ester synthesis.

References

- [1] Z. Zhang, L. Hu, H. Wu, W. Weng, M. Koh, P.C. Redfern, L.A. Curtiss, K. Amine, *Energy & Environmental Science*, 6 (2013) 1806.
- [2] L. Hu, Z. Xue, K. Amine, Z. Zhang, *Journal of the Electrochemical Society*, 161 (2014) A1777-A1781.
- [3] T. Böttcher, B. Duda, N. Kalinovich, O. Kazakova, M. Ponomarenko, K. Vlasov, M. Winter, G.V. Rösenthaller, *Progress in Solid State Chemistry*, 42 (2014) 202-217.
- [4] X. Chen, X. Li, D. Mei, J. Feng, M.Y. Hu, J. Hu, M. Engelhard, J. Zheng, W. Xu, J. Xiao, J. Liu, J.-G. Zhang, *ChemSusChem*, 7 (2014) 549-554.
- [5] H.Q. Pham, K.M. Nam, E.H. Hwang, Y.G. Kwon, H.M. Jung, S.W. Song, *Journal of the Electrochemical Society*, 161 (2014) A2002-A2011.
- [6] K. Xu, *Chem Rev*, 114 (2014) 11503-11618.
- [7] P. Verma, P. Maire, P. Novák, *Electrochimica Acta*, 55 (2010) 6332-6341.
- [8] K.C. Klavetter, S.M. Wood, Y.-M. Lin, J.L. Snider, N.C. Davy, A.M. Chockla, D.K. Romanovicz, B.A. Korgel, J.-W. Lee, A. Heller, C.B. Mullins, *Journal of Power Sources*, 238 (2013) 123-136.
- [9] C.K. Chan, R. Ruffo, S.S. Hong, Y. Cui, *Journal of Power Sources*, 189 (2009) 1132-1140.
- [10] B. Philippe, R. Dedryvère, M. Gorgoi, H. Rensmo, D. Gonbeau, K. Edström, *Chemistry of Materials*, 25 (2013) 394-404.
- [11] V. Chakrapani, F. Rusli, M.A. Filler, P.A. Kohl, *Journal of Power Sources*, 205 (2012) 433-438.
- [12] N. Delpuech, N. Dupré, D. Mazouzi, J. Gaubicher, P. Moreau, J.S. Bridel, D. Guyomard, B. Lestriez, *Electrochemistry Communications*, 33 (2013) 72-75.
- [13] L. Kavan, F.P. Dousek, K. Doblhofer, *Journal of Fluorine Chemistry*, 55 (1991) 37-45.
- [14] L. Kavan, F.P. Dousek, P. Janda, J. Weber, *Chemistry of Materials*, 11 (1999) 329-335.
- [15] D.H. Wong, J.L. Thelen, Y. Fu, D. Devaux, A.A. Pandya, V.S. Battaglia, N.P. Balsara, J.M. DeSimone, *Proc Natl Acad Sci U S A*, 111 (2014) 3327-3331.
- [16] I.A. Bobrikov, A.M. Balagurov, C.-W. Hu, C.-H. Lee, T.-Y. Chen, S. Deleg, D.A. Balagurov, *Journal of Power Sources*, 258 (2014) 356-364.
- [17] O. Dolotko, A. Senyshyn, M.J. Mühlbauer, K. Nikolowski, H. Ehrenberg, *Journal of Power Sources*, 255 (2014) 197-203.
- [18] T.C. Hansen, H. Kohlmann, *Zeitschrift für anorganische und allgemeine Chemie*, 640 (2014) 3044-3063.
- [19] H. Liu, C.R. Fell, K. An, L. Cai, Y.S. Meng, *Journal of Power Sources*, 240 (2013) 772-778.
- [20] M. Roberts, J.J. Biendicho, S. Hull, P. Beran, T. Gustafsson, G. Svensson, K. Edström, *Journal of Power Sources*, 226 (2013) 249-255.
- [21] J.F. Browning, L. Baggetto, K.L. Jungjohann, Y. Wang, W.E. Tenhaeff, J.K. Keum, D.L. Wood, G.M. Veith, *ACS Applied Materials & Interfaces*, 6 (2014) 18569-18576.

- [22] B. Jerliu, L. Dorrer, E. Huger, G. Borchardt, R. Steitz, U. Geckle, V. Oberst, M. Bruns, O. Schneider, H. Schmidt, *Physical Chemistry Chemical Physics*, 15 (2013) 7777-7784.
- [23] J.E. Owejan, J.P. Owejan, S.C. DeCaluwe, J.A. Dura, *Chemistry of Materials*, 24 (2012) 2133-2140.
- [24] G.M. Veith, L. Baggetto, R.L. Sacci, R.R. Unocic, W.E. Tenhaeff, J.F. Browning, *Chemical Communications*, 50 (2014) 3081-3084.
- [25] P.R. Abel, Y.-M. Lin, H. Celio, A. Heller, C.B. Mullins, *ACS Nano*, 6 (2012) 2506-2516.
- [26] C.K. Chan, H. Peng, G. Liu, K. McIlwrath, X.F. Zhang, R.A. Huggins, Y. Cui, *Nat Nanotechnol*, 3 (2008) 31-35.
- [27] Y. Oumellal, N. Delpuech, D. Mazouzi, N. Dupré, J. Gaubicher, P. Moreau, P. Soudan, B. Lestriez, D. Guyomard, *Journal of Materials Chemistry*, 21 (2011) 6201.
- [28] B. Philippe, R. Dedryvère, J. Allouche, F. Lindgren, M. Gorgoi, H. Rensmo, D. Gonbeau, K. Edström, *Chemistry of Materials*, 24 (2012) 1107-1115.
- [29] N. Leifer, M.C. Smart, G.K.S. Prakash, L. Gonzalez, L. Sanchez, K.A. Smith, P. Bhalla, C.P. Grey, S.G. Greenbaum, *Journal of The Electrochemical Society*, 158 (2011) A471.
- [30] M.L. Gordin, F. Dai, S. Chen, T. Xu, J. Song, D. Tang, N. Azimi, Z. Zhang, D. Wang, *ACS Appl Mater Interfaces*, 6 (2014) 8006-8010.
- [31] J. Kalhoff, D. Bresser, M. Bolloli, F. Alloin, J.Y. Sanchez, S. Passerini, *ChemSusChem*, 7 (2014) 2939-2946.

III. Evaluating the solid-electrolyte-interphase formed on silicon electrodes: a comparison of *ex situ* X-ray photoelectron spectroscopy and *in situ* neutron reflectometry

Tyler M. Fears^{a,b,†,*}, Mathieu Doucet^{c,*}, James F. Browning^{d,*}, Jon K. S. Baldwin^e, Jeffrey G. Winiarz^a, Helmut Kaiser^{f,g}, Haskell Taub^{f,g}, Robert L. Sacci^b, Gabriel M. Veith^{b,*}

^a*Department of Chemistry, Missouri University of Science and Technology, 400 W. 11th St., Rolla, MO 65409, USA*

^b*Materials Science and Technology Division, Oak Ridge National Laboratory, 1 Bethel Valley Rd., Oak Ridge, TN 37830, USA*

^c*Neutron Data Analysis and Visualization Division, Oak Ridge National Laboratory, 1 Bethel Valley Rd., Oak Ridge, TN 37830, USA*

^d*Chemical and Engineering Materials Division, Oak Ridge National Laboratory, 1 Bethel Valley Rd., Oak Ridge, TN 37830, USA*

^e*Materials Science and Technology Division, Los Alamos National Laboratory, Los Alamos, NM 87545, USA*

^f*University of Missouri Research Reactor, University of Missouri, 1513 Research Park Dr., Columbia, MO 65211, USA*

^g*Department of Physics and Astronomy, University of Missouri, Columbia, MO 65211, USA*

[†]*U.S. Department of Energy, Office of Science Graduate Student Research Program Fellow, Oak Ridge National Laboratory*

*Corresponding authors: tmf9rc@mst.edu (T.M. Fears), doucetm@ornl.gov (M. Doucet), browningjf@ornl.gov (J.F. Browning), veithgm@ornl.gov (G.M. Veith)

This work details experiments to characterize the liquid-solid interface of a silicon anode material *in situ* using neutron scattering characterization with perfluorocaroxylate electrolytes. The most conductive electrolyte, 0.1 M lithium bis(trifluoromethanesulfonyl)imide (LiTFSI) in deuterated dimethyl perfluoroglutarate (d_6 -PF5M₂) (1.87×10^{-2} mS/cm), was utilized for an *in situ* neutron reflectometry (NR) study of the solid-electrolyte-interphase (SEI) formation on a Si electrode. SEI composition and thickness determined via *in situ* NR and *ex situ* X-ray photoelectron spectroscopy (XPS) was compared. SEI expansion and contraction (breathing) during electrochemical cycling was observed via both techniques; however, *ex situ* XPS suggests

that the SEI thickness increases during Si lithiation and decreases during delithiation, while *in situ* NR suggests the opposite. It is shown that the most likely cause of this discrepancy is the selective removal of SEI components during electrode rinse, required to remove electrolyte residue prior to *ex situ* analysis, demonstrating the necessity of performing SEI characterizations *in situ*.

1. Introduction

Solid-electrolyte-interphases (SEIs) formed by electrolyte decomposition on electrode surfaces during electrochemical cycling are an integral, yet under-characterized component of Li-ion batteries. SEIs impede performance by reducing Li^+ conductivity but also increase the useful lifetime of the cell by preventing continual decomposition of the electrolyte and inhibiting electrode decomposition and exfoliation. Finding a balance between these properties is necessary for the optimization of battery performance and requires a detailed study of the relationship between SEI composition and properties. The SEI is typically a 5-50 nm layer on 1-100 μm particles, so the SEI is only a low compositional fraction and must be analyzed with surface-sensitive techniques or grown on high-surface-area materials to obtain sufficient signal intensity.¹⁻⁸ The most common methods of characterizing SEIs, e.g., X-ray photoelectron spectroscopy (XPS), infrared absorption spectroscopy (IR), nuclear magnetic resonance spectroscopy (NMR), involve disassembling cycled Li-ion cells and often rinsing the electrode of interest to remove excess electrolyte before analysis.⁶⁻⁹ These preparation steps potentially remove soluble SEI components and expose the electrode to environmental contaminants. *In situ* characterization avoids such effects and has the potential to monitor transient and dynamic interactions.

Several methods exist for studying battery materials and interfaces *in situ*.⁹⁻¹⁹ For this study, neutron reflectometry (NR) was chosen to investigate the SEI formed on a Si thin film, as it possesses several advantages over other methods. X-ray and neutron reflectometry are interface-sensitive techniques,^{8, 20-25} unlike diffraction or nuclear magnetic resonance, and interrogate a macroscopic sample size, unlike electron microscopy. Neutrons are deeply penetrating and sensitive to light elements (H, Li),^{10, 15, 17, 24-27} unlike X-rays, making NR particularly suited for the characterization of SEIs and electrodes in Li-ion batteries.^{10, 15, 17, 24-27} A specialized cell has been developed at the Oak Ridge National Laboratory for use on the Liquids Reflectometer (Spallation Neutron Source, Beam Line 4B) for performing NR on thin films with electrochemical cycling. This set-up can obtain high quality data in a reasonable amount of time (<1 hr per measurement) and minimizes model uncertainty by limiting the number of fitting parameters.²³⁻²⁵

Hydrogen, ¹H, possesses a large, incoherent neutron scattering cross-section, so the presence of hydrogenous material in an electrochemical cell can contribute significantly to the background signal in elastic neutron scattering techniques like NR. For neutron scattering experiments with *in situ* electrochemistry, this unwanted scattering typically comes from the requisite organic electrolyte solvent, e.g., dimethyl carbonate (DMC), ethylene carbonate (EC), propylene carbonate (PC). Because neutron scattering is derived from nuclear interactions, isotopic substitution (deuteration, ²H) is typically utilized to minimize unwanted scattering from hydrogenous components.^{15-18, 20, 21, 23-25, 27, 28} Unfortunately, deuterated carbonate esters are both expensive and of only moderate (~99%) purity, making viable alternatives desirable.²⁹

An ideal electrolyte for *in situ* neutron scattering studies would possess a high ionic conductivity, high purity (commercially available ^1H EC, DMC, PC electrolytes), and a low (incoherent) scattering cross-section (commercially available ^2H EC, DMC, PC). It is also necessary that the electrolyte have an appropriate electrochemical stability window, which is experiment-dependent. In order to aid NR data it is necessary to maximize the scattering length density (SLD) contrast between layers (discussed in Sect. 2.5), which warrants the use of an electrolyte with a high SLD for the experimental geometry used here. Other *in situ* neutron scattering techniques, e.g., neutron diffraction, benefit from minimizing both the electrolyte SLD and incoherent neutron scattering cross-section.^{10, 15-19}

Fluorinated solvents have a number of advantageous properties for Li-ion battery electrolytes: high oxidation potential, low flammability, and attractive SEI characteristics.^{1, 5, 8, 30-32} Perfluorinated organic solvents are also one family of materials that are both electrochemically stable and hydrogen-free, suggesting that they may be prime candidates for solvents in *in situ* neutron scattering experiments. To investigate this potential, d_3 -methyl perfluorocarboxylates were synthesized with high ($\geq 99.9\%$) purity and used as low-scattering electrolyte solvents for *in situ* NR. Perfluorocarboxylate esters were chosen due to the known ability of esters to solvate Li ions⁸ and the ability to easily and inexpensively synthesize deuterated esters using the corresponding carboxylic acids and deuterated methanol (d_3 -MeOD). The specific methyl perfluorocarboxylates used in this study (Fig. 1) were chosen such that they covered a reasonable range of $-\text{CF}_2-$ chain lengths, diesters, and perfluoroethers. The electrochemical properties of these electrolytes have been previously reported along with an in-depth *ex situ* chemical characterization of

the SEI formed on Si electrodes via *ex situ* XPS.³³ This study focuses on those properties specifically relevant to their use as electrolyte solvents in *in situ* neutron scattering experiments and a comparison with *ex situ* characterization. Using these electrolyte solvents instead of commercially-available deuterated carbonates improves both the observed electrochemistry, due to high purity, and the quality of NR data, due to their exceedingly low neutron scattering cross-sections. The relationship between the state-of-charge (SOC) of the Si electrode and the SEI composition and thickness differs when analyzed via *ex situ* XPS and *in situ* NR, demonstrating the importance of *in situ* characterization.

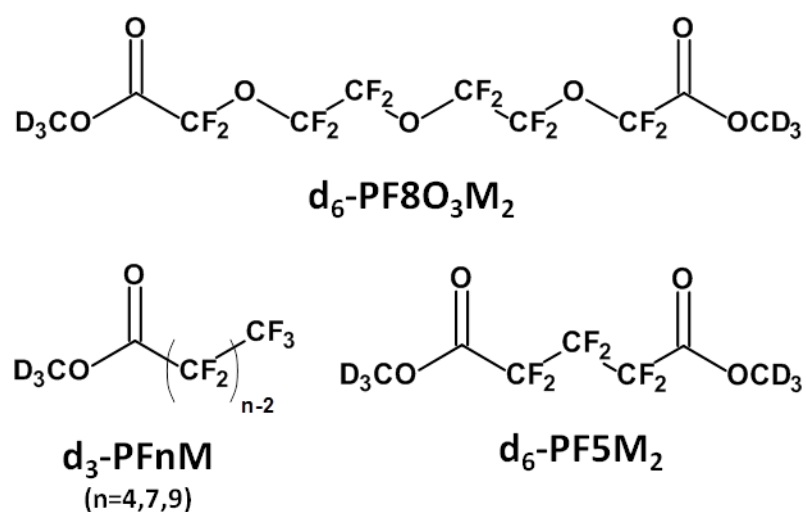


Fig. 1 d₃-methyl perfluorocarboxylate esters investigated as electrolyte solvents in this study.

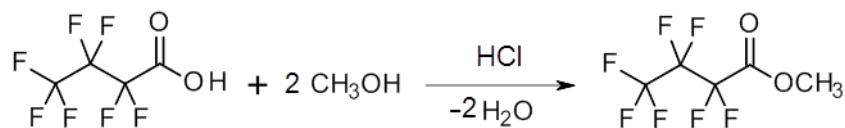
2. Materials and methods

All reagents were used as received unless otherwise noted. Those used in Li-ion battery cells were stored in a dry Ar-filled glovebox (<5.0 ppm O₂, <100 ppb H₂O) prior to cell fabrication.

The perfluorocarboxylates investigated here will be referenced according to the shorthand $\text{PF}_n\text{O}_x\text{Z}_y$, where n is the number of carbons on the perfluorocarboxylate, x is the number of ethereal oxygens in the perfluorocarboxylate, Z identifies the terminal group (A for carboxylic acid and M for methyl carboxylate ester), and y is the number of terminal groups.

2.1. Perfluorocarboxylic acid esterification

Perfluorobutyric acid (PF4A) (Acros, 99%), perfluoroheptanoic acid (PF7A) (Alfa Aesar, 98+%), perfluorononanoic acid (PF9A) (Alfa Aesar, 97%), perfluoroglutaric acid (PF5A₂) (Exfluor, 98%), and perfluoro-3,6,9-trioxaundane-1,11-dioic acid (PF8O₃A₂) (Exfluor, 98%) were esterified with methanol (MeOH) (Sigma-Aldrich, $\geq 99.8\%$) to form the corresponding methyl esters, PF4M, PF7M, PF9M, PF5M₂, and PF8O₃M₂ (Fig. 1) respectively (Scheme 1).



Scheme 1 Esterification of perfluorobutyric acid (PF4A) to form methyl perfluorobutyrate (PF4M).

In a typical synthesis, 25 mmol perfluorocarboxylic acid was dissolved in 50 mmol MeOH in a 20 mL scintillation vial. HCl, prepared by passing concentrated aqueous HCl (Sigma-Aldrich, 37%) vapor through a Drierite (Sigma-Aldrich) column, was bubbled through the solution, while stirring with a PTFE stir bar, until it became

turbid. This solution was then sealed and stirred overnight. After allowing the reaction mixture to settle into two phases, the lower, colorless layer was collected and transferred to a 50 mL round-bottom flask and distilled under dry N₂ (PF4M, boiling point = 80° C; PF7M, 140° C) or vacuum (PF9M, 140° C; PF5M₂, 120° C; PF8O3M₂, 160° C) as appropriate. For dicarboxylic acid esters, 100 mmol MeOH was used. For the synthesis of deuterated esters, e.g., d₃-PF4M, d₆-PF5M₂, MeOH was replaced with its perdeuterated counterpart, d₃-MeOD (99.8 %D, Fisher Scientific).

¹H (400 MHz) nuclear magnetic resonance (NMR) and ¹³C (100 MHz) NMR with inverse-gated ¹H decoupling were performed on a Varian Unity Inova and used to verify ester synthesis. Purity was determined using the integral of the CH₃ peak in the ¹H spectrum for the ester and trace MeOH, the only detectable impurity (ester: 4.0 ppm in ¹H and 54.2 ppm in ¹³C vs. tetramethylsilane (TMS); MeOH: 3.3 ppm and 3.6 ppm in ¹H and 48.6 ppm in ¹³C vs. TMS).

As-distilled esters were dried by storing over 3A molecular sieves (Alfa Aesar) in an Ar-filled glovebox for two weeks. Due to its high relative ionic conductivity in comparison to other perfluorocarboxylate-based electrolytes (1.87×10^{-2} mS/cm), 0.1 M lithium bis(trifluoromethane-sulfonyl)imide (LiTFSI) (3M, Battery Grade) in d₆-PF5M₂ was used as the electrolyte for all electrochemical characterizations.

2.2. Neutron Scattering Profiles

The total scattering coefficient (τ) of a series of protiated and deuterated electrolyte solvents was calculated using standard thermal neutron scattering cross-sections³⁴ and solvent densities:

$$\tau = \sum_i N_{d,i}(\sigma_{T,i}) = N_A M_d \sum_i n_i(\sigma_{COH,i} + \sigma_{INC,i}) \quad (1)$$

where $N_{d,i}$ is the number density of nucleus i , $\sigma_{T,i}$ is the sum of the coherent ($\sigma_{COH,i}$) and incoherent ($\sigma_{INC,i}$) neutron scattering cross-section of nucleus i , N_A is Avagadro's number, M_d is the molar density of the solvent, and n_i is the number of nucleus i in the molecular formula for the solvent. Scattering profiles were collected from several electrolyte solvents in order to compare with the calculated values and demonstrate the contribution of both incoherent (flat) and coherent (diffuse peaks) scattering to the total background signal.

Energy-integrated neutron scattering profiles were collected on the University of Missouri Research Reactor (MURR) triple-axis spectrometer (TRIAX) using a 6-mm-diameter Al sample can. The incident wavelength was fixed at 2.36 Å (14.7 meV). Scattered neutrons were monitored from $2\theta = 44.0^\circ$ ($Q = 1.99 \text{ \AA}^{-1}$) to $2\theta = 82.2^\circ$ (3.50 \AA^{-1}) at a step-size of 0.1° for 1×10^6 monitor counts (~ 2 min) per point.

2.3. Fabrication of electrochemical cell for in situ NR

The thin-film working electrode was deposited by DC magnetron sputtering and evaporation from commercially available targets, Cu (99.99% - Kurt J. Lesker) and Si (99.99% - Kurt J. Lesker) in an in-house sputtering system. Base pressures were below 5×10^{-8} Torr before Cu sputter deposition and the target to substrate distances were 5 cm. Rates were measured using a quartz crystal microbalance. The Cu films were deposited by DC sputtering at an applied power of 300 W, at 3 mTorr Ar (99.9995%, Air Liquide) for 2 min. The amorphous Si films were deposited by thermal evaporation in a chamber

with a base pressure less than 5×10^{-9} Torr. The samples were not exposed to air between depositions. 50-mm-diameter, 10-mm-thick single-crystal Si substrates were obtained from the Institute of Electronic Materials Technology, Warszawa, Poland.

Ti_{0.68}Zr_{0.32} alloy (subsequently referred to as TiZr) was selected as the Li current collector for two reasons: (1) TiZr is a null (SLD = 0, incoherent) scatterer of neutrons, eliminating the possibility of interfering diffraction peaks in the NR pattern, and (2) TiZr does not react chemically or electrochemically with Li. A machined 50-mm-diameter, 1-cm-thick TiZr substrate was cleaned in successive water and isopropanol sonication baths and dried at 120 °C for 2 days. The Li counter electrode (2.9 cm) was prepared using $3/4$ "-wide Li-foil (Alfa Aesar), which was scraped clean and pressed onto the TiZr substrate in a dry Ar-filled glovebox.

Wires were attached to the Si and TiZr plates (prior to Li deposition) using silver epoxy (Illinois Tool Works) which was allowed to dry overnight. The silver epoxy was placed on the edge of the Si wafer to contact the Cu which was spilled around the wafer during deposition. The epoxy was never in contact with the electrolyte. Electrodes and 0.1 M LiTFSI in d₆-PF5M₂ electrolyte were sealed under dry Ar and transferred to a He-filled glovebox (H₂O < 1 ppm; O₂ < 7 ppm) located at the beam line for on-site cell assembly.

The *in situ* electrochemical cell for NR was assembled using a specially-developed apparatus as previously reported.²³⁻²⁵ The electrodes were separated by a 48-mm-diameter Teflon-coated Viton O-ring with a 0.8 mm cross-sectional diameter. The total cell volume was ~2.5 mL, depending on the amount of Li on the TiZr. This volume was filled with the 0.1 M LiTFSI in d₆-PF5M₂ electrolyte using ports in the TiZr current

collector, which were subsequently sealed with Teflon plugs. A diagram of the assembled cell and NR geometry is shown in Fig. 2.

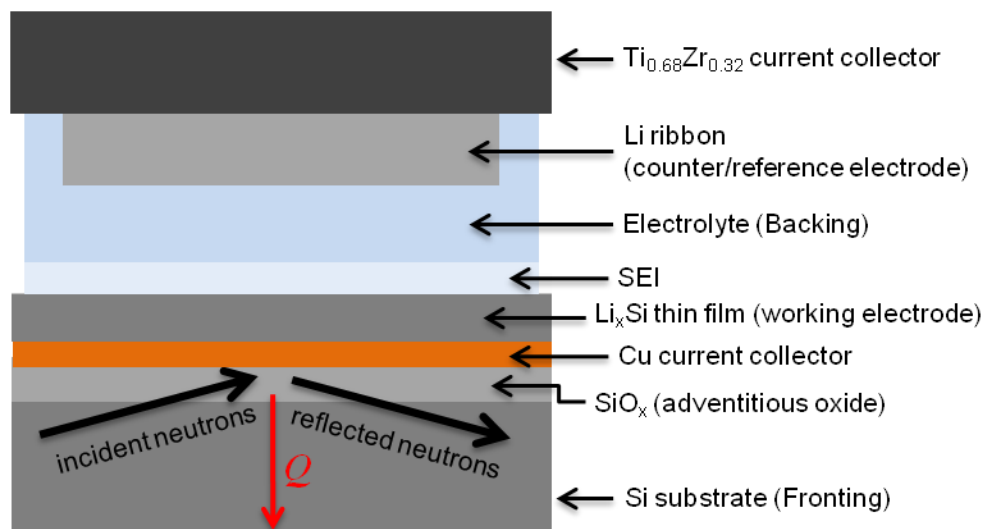


Fig. 2 Experimental geometry for collecting NR data.

2.4. In situ *electrochemistry and NR*

Electrochemistry was controlled using a Biologic VSP potentiostat. Due to the high resistance of the *in situ* cell, galvanostatic cycling was not possible, so the cell was cycled using a hybrid galvanostatic-potentiostatic protocol. Electrodes were driven galvanostatically ($375 \mu\text{A}$) to the desired potential and held potentiostatically for 30 min. The cell was then allowed to equilibrate in the open-circuit state for 30 min prior to NR data collection. Voltages are reported with respect to the Li metal counter electrode (Li/Li^+).

NR measurements were carried out on the Liquids Reflectometer (LR, Beam Line 4B) at the Spallation Neutron Source (SNS) at Oak Ridge National Laboratory. The LR is

a horizontal-geometry instrument using the time-of-flight technique with an effective single bandwidth of 3.5 Å at an accelerator pulse frequency of 60 Hz. NR measurements on the assembled cell were carried out in the inverted geometry, using the Si substrate as the incident medium, in order to observe a critical edge. NR was performed on the as-fabricated electrode in the traditional geometry, with air as the incident medium, in order to determine the initial multilayer parameters prior to any chemical interaction with the electrolyte. For these measurements, neutrons of wavelengths 2.5 Å to 17 Å together with four angles of incidence, $\theta = 0.60^\circ$, 0.69° , 1.37° , and 2.71° , provided a wave vector transfer (Q) range extending from 0.008 \AA^{-1} to 0.22 \AA^{-1} . An incident beam slit was adjusted for each angle in order to maintain a constant footprint on the sample.

Reflected neutrons are collected in a two-dimensional detector array oriented perpendicular to the specularly reflected beam. Each neutron detection event is recorded with detector pixel ID and time-of-flight (TOF) from the spallation event. This data is processed with the Mantid data analysis framework to obtain the reflectivity profile.³⁵ Using the reflection angle and neutron TOF, the data is converted to intensity as function of Q . The background intensity is determined from the off-specular intensity and subtracted from the specular intensity (Electronic Supplementary Material Fig. S1). The final reflectivity is obtained by absolutely normalizing the resulting intensity using attenuation parameters experimentally-determined from an uncoated single-crystal Si substrate.

2.5. Fitting of NR data

Modeling of the neutron reflectivity data was done using the Motofit program.²⁶ Details of the analysis, including the estimation of the uncertainties can be found in reference.²⁵ Model constraints were added to analysis described in the reference stated above. Using the well-defined relationship between Li_xSi alloy stoichiometry and cell volume,³⁶

$$\frac{V}{V_0} = 1 + 0.775x \quad (2)$$

and assuming one-dimensional swelling typical of thin films, the thickness and SLD of the Li_xSi layer were constrained to a single fitting parameter. Ultimately fitting of NR results in a thickness and SLD (β) for each layer. SLD is indicative of the atomic composition of the layer and can be calculated using Eq. 3:

$$\beta = \sum_i N_{d,i} b_i = N_d \sum_i \chi_i b_i \quad (3)$$

where $N_{d,i}$ is the number density of nucleus i , b_i is the neutron scattering length of nucleus i , N_d is the average atomic number density of the layer, and χ_i is the molar fraction of nucleus i .

2.6. Ex situ characterization

Si thin-film witness electrodes were prepared via radio-frequency (RF) magnetron sputtering using an undoped Si target under Ar at 7.5 mTorr and 90 W RF power. The

deposition rate was determined to be 8 nm/min using a quartz crystal microbalance (Inficon). Si was deposited for 10 min onto a rough electrochemical-grade Cu foil (Oak-Mitsui). The Si films were then cut into either 13-mm- or 8-mm-diameter electrodes as necessary.

The effect of cycling on electrolyte composition was investigated via *ex situ* NMR. Cycled electrolytes were prepared by galvanostatically (10 μ A) discharging electrolytes for 18 hr in a two-electrode Swagelok-type cells with an 8-mm Si thin-film working electrode and Li counter electrode and \sim 1 mL protiated or deuterated 0.1 M TFSI electrolyte. Two layers of a 0.14-mm-thick PEEK mesh (McMaster Carr) were used as a separator in order to ensure a large electrolyte volume for analysis. Swagelok cells were disassembled in a dry Ar glovebox and \sim 0.75 mL of each cycled and uncycled electrolyte was transferred to a 5-mm NMR tube. The tubes were then sealed with a polypropylene cap followed by placing a thin bead of epoxy (Loctite Hysol 1C) on the lip of the polypropylene cap for air-tightness before removing from the glovebox. ^1H (400 MHz), ^{13}C (101 MHz) with inverse-gated ^1H decoupling, ^{19}F (376 MHz), and ^7Li (155 MHz) NMR on a Bruker Avance III spectrometer. ^1H spectra were referenced to the most intense impurity signal (1.35 ppm vs. TMS). ^{13}C and ^{19}F spectra were referenced to the most intense CF_2 peak (109.43 ppm vs. TMS and -119.60 ppm vs. CFCl_3 , respectively). These secondary references were chosen in order to avoid isotopically-induced shifts from deuteration on the CH_3 signal (0.04 ppm in ^1H and 0.70 ppm in ^{13}C). Due to the absence of an accurate (<0.01 ppm) secondary standard, ^7Li peaks were set to 0 ppm and are only used to demonstrate changes in peak width and intensity with cycling.

The atomic composition of the SEI formed on Si thin-film electrodes was characterized as a function of SOC via *ex situ* XPS. CR2023 stainless steel coin cells (Pred Materials) were prepared using Li ribbon, porous polypropylene separators (Treopore) wetted with electrolyte, and 13-mm Si thin-film electrodes. Coin cells were galvanostatically cycled at 10 μ A, corresponding to an approximate cycling rate of C/10 (fully discharged in 10 h), on a Maccor 4000 battery cycler and stopped at specific potentials related to observed electrochemical reactions. Cycled coin cells were then transferred into a dry Ar-filled glovebox for decrimping. Electrodes were rinsed with 2 mL DMC (Aldrich, 99.9%) to remove excess electrolyte, dried under vacuum, and sectioned for *ex situ* analysis of insoluble SEI components. Electrodes were transferred from the glovebox to the XPS sample stage under vacuum in a specially developed transfer chamber to prevent decomposition upon exposure to air. XPS data were collected on a PHI 3056 with an Al anode source operating at 15 kV and 23.3 mA. High-resolution spectra were collected using a pass energy of 5.85 eV with 0.05 eV steps. Peak fitting and quantitative elemental analysis was performed using the PHI Multipak analysis suite and standard sensitivity factors. Binding energies were referenced to the C 1s C-H peak (284.8 eV).

3. Results

3.1. Ester physical properties

The synthesis and conductivity of these electrolytes has been described previously.³³ In this prior work we demonstrated that despite the relatively low purity of the carboxylic acid starting reagents, ¹³C and ¹H NMR revealed that the esterified

products were of high purity (>99.7 mole %). The most common impurity was methanol which could easily be removed by distillation especially for the esters with higher boiling points, which can be held under vacuum at room temperature for extended periods with negligible sample loss. In order to confirm the predicted coherent and incoherent scattering components, Fig. 3A, from the electrolyte energy-integrated, elastic plus inelastic, neutron scattering profiles were measured, Fig. 3B, on the solvents without salt species. Using the calculated thermal neutron scattering coefficients, τ (summarized in Fig. 3A), the fraction of unscattered neutrons passing through a medium can be estimated from the Beer-Lambert law (Eq. 4):

$$\frac{I(l)}{I_0} = e^{-\tau l} \quad (4)$$

where $I(l)$ is the intensity of the neutron beam after passing a distance l through the scattering medium and I_0 is the initial intensity of the neutron beam. Since the scattered neutrons only add to the background intensity during a measurement, it is ideal to minimize this contribution. For example, a 5-mm path through protiated DMC would scatter 80% of neutrons while deuterated DMC would only scatter 5.5% of the neutrons. Passing neutrons through protiated and deuterated PF5M₂ results in 56% and 2.8% of neutrons scattering, respectively. Fig. 3B shows the measured neutron scattering profiles of several standard and prepared deuterated and protiated solvents. The two large peaks at 2.7 and 3.1 Å⁻¹ are due to the polycrystalline Al in the sample can whose intensities vary depending on tube orientation relative to the beam. The data for the solvents is reflected in the apparent baseline of the spectra. As expected the protiated DMC has a very high

intensity due to the large concentration of protons. A second group of spectra collected for the protiated esters show that their cross-sections are much lower than the DMC consistent with lower neutron scattering densities as estimated in Figure 3A. Finally, the third bunch of spectra collected for the deuterated esters are universally low, which is consistent with theoretical calculations.³⁴ While the greatest reduction in background is achieved through deuteration, d_6 -PF5M₂ is expected to contribute only about half as much to the background intensity as d_6 -DMC which would result in a significant reduction in background intensity.

After rigorous drying with 3A molecular sieves in a dry Ar glovebox, only PF5M₂ was able to dissolve LiTFSI up to 0.1 M. While the conductivity of 0.1 M LiTFSI in PF5M₂ (1.9×10^{-2} mS/cm) is inferior to carbonate-based electrolytes, e.g., 1.2 M LiPF₆ in 3:7 EC-DMC (11 mS/cm), it is sufficient for low to moderate discharge rates.³³

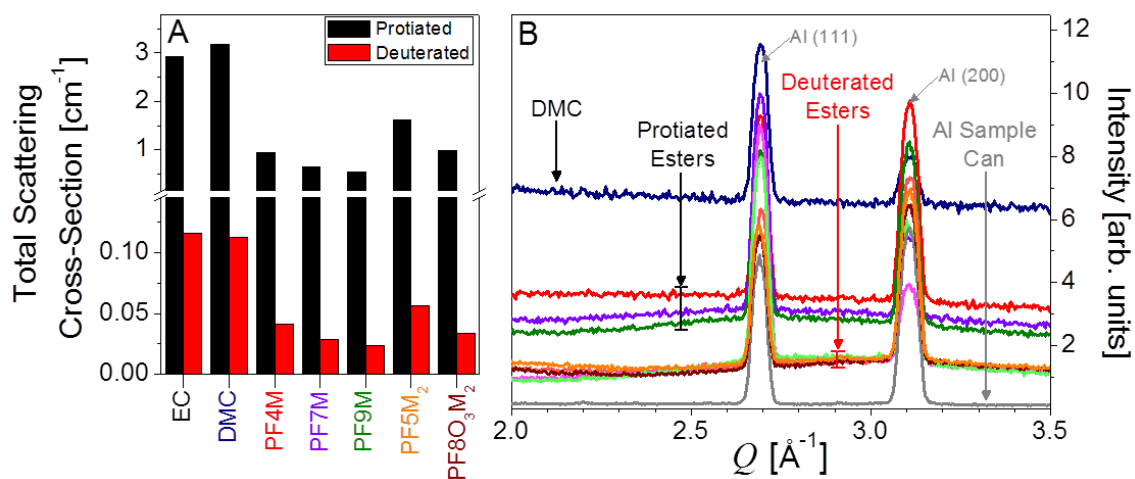


Fig. 3 (A) Calculated total neutron scattering coefficients (τ) and (B) measured neutron scattering profiles for selected electrolyte solvents. Al (111) and (200) peaks in (B) arise from the Al sample cell.

3.2. Comparison of *ex situ* and *in situ* electrochemistry

A differential capacity (dQ_c/dV) curve for the first cycle of a Si thin-film coin cell cycled galvanostatically at $10 \mu\text{A}$ is shown in Fig. 4. Previous studies have identified the major electrochemical reactions that take place during the first lithiation of Si thin-film electrodes with a 0.1 M LiTFSI in PF5M₂ electrolyte: SEI formation, ~ 1.0 V (Fig. 4, green ●); adventitious oxide lithiation, 0.48 V (orange ■); irreversible Si lithiation feature, 0.26 V (blue ◆); first lithiation step, 0.21 V (red ▲); second lithiation step, < 0.07 V (red ▲); and delithiation, 0.40 V and 0.54 V (red ▼).³³ These voltages were used to identify regions of interest for the NR studies described below. Furthermore, additional coin cells were cycled to 0.6 V, 0.4 V, 0.2 V, 0.07 V, and 2.5 V (Fig. 4, black arrows) for *ex situ* XPS investigations to support the NR investigation of the SEI chemistry. A detailed analysis of the chemical composition and evolution of the SEI as determined via *ex situ* XPS is discussed elsewhere.³³

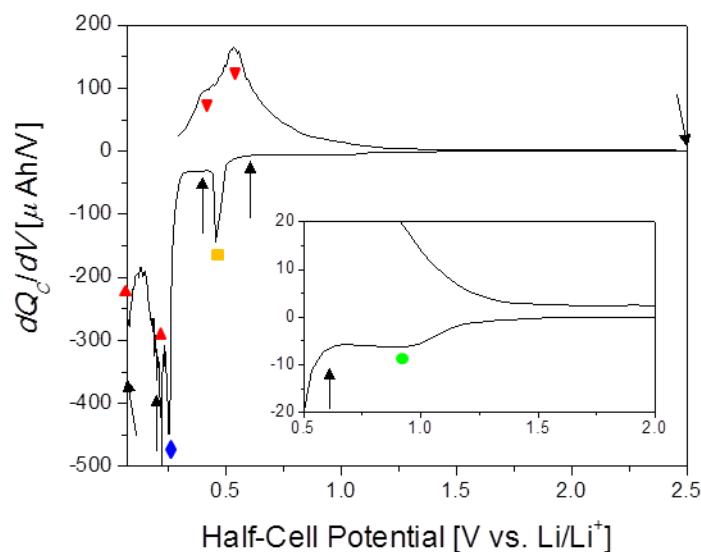


Fig. 4 Differential capacity curve for the first cycle of a Si thin-film half-cell used for *ex situ* analysis. Arrows mark stopping potentials for *ex situ* XPS. Shapes mark identified electrochemical reactions: SEI formation (green ●), SiO₂ lithiation (orange ■), irreversible lithiation (blue ◆), Si lithiation (red ▲), and Si delithiation (red ▼).

Fig. 5 shows the voltage and current profiles for the electrode used in the *in situ* NR cell as function of time. The NR data was collected during the rest steps for the voltage and current collection. While the cycling of battery materials is typically performed galvanostatically (constant current), the high resistance of the electrode used in the NR cell resulted in large overpotentials which made stopping at predetermined cell potentials difficult. For this reason, a hybrid galvanostatic-potentiostatic (constant voltage) protocol was utilized. By holding the electrode at a predetermined potential and allowing the current to decay, the resistive potential drop will decrease and approach the "true" potential of a traditional cell with a lower resistance, i.e., a coin cell. After this step, an additional relaxation step was performed at open circuit to allow for cell equilibration, e.g., Li redistribution, to prevent compositional changes from occurring

during NR data collection. Even though the cell was allowed to relax at open circuit for 30 min prior to the collection of NR data, continued potential relaxation during NR data collection is apparent; however, this relaxation is quasi-linear and relatively small, implying that any additional changes in the electrode and SEI are minimal and acceptable. Furthermore, as our goal was to characterize the SEI structure very small changes in Li-Si chemistry will not influence the SEI chemistry significantly.

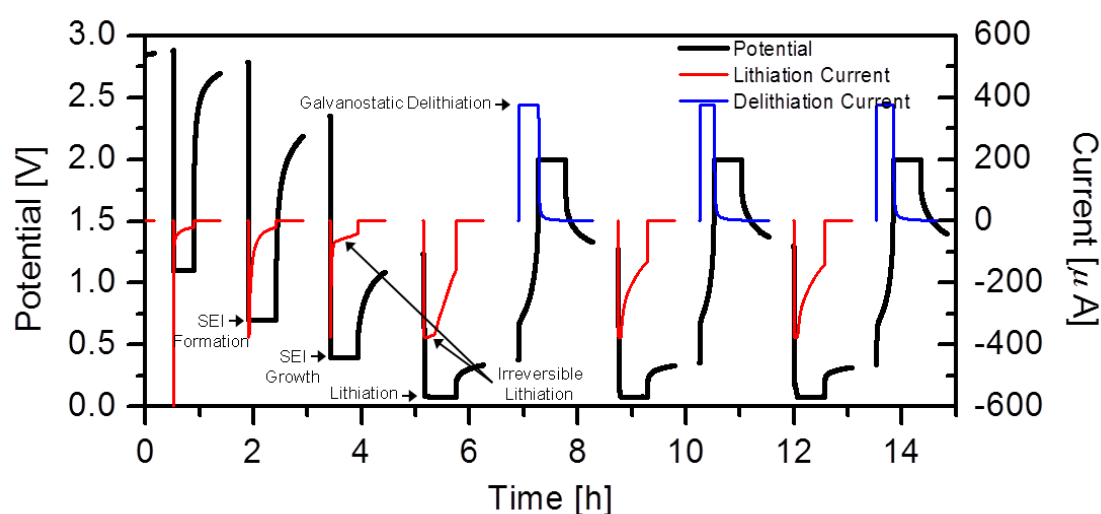


Fig. 5 Electrochemical data for *in situ* NR cell. NR data was collected during the gaps. The voltage profile is shown in black while the current profile is shown in red (lithiation) and blue (delithiation).

3.3. Neutron reflectometry

The electrode used in this study was initially measured in air in order to determine the thickness of the Si electrode, Cu current collector, and any adventitious oxide layers before any chemical or electrochemical reactions took place. It was determined that the Si electrode and copper current collectors were 48.3 and 7.4 nm thick, respectively, and that there was a 2.3 nm SiO₂ layer between the single-crystal Si substrate and the Cu current collector (Table 1). Adding a SiO₂ layer on the surface of the Si electrode in the model

did not improve the fit quality, so it is assumed that any adventitious oxide on the surface of the electrode is negligible. Neutron reflectivity curves obtained for the electrode at different cell potentials and the corresponding fits to the data fits are shown in Fig. 6A-I. From this data one can clearly see no change in the OCV structure and the 1.1 V data indicating no change in the Si electrode stoichiometry and no clear formation of a condensed surface layer or SEI reaction product. Furthermore, there is also no change in the in air structure versus OCV (not shown).

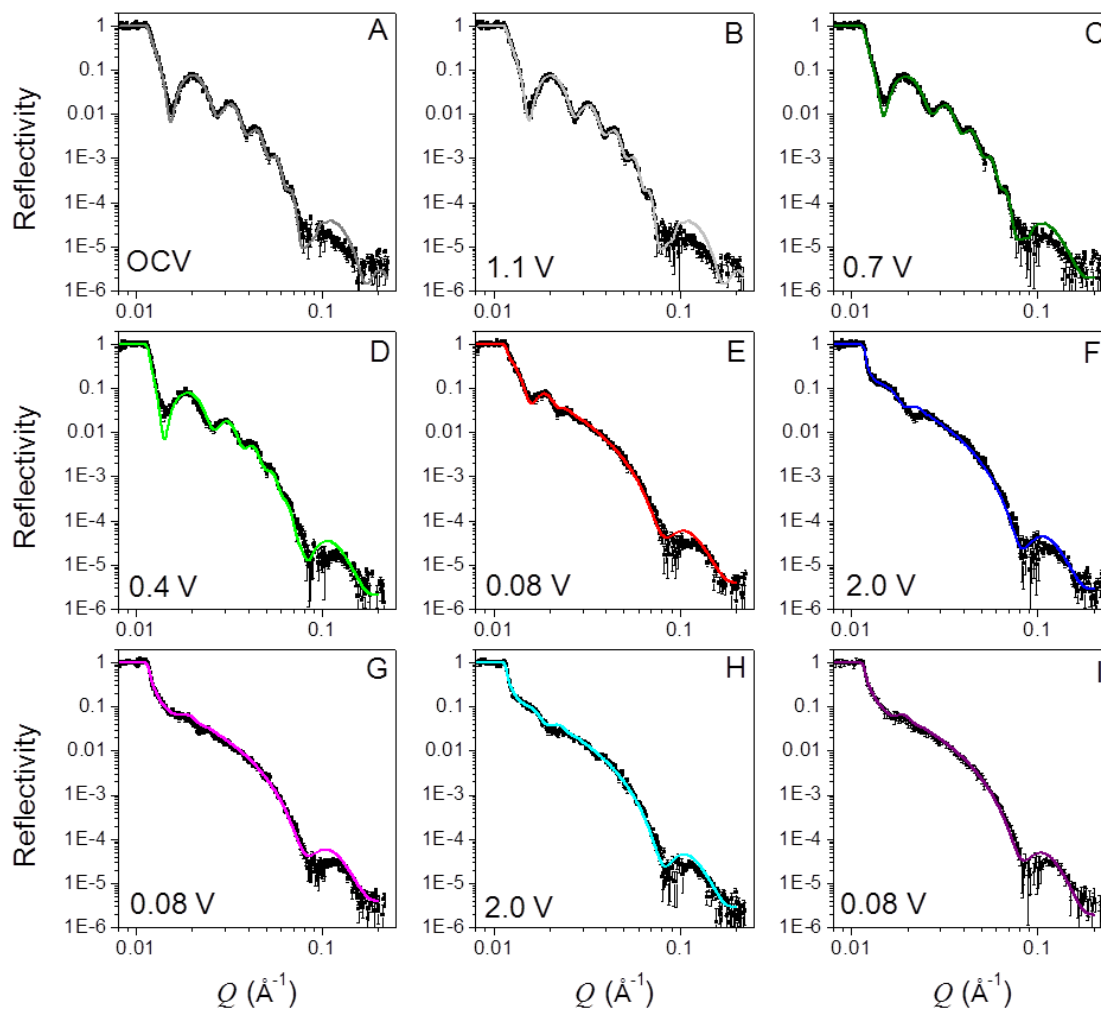


Fig. 6 NR data (black points) and fits (colored lines) in order of collection (A-I).

However, there are subtle but clear differences in the reflectometry profile at high Q 's upon reaching 0.7 V where we see evidence for SEI formation in the CV data (Fig. 4). Fitting this data revealed a very small expansion of the Si layer (48.3 to 48.9 nm) due to a slight lithiation and the formation of a 14.4 nm surface reaction layer we attribute to the SEI. Fig. 7 shows a representation of the SLD as a function of distance from the Cu/Si interface determined from the fits to the NR data. From this plot, and Table 1, we see that the SEI has a refined SLD of 4.5 which is lower than the experimentally measured SLD of the electrolyte ($4.8 \times 10^{-6} \text{ \AA}^{-2}$). This lower SLD has to be due to the formation of a reaction phase with slightly higher Li content than the bulk electrolyte or a film made from the electrolyte but with a lower density than the electrolyte. Given that a significant decrease in density with solid formation is unlikely and additional evidence of Li in the SEI layer (discussed below) this reduction in SLD has to be due to an increase in the Li content of the SEI. Upon continued lithiation (0.4 V) we see a further loss in structure within the NR data consistent with an increased Li-Si ratio and a slight thickening of the SEI layer (14.4 to 16.7 nm).

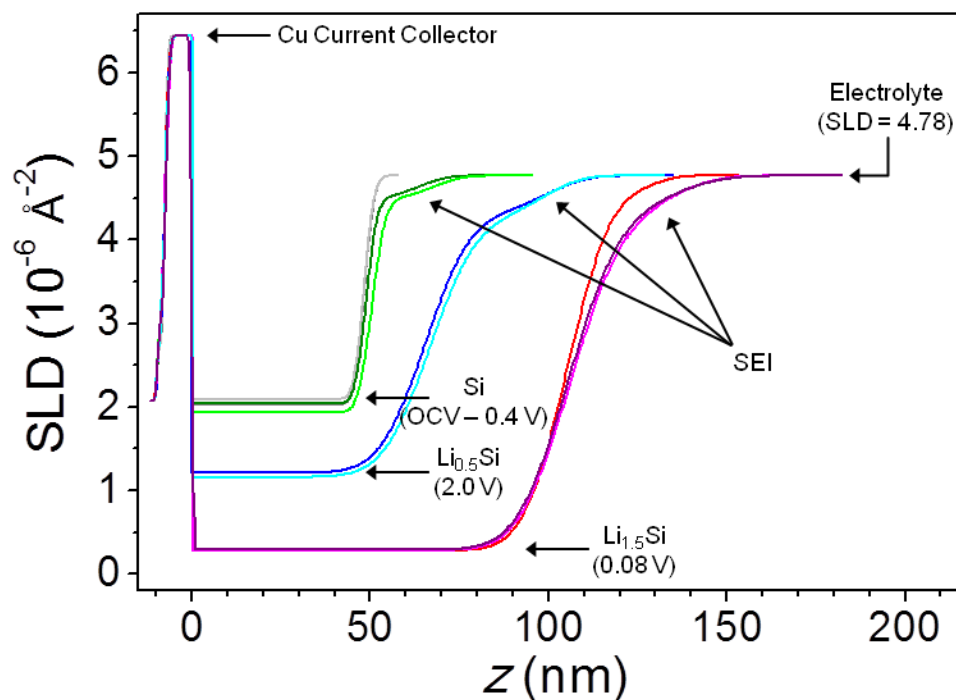


Fig. 7 SLD profiles representing the tabulated fit parameters (Table 1). Colors match the corresponding fits from Fig 7. Major layers are labeled.

Upon further lithiation (0.08 V) we see a significant change in the NR data due to the growth of the Li-Si electrode layer (50.5 to 106 nm) and the further growth in the SEI thickness (16.7 to 26.6 nm). The SLD of the Si-layer decreases from $2.07 \times 10^{-6} \text{ \AA}^{-2}$ to $0.28 \times 10^{-6} \text{ \AA}^{-2}$ due to the incorporation of the low SLD Li. Eq. 2 and 3 indicate that lithiation of the electrode results in the alloy $\text{Li}_{1.5}\text{Si}$, well below the full lithiation capacity of $\text{Li}_{3.75}\text{Si}$. Furthermore, delithiation of the electrode does not go to completion, resulting in an electrode composition of $\text{Li}_{0.45}\text{Si}$, suggesting that a significant portion of the Si lithiation capacity is irreversible.

To confirm that the Li-Si ratio determined via NR is consistent with electrochemical results we compared the *reversible* Li/Si ratio from NR to the reversible

electrochemical capacity of the cell. If the entire electrode area within the O-ring (18 cm^2 , 4.8 cm diameter) was lithiated uniformly, the observed reversible electrochemical capacity ($142 \mu\text{Ah}$) indicates that the electrode has a reversible Li capacity of 0.69 Li per Si. This is significantly smaller than the changes in electrode thickness from NR (Eq. 2) which suggest that the electrode has a reversible capacity of ~ 1.0 Li per Si. Since the Li metal electrode (~ 2.9 cm diameter) is smaller than the Si electrode and large overpotentials are observed in the NR cell a non-uniform lithiation is not unreasonable. The Li/Si ratio determined via NR and *in situ* charge and discharge capacities suggest a uniformly lithiated electrode would possess an area of 10 cm^2 (3.6 cm diameter), closer to the size of the Li electrode yet still significantly larger than the NR footprint ($4 \text{ mm} \times 2 \text{ mm}$ centered on the Si electrode/Li counter electrode). We believe that the electrode area that contains the NR footprint has the most uniform lithiation but that the rest of the electrode lithiates at a much slower rate and to a much lower extent.

One way to confirm this hypothesis is to measure a relaxation cell potential and compare it to Li/Si compositions in the literature. We compared the potential relaxation curves for the *in situ* NR cell (Fig. 5) and a standard coin cell (Fig. 4) operated under galvanostatic conditions to estimate the NR cell's state-of-charge. Fortunately, despite the large differences in cell geometry, the potential relaxation curves for the *in situ* NR cell and coin cell are similar, especially in the lithiated state as demonstrated in Fig. 8. Comparing the potential relaxation rates (Fig. 8B) for the two types of cell we see that the largest differences occur during the early stages of relaxation. Furthermore, the potential relaxation curves in the lithiated state are nearly identical, even for different potentials (0.2 V and 0.07 V). Using this information, an equivalent coin cell potential was

determined for each *in situ* NR cell potential by taking the potential after 10 min of relaxation and subtracting the total relaxation potential drop (10 min) for a comparable coin cell potential. From this analysis we find that the NR cell would have an equivalent potential of 0.18 V relative to a coin cell indicating a Li/Si ratio between 0.9 and 1.9 which is consistent with the NR thicknesses.

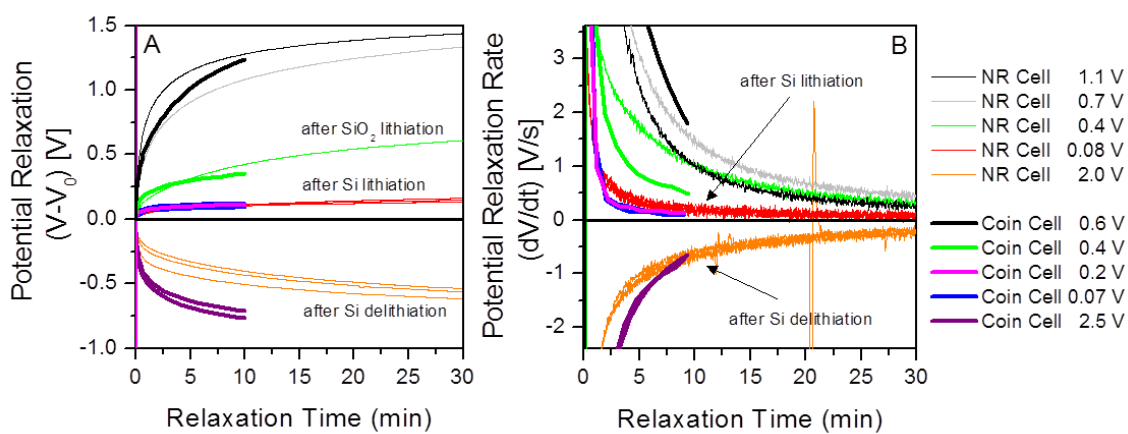


Fig. 8 Potential relaxation (A) and relaxation rate (B) for *in situ* NR and coin cells stopped at various potentials.

As noted previously the SEI thickness increased from 16.7 to 26.6 nm when lithiated to Li_{1.5}Si. Interestingly the SLD of the SEI increased from 4.5 to $4.7 \times 10^{-6} \text{ \AA}^{-2}$. Since *ex situ* XPS indicates that Li content increases during the first lithiation (Sect. 3.4), which is expected to decrease SLD, this increase in SLD could be due to a densification of the SEI or an increase in high scattering length nuclei like ²H, which is not captured via XPS, or C. A large increase in SEI porosity (> 66%) could also explain this change; however, we are unaware of any mechanism which would induce such a sudden and significant increase in porosity and further find this explanation unlikely in a period when

both *in situ* NR and *ex situ* XPS (Sect 3.4) indicate SEI growth, from 14.4 ± 3.2 nm to 26.6 ± 2.1 nm (NR) and 5.3 ± 2.3 nm to 7.9 ± 3.4 nm (XPS).

Upon delithiation the electrode thickness reduces significantly (106 to 65.4 nm) resulting in a composition of $\text{Li}_{0.45}\text{Si}$. Interestingly, the thickness of the SLD increases further to 34.2 nm with a corresponding decrease in the SLD to $4.3 \pm 0.3 \times 10^{-6} \text{ \AA}^{-2}$ indicating an increase in Li content or a decrease in SEI density. Since *ex situ* XPS indicates that Li content is decreasing (Sect. 3.4) during this stage, the change in SLD is most likely due to a change in the average atomic density (N_d) of the SEI. Upon further cycling the SEI layer contracts ($\text{Li}_{1.5}\text{Si}$) significantly (34.2 to 27.3 nm) while maintaining the SEI SLD. A similar expansion and contraction are observed for the later cycle. This swelling and contracting has been previously observed via in NR studies on the SEI formed in traditional carbonate electrolytes.²⁵ The degree of swelling and contraction decreases with additional cycling—a 6.9 nm difference after the first cycle and a 3.6 nm difference after the second cycle—suggesting that the SEI is approaching an equilibrium state. If this contraction and swelling is due in part to changes in the atomic density of the SEI, the lack of corresponding changes in the SLD of the SEI indicate that compositional changes occur in concert, counteracting the effects of changes in atomic density. The most likely compositional difference is the Li content. Increasing the density of the SEI (contraction) increases the SLD while increasing the Li content reduces the SLD. If we assume that the changes in SEI thickness are due primarily to changes in atomic density and changes in the SLD are due primarily to changes in the Li content of the SEI, we can conclude that the SEI on the Si electrode in the lithiated state ($\text{Li}_{1.5}\text{Si}$) has both a higher

atomic density and higher Li content than the SEI on the Si electrode in the delithiated state ($\text{Li}_{0.5}\text{Si}$).

Table 1 Results of NR fits for electrochemically active components. Additional layers and roughness parameters included in Electronic Supplementary Material Table S1.

Potentiostatic Voltage	Equivalent Coin Cell Potential [V]	Si Electrode Thickness [nm]	Li/Si	SEI Thickness [nm]	SEI SLD [10^{-6} \AA^{-2}]	χ^2
In air		48.3 ± 0.1				2.2
OCV	2.88	48.4 ± 0.1	0.00			2.0
1.1 V	1.30	48.3 ± 0.1	0.00			1.8
0.7 V	0.70	48.9 ± 0.1	0.01	14.4 ± 3.2	4.5 ± 0.1	2.3
0.4 V	0.55	50.5 ± 0.5	0.06	16.7 ± 6.4	4.5 ± 0.2	7.0
0.08 V	0.18	106.0 ± 0.3	1.53	26.6 ± 2.1	4.7 ± 0.1	2.9
2.0 V	2.20	65.4 ± 1.1	0.45	34.2 ± 7.2	4.3 ± 0.3	4.1
0.08 V	0.18	105.9 ± 0.7	1.53	27.3 ± 2.3	4.3 ± 0.1	3.0
2.0 V	2.27	66.9 ± 0.6	0.49	32.2 ± 1.5	4.3 ± 0.1	3.2
0.08 V	0.17	105.5 ± 0.7	1.52	28.6 ± 4.0	4.3 ± 0.1	3.9
2.0 V	2.30					

3.4. Ex situ XPS

Most of the communities understanding of SEI chemistry comes from traditional *ex situ* methods like X-ray photoelectron spectroscopy. To understand how the SEI chemistry measured from the reflectometry data compares with traditional XPS studies we performed a detailed analysis of previously collected XPS data to estimate layer thicknesses and compositions. The published XPS data indicates that the SEI chemistry in the PF5M₂ electrolytes were very similar to a standard EC/DMC based electrolyte. Indeed the SEI was shown to contain LiF and Li₂CO₃ type components as well as organic carbonates (C 1s: **CO**₃, 289 eV; O 1s: C=**O**, 532 eV, and C-**O**, 533 eV), carboxylates (C 1s: **CO**₂, 289 eV; O 1s: C=**O** and C-**O**), ethers/esters (C 1s: **CO**, 285.5 eV; O 1s: C-**O**),

and fluorides (C 1s: CF, 287 eV; F1s: CF 689 eV) in similar concentrations. For this work we turned our attention to the Si 2p spectra collected for the samples, which was not previously discussed in great detail. Given that the XPS probe depth can be used to estimate layer thickness using Eq. 5:

$$I(A) = F\sigma(A) \sum_i \left(\int_0^{L_i} N_{d,i}(A) e^{-\frac{x}{\lambda_i}} dx \prod_j^{i-1} e^{-\frac{L_j}{\lambda_j}} \right) \quad (5)$$

where $I(A)$ is the signal intensity for atom A , F is a prefactor that is determined by the experimental conditions, $\sigma(A)$ is the standard sensitivity factor for atom A , L_i is the thickness of layer i ($i = 1$ for the top layer), λ_i is the electron inelastic mean free path for layer i , and $N_{d,i}(A)$ is the number density (atoms/nm³) for atom A in layer i . The only source of Si is the electrode and adventitious oxide, so the Si 2p signal (Fig. 9) and Eq. 5 can be used to estimate the SEI (Layer 1) thickness, since $N_d(\text{Si})$ and thickness are known for those layers. For the as-fabricated electrodes, no Cu signal from the current collector is detected, so the Si layer (Layer 3) can be treated as infinitely thick. Assuming the adventitious oxide is SiO₂, the oxide layer (Layer 2) thickness can be calculated from the ratio of the integrated intensity of the SiO₂ and Si peak in the Si 2p spectrum. In general, λ is material dependent; however, most materials have $\lambda = 3.5 \pm 1.5$ nm.^{6, 7, 37, 38} There is no simple method for determining λ for arbitrary materials, so a uniform $\lambda = 3.5 \pm 1.5$ nm was assumed for all calculations. X-ray attenuation does occur within the sample; however, the penetration depth of X-rays is on the order of mm and can be neglected without the introduction of error for all subsequent calculations.

For an accurate determination of the SEI thickness, changes in the thickness and $N_d(\text{Si})$ of Layers 2 and 3 must be taken into account. Fortunately, the reactions in these layers are relatively well-defined in the literature and electrochemically well-separated.^{6, 7, 33, 39} At 0.5 V, the adventitious oxide (Layer 2) undergoes irreversible lithiation ($4e^- + 4\text{Li}^+ + \text{SiO}_2 \rightarrow 2\text{LiO}_2 + \text{Si}$) and is assumed to form an intimate mixture of LiO_2 and Si, both of which have well-known densities. At lower voltages (<0.3 V) lithiation of the Si ($xe^- + x\text{Li}^+ + \text{Si} \rightarrow \text{Li}_x\text{Si}$) in Layers 2 and 3 begins to occur, where $N_d(\text{Si})$ can be determined from Eq. 2. Based on the NR results, $x = 1.56$ for 0.2 V, $x = 3.75$ for 0.07 V, and $x = 0.5$ for 2.5 V. Although the differential capacity curves indicate that the electrode does not reach full lithiation ($\text{Li}_{3.75}\text{Si}$) at 0.07 V, assuming full lithiation underestimates SEI thickness and represents the most conservative estimate and is sufficient for analysis. The thickness, composition, and $N_d(\text{Si})$ for each layer as a function of SOC are summarized in Table 2.

Only Layer 1 (SEI) contains information that is not defined *a priori* for this analysis so only the properties of that layer can be determined. *Ex situ* XPS shows that the SEI forms electrochemically above 0.6 V (4.5 ± 1.9 nm) followed by continued growth during SiO_2 (0.4 V, 5.3 ± 2.3 nm) and Si (0.2 V, 7.9 ± 3.4) lithiation. A Si signal for the first full lithiation (0.07 V) was not collected, so it is not possible to determine an SEI thickness for this state; however, given the low reduction stability of the fluorinated electrolyte,^{8, 30, 31, 33} it is likely that the thickness of the SEI in this state is greater than in the 0.2 V state. The SEI then shrinks during delithiation (2.5 V, 6.9 ± 3.0 nm) and swells during the second lithiation (0.07 V, 12.5 ± 5.4 nm). This is the *opposite* of the swelling behavior observed via NR indicating that the washing procedure removes part of the SEI

layer chemistry or changes the density of the surface layer by removing parts of the condensed surface layer. This effect was explicitly studied on highly-oriented pyrolytic graphite electrodes for a 1.5 M LiTFSI in EC electrolyte with and without additives, where the removal of SEI components is universally observed.

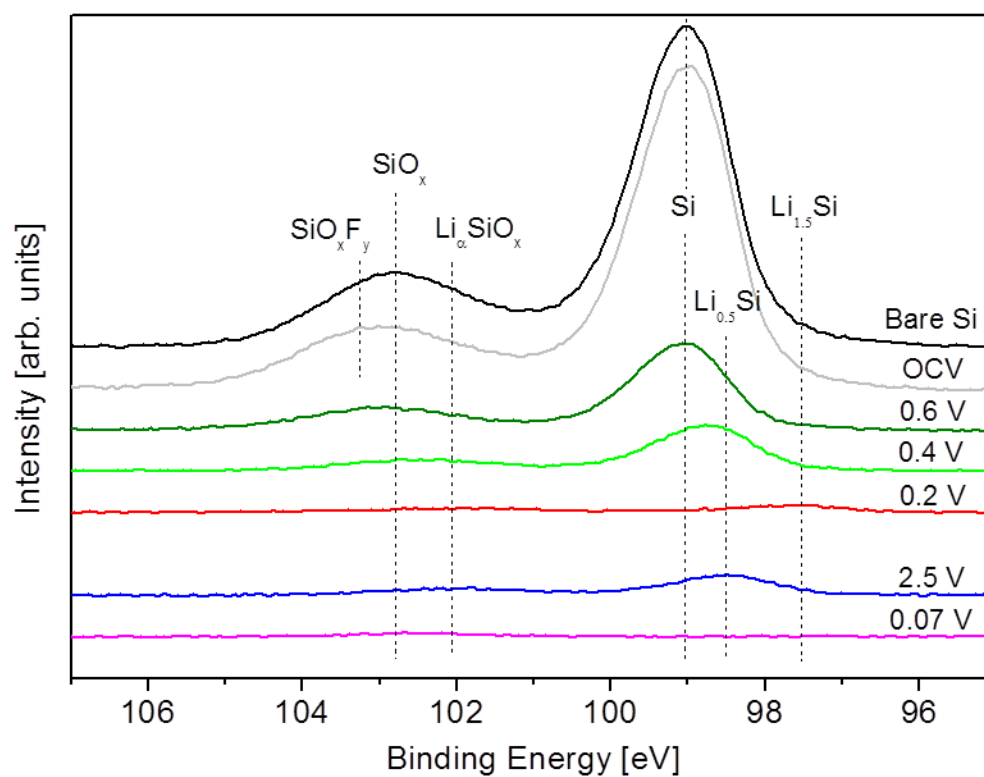


Fig. 9 *Ex situ* Si 2p XPS spectra used to calculate SEI thickness using Eq. 5. Spectra colored to match that of the closest SLD profile determined from NR.

Table 2 Layer thicknesses derived from *ex situ* XPS. Uncertainty derived from $\lambda = 3.5 \pm 1.5$ nm. SLD range of the SEI estimated using the atomic density (N_d) of LiF and EC. High-resolution Si data was not collected for the first 0.07 V sample, due to the fact that no Si signal was detected in the low-resolution spectrum.

Potential	Integrated Intensity [arb. units]	Layer 1 (SEI)		Layer 2 (SiO ₂)		Layer 3 (Si)		
		Thickness [nm]	SLD [10^{-6} \AA^{-2}]	Composition	Thickness [nm]	$N_d(\text{Si})$ [nm^{-3}]	Composition	$N_d(\text{Si})$ [nm^{-3}]
Bare Si	98.70			SiO ₂	1.9 ± 0.8	26.54	Si	49.94
OCV	96.79			SiO ₂	1.9 ± 0.8	26.54	Si	49.94
0.6 V	26.40	4.5 ± 1.9	4.8 ± 0.7	SiO ₂	1.9 ± 0.8	26.54	Si	49.94
0.4 V	14.62	5.3 ± 2.3	4.7 ± 0.7	Li ₂ O + Si	3.5 ± 1.5	14.43	Si	49.94
0.2 V	3.45	7.9 ± 3.4	3.7 ± 0.5	Li ₂ O + Li _{1.5} Si	4.7 ± 2.0	10.69	Li _{1.56} Si	22.61
0.07 V			3.6 ± 0.5	Li ₂ O + Li _{3.75} Si				
2.5 V	6.93	6.9 ± 3.0	4.4 ± 0.6	Li ₂ O + Li _{0.50} Si	3.9 ± 1.7	12.97	Li _{0.5} Si	35.99
0.07 V	0.83	12.5 ± 5.4	4.1 ± 0.6	Li ₂ O + Li _{3.75} Si	5.0 ± 2.2	7.84	Li _{3.75} Si	12.78

After correcting for (attenuated) O and Li signals from the Si and SiO₂ layer, the SLD of the SEI can be estimated directly from the atomic composition determined via XPS (Fig. 10) using Eq. 1. This requires an assumption of the average atomic density (N_d) of the SEI. For this purpose, a range of model N_d was chosen: high density (LiF), moderate density (Li₂CO₃), and low density (EC). Since the N_d of the SEI is unknown, the absolute SLD of the SEI determined via this method is not particularly useful without additional context. Instead changes in the SLD of the SEI can be discussed according to the changes in the atomic composition that most influenced that change. The SLD of the SEI initially starts out high (0.6 V, $4.8 \pm 0.7 \cdot 10^{-6} \text{ \AA}^{-2}$, 22.1% Li; 0.4 V, $4.7 \pm 0.7 \cdot 10^{-6} \text{ \AA}^{-2}$, 23.8% Li) but decreases during lithiation as the Li content of the SEI increases (0.2 V, $3.7 \pm 0.5 \cdot 10^{-6} \text{ \AA}^{-2}$, 34.9% Li; 0.07 V, $3.6 \pm 0.5 \cdot 10^{-6} \text{ \AA}^{-2}$, 35.2% Li). Delithiation of the electrode causes the SLD to increase as the Li content drops (2.5 V, $4.4 \pm 0.6 \cdot 10^{-6} \text{ \AA}^{-2}$,

27.2% Li). The SLD then drops again as the Li content increases during lithiation (0.07 V, $4.1 \pm 0.6 \times 10^{-6} \text{ \AA}^{-2}$, 29.8% Li).

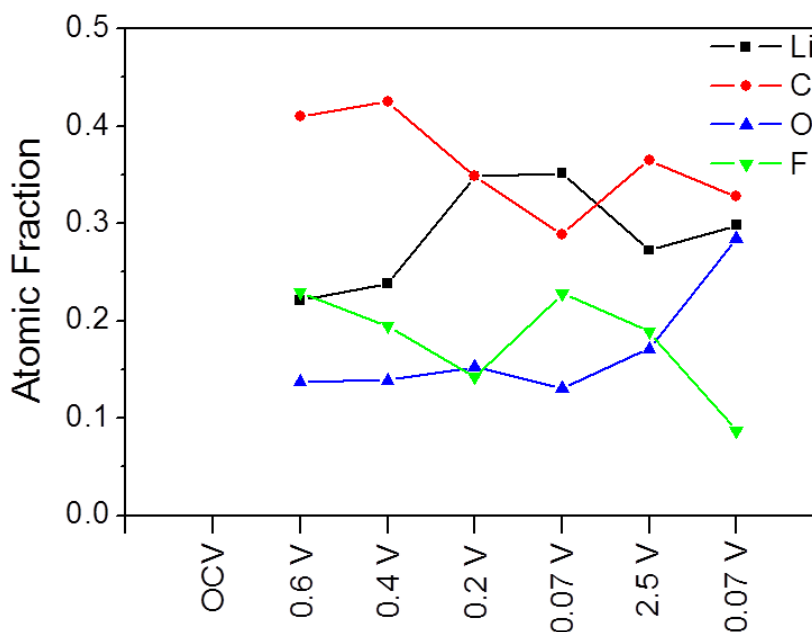


Fig. 10 Atomic compositions of the SEI determined from XPS and used to estimate SLD.

The changes in the SLD are simplest to explain in terms of changes in the concentration of Li salts (LiF, Li_2CO_3 , etc.), which are less likely than organic (C, F, O) species to be removed during washing. However, all of the atoms composing the SEI affect its SLD. Changes in both the C (6.65 fm) and Li (-1.90 fm) content of the SEI will drastically affect the predicted SLD. One of the major changes in SEI composition is the increase of F and decrease of O with cycling (Fig. 10); however, since F and O have similar scattering lengths (5.65 fm and 5.80 fm, respectively), this change does not have a significant effect on the SLD of the SEI. XPS also does not capture the contribution of hydrogen to the SLD of the SEI, meaning that this method of predicting the SLD of the SEI will underestimate the SLD of a deuterated SEI and overestimate the SLD of a

protiated SEI proportional to the hydrogen content, as D (6.67 fm) and H (-3.74 fm) have scattering lengths higher and lower than that of any of the other SEI components.

3.5. Ex situ NMR

NMR was carried out on the electrolyte before and after cycling in order to determine to what extent soluble electrochemical byproducts were formed during cycling. Lithium perfluoroglutarate (PF5Li₂) was previously observed in a cycled electrolyte via infrared absorption spectroscopy,³³ suggesting that electrochemical de-esterification of the methyl ester takes place, similar to what is seen in the initial stages of SEI formation in organic carbonates.⁸

Multinuclear NMR (Fig. 11) of deuterated and protiated electrolytes shows subtle changes that occur during cycling. Major signals belong to PF5M₂ [¹H: 1.0 (singlet); ¹³C: 15.0 (singlet), 109.4 (triplet of triplets), 111.2 (triplet of quintets), 160.2 (multiplet); ¹⁹F: -125.2 (singlet), 119.6 (singlet)] and TFSI⁻ [¹³C: 120.6 (quartet); ¹⁹F: -80.8 (singlet)]. The chemical shift of the CH₃ group in the deuterated electrolytes is slightly different than that of the protiated electrolyte (4.00 ppm vs. 4.04 ppm in ¹H and 54.34 (septet) vs. 55.04 ppm (singlet) in ¹³C). The deuterated electrolytes have a relatively intense peak at 3.85 ppm in the ¹H spectrum which is most likely due to MeOH (CD₃OH) formed by hydrolysis of d₆-PF5M₂ by trace H₂O impurities. The corresponding peak in the protiated electrolytes is obscured by the ¹H-¹³C satellite. The signal for the CH₃ of MeOH (¹H: 3.6 ppm) appears in the protiated electrolytes but not the deuterated electrolytes, consistent with the low proportion (<0.6 %) of CHD₂ in the deuterated electrolyte.

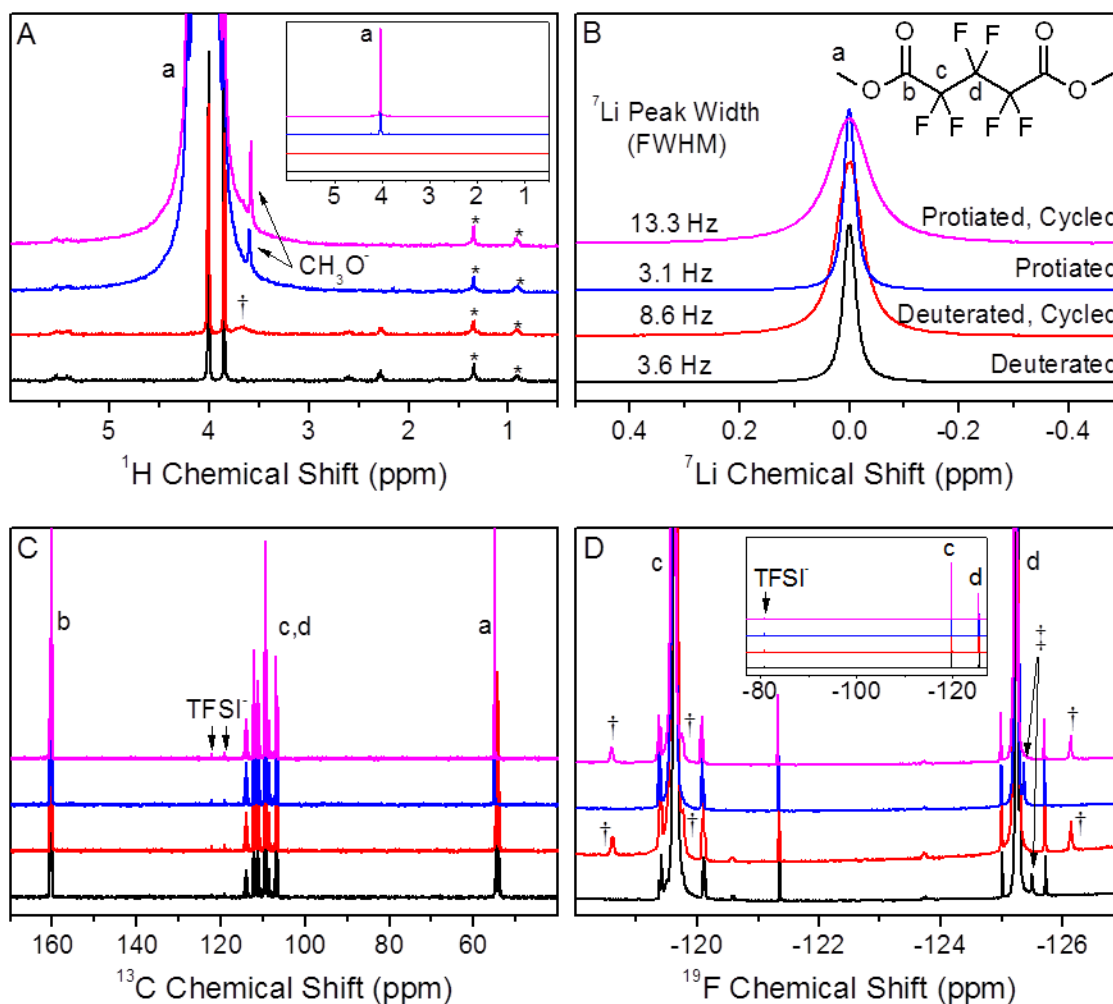


Fig. 11 ^1H (A), ^7Li (B), ^{13}C (C), and ^{19}F (D) NMR spectra of deuterated and protiated electrolytes before and after cycling. Peaks corresponding to PF_5M_2 (a-d) and the TFSI anion are labeled. Insets in ^1H and ^{19}F spectra are 1/1000 \times scale to show full intensity of PF_5M_2 and TFSI peaks. Signals unique to the cycled (\dagger) and uncycled (\ddagger) electrolytes as well as signals attributed to volatile species in the epoxy sealant (*) are labeled.

Additional signals are of low intensity (<0.1% of primary peaks), illustrating the necessity of using neat (no deuterated solvent) electrolytes during analysis in order to observe impurities and electrochemically-formed compounds. All species unique to cycled and uncycled electrolytes appear in both protiated and deuterated electrolytes. The broad peak at 3.7 ppm in the ^1H spectrum (Fig. 11A, \dagger) of the cycled, deuterated

electrolyte does not show a corresponding intense peak in the protiated electrolyte, suggesting that this peak may be due to an adventitious ^1H source, likely ambient H_2O , whose chemical shift is highly environment-dependent.^{40, 41} Adventitious sources of H have ^1H signals that are independent of the level of deuteration of the electrolyte, unlike any hydrogenous species formed from the electrolyte during cycling.

The most significant difference between the cycled and uncycled electrolytes is the intensity and width of the ^7Li signal (Fig. 11B). The changes in peak width for the protiated (3.1 Hz \rightarrow 13.3 Hz) and deuterated (3.6 Hz \rightarrow 8.6 Hz) electrolytes with cycling is consistent with the formation of PF_5Li_2 , which would reduce symmetry around the quadrupolar ^7Li nuclear, increasing relaxation rate and peak width. The intensity of the ^7Li signal increases by 18% for the protiated electrolyte and by 28% for the deuterated electrolyte. Though it is difficult to integrate the ^{19}F signals, due to overlap from intense nearby peaks, the differences in the intensity changes in the ^7Li signal are qualitatively consistent with the differences in intensity of the ^{19}F peaks (Fig. 11D, †) in the protiated and deuterated electrolytes. If due solely to electrochemical formation of PF_5Li_2 , a 28% increase in the ^7Li signal (0.1 M) would correspond to the formation of 14 mM PF_5Li_2 . The appearance of ^{19}F signals (†) at ~ 0.003 times the intensity of the primary PF_5M_2 (5.5 M) peaks at similar chemical shifts is consistent with the formation of PF_5Li_2 . This observation is further evidence that PF_5Li_2 is the primary soluble product formed during electrochemical cycling. It is, however, unclear whether the differences in the ^7Li spectrum between the protiated and deuterated electrolytes are due to slight differences in the electrochemical discharge conditions, e.g., electrolyte volume and cell resistance, or chemical differences caused by an isotopic effect, e.g., PF_5Li_2 solubility.

It is difficult to identify the specific species formed during cycling solely from the chemical shifts in one-dimensional NMR data; though it is clear that only a small number of species (at relatively low concentrations) are formed. Since all other impurity signals present in the uncycled electrolyte except for one (Fig. 11D, ‡) are also present in the cycled electrolyte at roughly the same concentrations, these impurities are most likely electrochemically inert and do not affect SEI formation or composition. Based on the above analysis, PF5Li₂ is the only *soluble* species formed during electrochemical cycling. Using Eq. 3, the SLD of the electrolyte is expected to change from $4.78 \times 10^{-6} \text{ \AA}^{-2}$ to 4.77 after discharging the cell. NR is not sensitive to such a small change in the electrolyte SLD, so it is assumed to remain constant during cycling. Additionally, this analysis does not eliminate the possibility of species formed that are soluble in DMC and would be removed during washing prior to *ex situ* XPS.

4. Discussion

Fig. 12 compares the thickness and SLD of the SEI as determined via *ex situ* XPS (Table 2) and *in situ* NR (Table 1). XPS suggests that the SEI swells during lithiation and contracts during delithiation. NR suggests the opposite, and previous *in situ* NR measurements using a traditional EC/DMC electrolyte show swelling during delithiation and contraction during lithiation, in agreement with the NR results shown here.²⁵ XPS also appears to underestimate the SLD of the SEI when compared to NR. The differences between the XPS and NR results have three potential causes: (1) the lack of hydrogen sensitivity in XPS, (2) differences in porosity caused by drying the SEI prior to *ex situ*

analysis, and (3) the removal of SEI components during DMC washing prior to *ex situ* analysis.

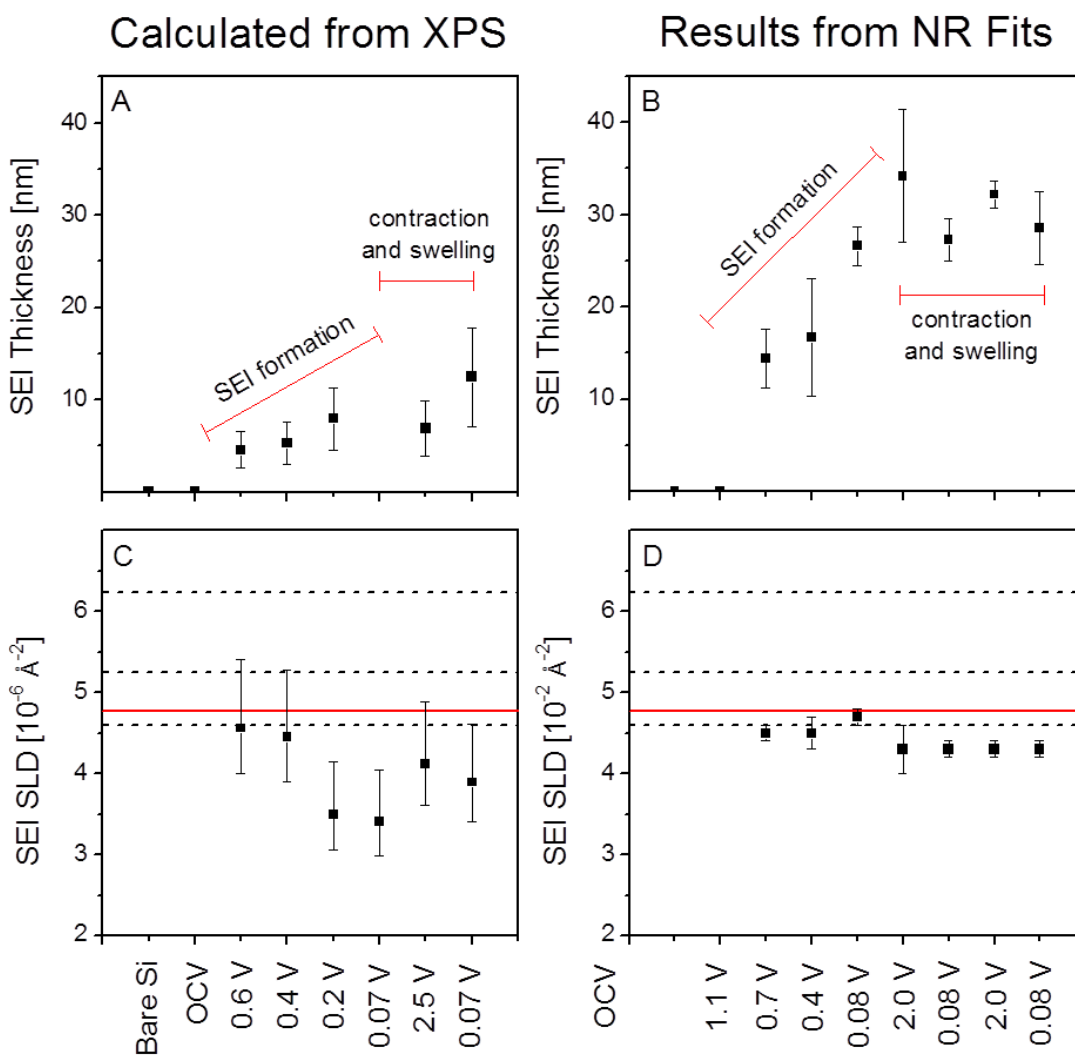


Fig. 12. SEI thickness and SLD as determined via *ex situ* XPS (A, C) and *in situ* NR (B, D). The black dashed lines in C and D indicate the expected SLD for PF5Li₂ at the atomic density of LiF (upper), Li₂CO₃ (middle), and EC (lower). The solid red line indicates the SLD of the electrolyte.

It is possible that SLDs calculated from XPS are low due to the insensitivity of XPS to H, which, in the form of D (6.67 fm), has a higher scattering length than O (5.80 fm), F (5.65 fm), C (6.65 fm), and Li (-1.90 fm). However, the low hydrogen content of the electrolyte makes this possibility unlikely, and neglecting the hydrogen content fails to explain the observed differences in SEI thickness.

Another possibility is that SEI porosity, which would be present only in the *in situ* cell, is responsible for this discrepancy. Assuming these pores are filled with electrolyte, only for the lowest model density ($N_d(\text{SEI}) = N_d(\text{EC})$) can physically reasonable values of porosity be calculated. Reconciling these values would require 40 % to 70 % porosity in most of the cases to obtain the SLD observed via NR, much higher than previously observed values. Since this porosity would collapse entirely during drying, prior to collecting XPS data, the thicknesses determined from NR should be 1.7 to 3.3 times as thick as that determined via XPS. While these results are not physically impossible, they are on the extreme edge of plausibility. For the SEI formed at the end of the first discharge, these values jump to 90 % - 99 % porosity and 10 to 100 swelling. Though a thickness measurement from XPS is not available for this state, it is highly unlikely that an SEI of 0.3 nm to 4.1 nm would be observed. Changes in porosity are also unable to explain why swelling and contracting of the SEI occur during opposite steps when observed through XPS or NR. For these reasons, it is unlikely that porosity of the SEI measured *in situ* is the sole source of the differences between SEI thickness and SLD measured via XPS or NR.

The third possibility is that rinsing the electrodes prior to XPS, necessary to remove excess electrolyte, dissolves certain components of the SEI. We tested only for

the formation of species which were soluble in PF5M₂, in which most Li salts are not very soluble, and found only small amounts of PF5Li₂ (also likely of low solubility). Li salts and organic monomers that are part of the SEI are likely to be much more soluble in DMC, leaving only high molecular weight polymers and highly insoluble Li salts, e.g., LiF, Li₂O, Li₂CO₃, to be detected after washing. Identification of dissolved species, e.g., via NMR of electrode rinse, is made difficult by the low concentration of any extracted species and their likely similarity to the electrolyte itself, which is a significant component of the residue on the electrode prior to rinsing. However, since the SLD of the SEI ($4.3 \pm 0.1 \times 10^{-6} \text{ \AA}^{-2}$) is lower than the SLD of PF5Li₂ at the lowest proposed density (EC, $4.6 \times 10^{-6} \text{ \AA}^{-2}$), the SEI is more Li-rich than both polymerized PF5M₂ and solid PF5Li₂.

NR indicates that the PF5M₂ electrolyte forms an SEI that's 32 ± 8 nm thick. This result is consistent with the generally theorized—albeit broad—range for a typical SEI thickness of one to hundreds of nm^{8, 9} and similar to previous NR measurements of the thickness of the SEI formed in EC/DMC electrolytes.²⁵ Both *in situ* NR and *ex situ* XPS indicate that the SEI swells and contracts during cycling. NR indicates that the SEI contracts by up to 22% during lithiation and swells during delithiation, slowly approaching an equilibrium thickness. XPS suggests the opposite, up to 45% contraction during delithiation and swelling during lithiation. XPS also underestimates the SLD of the SEI by up to 25% and underestimates the thickness of the SEI by a factor of 3 to 4. Combining *in situ* atomic force microscopy and *ex situ* XPS, Cresce *et al.* have shown that the SEI formed in a carbonate electrolyte (1.32 M LiTFSI in EC) on highly oriented pyrolytic graphite (HOPG) is composed of a hard, primarily inorganic layer on the

electrode surface and soft, organic layer on top of that. Rinsing the HOPG electrode after cycling was shown to remove the soft outer layer of the SEI and leave a layer rich in inorganic carbonates and fluorides.⁹ This can explain the differences observed in this study between *ex situ* XPS and *in situ* NR. The inner, thin Li-rich (low SLD) layer is observed in XPS after washing away the outer, thick organic layer (high SLD) that is observed in NR.

6. Conclusion

This study provides direct evidence for the contention that rinsing electrodes prior to *ex situ* characterization modifies the SEI, leading to potentially fallacious conclusions about the function, composition, and optimization of SEIs.^{2, 8, 9, 11, 13, 14, 21, 22, 25} In order to obtain an accurate description of the SEI it is necessary to characterize it *in situ*. Unfortunately, *in situ* characterizations are difficult to perform, prone to interference, and often limited in scope. For example, *in situ* NR requires extremely smooth interfaces and low-scattering electrolytes, is not reliable in the absence of an accurate and relatively simple model, and does not provide chemical information. The composition and function of the SEI is complicated and will require multiple complementary *in situ* techniques to fully understand. Recently, strides have been made to develop robust methods for *in situ* characterization; however, *ex situ* characterizations are currently far more common.⁸

Acknowledgements

Student support and materials for ester synthesis and scattering profiles provided by the U.S. National Science Foundation under Grant No. DGE-1069091. Student

support for the electrochemical, XPS, and ATR-IR studies performed at Oak Ridge National Laboratory provided by the U.S. Department of Energy, Office of Science, Office of Workforce Development for Teachers and Scientists, Office of Science Graduate Student Research (SCGSR) program. The SCGSR program is administered by the Oak Ridge Institute for Science and Education for the DOE under contract number DE-AC05-06OR23100. The equipment, materials and technical guidance at ORNL was supported by the Materials Sciences and Engineering Division, Office of Basic Energy Sciences, U.S. Department of Energy under contract with UT-Battelle, LLC (GMV – XPS, ATR-IR, electrochemical) and the Fluid Interface Reactions, Structures, and Transport (FIRST) Center, an Energy Frontier Research Center funded by the U.S. Department of Energy, Office of Science, Office of Basic Energy Sciences (RLS – Conductivity, ATR-IR). T.M.F would like to thank Dr. C. Sotiriou-Leventis for help in formulating the perfluorocarboxylate ester synthesis.

References

1. H. Q. Pham, K. M. Nam, E. H. Hwang, Y. G. Kwon, H. M. Jung and S. W. Song, *Journal of the Electrochemical Society*, 2014, **161**, A2002-A2011.
2. P. Verma, P. Maire and P. Novák, *Electrochimica Acta*, 2010, **55**, 6332-6341.
3. K. C. Klavetter, S. M. Wood, Y.-M. Lin, J. L. Snider, N. C. Davy, A. M. Chockla, D. K. Romanovicz, B. A. Korgel, J.-W. Lee, A. Heller and C. B. Mullins, *Journal of Power Sources*, 2013, **238**, 123-136.
4. C. K. Chan, R. Ruffo, S. S. Hong and Y. Cui, *Journal of Power Sources*, 2009, **189**, 1132-1140.
5. X. Chen, X. Li, D. Mei, J. Feng, M. Y. Hu, J. Hu, M. Engelhard, J. Zheng, W. Xu, J. Xiao, J. Liu and J.-G. Zhang, *ChemSusChem*, 2014, **7**, 549-554.
6. B. Philippe, R. Dedryvère, M. Gorgoi, H. Rensmo, D. Gonbeau and K. Edström, *Chemistry of Materials*, 2013, **25**, 394-404.
7. B. Philippe, R. Dedryvère, J. Allouche, F. Lindgren, M. Gorgoi, H. Rensmo, D. Gonbeau and K. Edström, *Chemistry of Materials*, 2012, **24**, 1107-1115.
8. K. Xu, *Chem Rev*, 2014, **114**, 11503-11618.
9. A. v. Cresce, S. M. Russell, D. R. Baker, K. J. Gaskell and K. Xu, *Nano Letters*, 2014, **14**, 1405-1412.
10. O. Dolotko, A. Senyshyn, M. J. Mühlbauer, K. Nikolowski and H. Ehrenberg, *Journal of Power Sources*, 2014, **255**, 197-203.
11. M. T. McDowell, S. W. Lee, J. T. Harris, B. A. Korgel, C. Wang, W. D. Nix and Y. Cui, *Nano Lett*, 2013, **13**, 758-764.
12. L. Zhou, M. Leskes, A. J. Ilott, N. M. Trease and C. P. Grey, *J Magn Reson*, 2013, **234**, 44-57.
13. K. Edström and M. Herranen, *Journal of The Electrochemical Society*, 2000, **147**, 3628-3632.
14. P. Novák, D. Goers, L. Hardwick, M. Holzapfel, W. Scheifele, J. Ufheil and A. Würsig, *Journal of Power Sources*, 2005, **146**, 15-20.
15. M. Bianchini, E. Suard, L. Croguennec and C. Masquelier, *The Journal of Physical Chemistry C*, 2014, **118**, 25947-25955.
16. I. A. Bobrikov, A. M. Balagurov, C.-W. Hu, C.-H. Lee, T.-Y. Chen, S. Deleg and D. A. Balagurov, *Journal of Power Sources*, 2014, **258**, 356-364.
17. H. Liu, C. R. Fell, K. An, L. Cai and Y. S. Meng, *Journal of Power Sources*, 2013, **240**, 772-778.
18. M. Roberts, J. J. Biendicho, S. Hull, P. Beran, T. Gustafsson, G. Svensson and K. Edström, *Journal of Power Sources*, 2013, **226**, 249-255.
19. X.-L. Wang, K. An, L. Cai, Z. Feng, S. E. Nagler, C. Daniel, K. J. Rhodes, A. D. Stoica, H. D. Skorpenske, C. Liang, W. Zhang, J. Kim, Y. Qi and S. J. Harris, *Sci. Rep.*, 2012, **2**.
20. B. Jerliu, L. Dorrer, E. Huger, G. Borchardt, R. Steitz, U. Geckle, V. Oberst, M. Bruns, O. Schneider and H. Schmidt, *Physical Chemistry Chemical Physics*, 2013, **15**, 7777-7784.
21. J. E. Owejan, J. P. Owejan, S. C. DeCaluwe and J. A. Dura, *Chemistry of Materials*, 2012, **24**, 2133-2140.

22. M. Hirayama, N. Sonoyama, T. Abe, M. Minoura, M. Ito, D. Mori, A. Yamada, R. Kanno, T. Terashima, M. Takano, K. Tamura and J. i. Mizuki, *Journal of Power Sources*, 2007, **168**, 493-500.
23. J. F. Browning, L. Baggetto, K. L. Jungjohann, Y. Wang, W. E. Tenhaeff, J. K. Keum, D. L. Wood and G. M. Veith, *ACS Applied Materials & Interfaces*, 2014, **6**, 18569-18576.
24. G. M. Veith, L. Baggetto, R. L. Sacci, R. R. Unocic, W. E. Tenhaeff and J. F. Browning, *Chemical Communications*, 2014, **50**, 3081-3084.
25. G. M. Veith, M. Doucet, J. K. Baldwin, R. L. Sacci, T. M. Fears, Y. Wang and J. F. Browning, *The Journal of Physical Chemistry C*, 2015, **119**, 20339-20349.
26. A. Nelson, *J. Appl. Cryst.*, 2006, **39**, 273-276.
27. T. Heitmann and W. Montfrooij, *Practical Neutron Scattering at a Steady State Source*, Mizou Media - University BookStores, 2012.
28. T. C. Hansen and H. Kohlmann, *Zeitschrift für anorganische und allgemeine Chemie*, 2014, **640**, 3044-3063.
29. Sigma-Aldrich, <https://www.sigmaaldrich.com/united-states.html>, (accessed March 10, 2015).
30. L. Hu, Z. Xue, K. Amine and Z. Zhang, *Journal of the Electrochemical Society*, 2014, **161**, A1777-A1781.
31. Z. Zhang, L. Hu, H. Wu, W. Weng, M. Koh, P. C. Redfern, L. A. Curtiss and K. Amine, *Energy & Environmental Science*, 2013, **6**, 1806.
32. T. Böttcher, B. Duda, N. Kalinovich, O. Kazakova, M. Ponomarenko, K. Vlasov, M. Winter and G. V. Röschenthaler, *Progress in Solid State Chemistry*, 2014, **42**, 202-217.
33. T. M. Fears, R. L. Sacci, J. G. Winiarz, H. Kaiser, H. Taub and G. M. Veith, *Journal of Power Sources*, 2015, **299**, 434-442.
34. V. F. Sears, *Neutron News*, 1992, **3**, 26-37.
35. O. Arnold, J. C. Bilheux, J. M. Borreguero, A. Buts, S. I. Campbell, L. Chapon, M. Doucet, N. Draper, R. Ferraz Leal, M. A. Gigg, V. E. Lynch, A. Markvardsen, D. J. Mikkelson, R. L. Mikkelson, R. Miller, K. Palmen, P. Parker, G. Passos, T. G. Perring, P. F. Peterson, S. Ren, M. A. Reuter, A. T. Savici, J. W. Taylor, R. J. Taylor, R. Tolchenov, W. Zhou and J. Zikovsky, *Nuclear Instruments and Methods in Physics Research Section A: Accelerators, Spectrometers, Detectors and Associated Equipment*, 2014, **764**, 156-166.
36. V. L. Chevrier and J. R. Dahn, *Journal of The Electrochemical Society*, 2009, **156**, A454-A458.
37. S. Tanuma, C. J. Powell and D. R. Penn, *Surface and Interface Analysis*, 2005, **37**, 1-14.
38. S. Tanuma, C. J. Powell and D. R. Penn, *Surface and Interface Analysis*, 2011, **43**, 689-713.
39. P. R. Abel, Y.-M. Lin, H. Celio, A. Heller and C. B. Mullins, *ACS Nano*, 2012, **6**, 2506-2516.
40. H. E. Gottlieb, V. Kotlyar and A. Nudelman, *The Journal of Organic Chemistry*, 1997, **62**, 7512-7515.
41. G. R. Fulmer, A. J. M. Miller, N. H. Sherden, H. E. Gottlieb, A. Nudelman, B. M. Stoltz, J. E. Bercaw and K. I. Goldberg, *Organometallics*, 2010, **29**, 2176-2179.

Electronic Supplementary Material

Contents:		Page
Fig. S1	UV-Vis absorption spectra of VOCl_3 solutions	144
Table S1	UV-Vis absorption spectra collected during gel aging	145
References		146

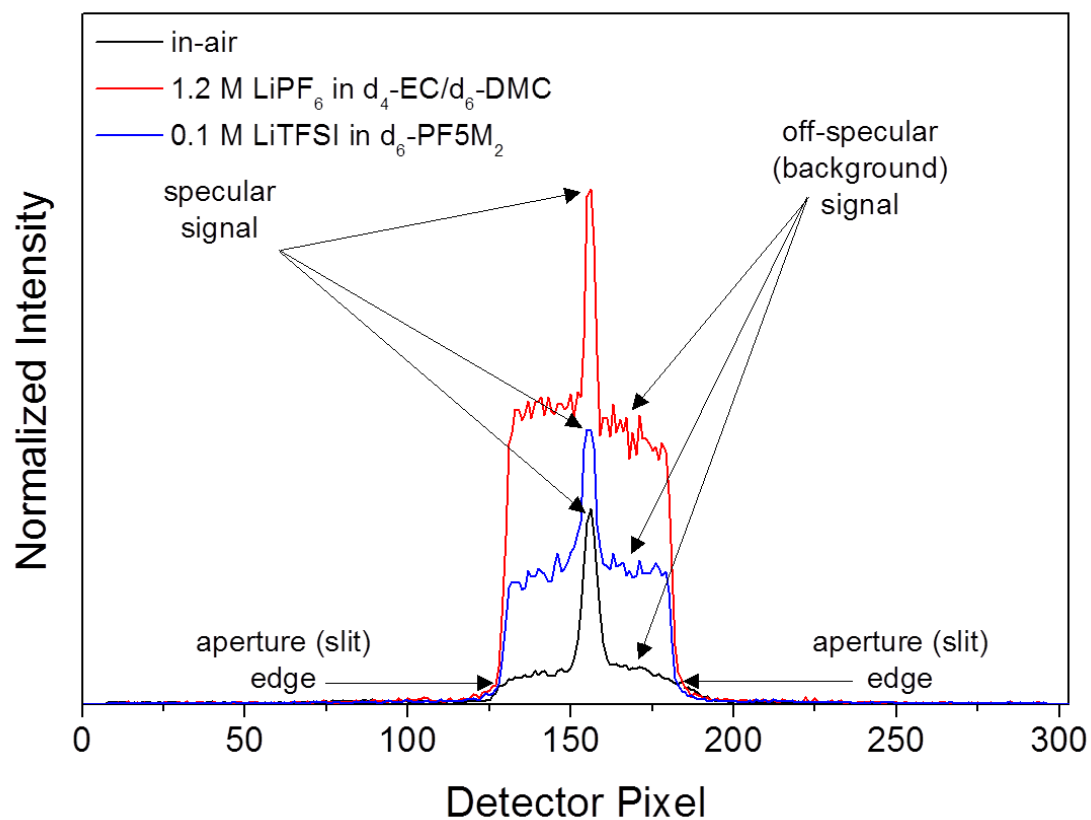


Fig. S1 High- Q NR data before background subtraction. This data demonstrates the low background signal of the PF5M₂ electrolyte as compared to a deuterated EC/DMC electrolyte.¹

Table S1. Multilayer parameters determined from NR fits. Values in italics were not varied independently during fitting.

Sample Voltage	Si SLD [10 ⁻⁶ Å ⁻²]	Interface Roughness [nm]	SiO ₂ Thickness [nm]	SiO ₂ SLD [10 ⁻⁶ Å ⁻²]	Interface Roughness [nm]	Cu Thickness [nm]	Cu SLD [10 ⁻⁶ Å ⁻²]	Interface Roughness [nm]	Si Electrode Thickness [nm]	Si Electrode SLD [10 ⁻⁶ Å ⁻²]	Interface Roughness [nm]	SEI Thickness [nm]	SEI SLD [10 ⁻⁶ Å ⁻²]	Interface Roughness [nm]	Electrolyte SLD [10 ⁻⁶ Å ⁻²]	χ^2
in-air	2.07	0.399	2.33	2.67	1.29	7.5	6.45	0.68	48.3	1.9	1.57				0 (air)	2.2
OCV	2.07	<i>0.399</i>	2.33	2.67	<i>1.29</i>	7.5	6.45	0.02 ± 0.02	48.4 ± 0.1	2.02 ± 0.02	2.3 ± 0.1				4.78	2.0
1.1 V	2.07	<i>0.399</i>	2.33	2.67	<i>1.29</i>	7.5	6.45	0.03 ± 0.02	48.3 ± 0.1	2.09 ± 0.02	2.3 ± 0.1				4.78	1.8
0.7 V	2.07	<i>0.399</i>	2.33	2.67	<i>1.29</i>	7.5	6.45	0.06 ± 0.04	48.9 ± 0.1	<i>2.04</i>	2.5 ± 0.1	14.4 ± 3.2	4.5 ± 0.1	6.6 ± 1.7	4.78	2.3
0.4 V	2.07	<i>0.399</i>	2.33	2.67	<i>1.29</i>	7.5	6.45	0.02 ± 0.03	50.5 ± 0.5	<i>1.93</i>	3.0 ± 0.5	16.7 ± 6.4	4.5 ± 0.2	6.9 ± 2.4	4.78	7.0
0.08 V	2.07	<i>0.399</i>	2.33	2.67	<i>1.29</i>	7.5	6.45	0.01 ± 0.03	106.0 ± 0.3	0.28	9.7 ± 0.6	26.6 ± 2.1	4.7 ± 0.1	5.1 ± 2.0	4.78	2.9
2.0 V	2.07	<i>0.399</i>	2.33	2.67	<i>1.29</i>	7.5	6.45	0.03 ± 0.03	65.4 ± 1.1	<i>1.21</i>	10.1 ± 1.3	34.2 ± 7.2	4.3 ± 0.3	8.6 ± 2.0	4.78	4.1
0.08 V	2.07	<i>0.399</i>	2.33	2.67	<i>1.29</i>	7.5	6.45	0.01 ± 0.03	105.9 ± 0.7	0.28	11.2 ± 1.1	27.3 ± 2.3	4.3 ± 0.1	11.1 ± 2.6	4.78	3.0
2.0 V	2.07	<i>0.399</i>	2.33	2.67	<i>1.29</i>	7.5	6.45	0.02 ± 0.04	66.9 ± 0.6	<i>1.16</i>	10.4 ± 0.7	32.2 ± 1.5	4.3 ± 0.1	8.2 ± 1.4	4.78	3.2
0.08 V	2.07	<i>0.399</i>	2.33	2.67	<i>1.29</i>	7.5	6.45	0.43 ± 0.02	105.5 ± 0.7	<i>0.29</i>	11.2 ± 0.8	28.6 ± 4.0	4.3 ± 0.1	11.9 ± 2.5	4.78	3.9

References

1. G. M. Veith, M. Doucet, J. K. Baldwin, R. L. Sacci, T. M. Fears, Y. Wang and J. F. Browning, *The Journal of Physical Chemistry C*, 2015, **119**, 20339-20349.

SECTION

2. CONCLUSION

The work included in Paper I and Papers II and III is difficult to reconcile within a single cohesive theme, indicative of the changes that occur over the course of a 5-year doctoral career. The project that resulted in Papers II and III (fluorinated neutron-transparent Li-ion battery electrolytes) arose organically from the project that resulted in Paper I (sol-gel vanadium oxide) through a series of projects (and funding sources) which have not yet yielded publishable results.

In the process of characterizing the materials formed in Paper I, one application stood out as particularly interesting (fundable): high-capacity Li-ion battery cathodes. A series of novel vanadium oxide and lithium vanadate nanomaterials could be synthesized in the lab, but structural characterization—especially the ever-desirable *in situ* studies—proved difficult. The co-refinement of (common) X-ray and (less-common) neutron diffraction data represented one promising solution; however, application of these techniques was more difficult than initially anticipated due to inherent complexity of both the structure of vanadium oxide systems and diffraction from highly anisotropic nanomaterials.

The desire to perform *in situ* studies of battery materials was ever-present and a functional electrochemical cell for *in situ* neutron diffraction was sufficiently novel to pique interest in an exploratory study on alternative neutron-transparent electrolytes. Unlike solving the structure of three-dimensional anisotropic vanadate nanoparticles, the synthesis and study of fluorinated, neutron-transparent Li-ion battery electrolytes showed immediate high-quality results. As such, focus shifted from solving the structure of

nanoparticulate vanadate cathode materials to the characterization of fluorinated ester electrolytes.

This path shows how the two projects included in this thesis, which share little in terms of subject or technique, arose naturally over the course of investigation.

VITA

Tyler Martin Fears was born in St. Charles, Missouri on May 13, 1987. In 2005 he began school at the University of Missouri-Rolla. As an undergraduate he was a member and officer of the Beta Alpha chapter of the Kappa Alpha Order fraternity. He also performed undergraduate research under Dr. Jeffrey G. Winiarz where he published a manuscript as first author. In 2010 he graduated the (now Missouri University of Science in Technology) with Bachelors of Science in Physics and in Chemistry.

In 2011, Tyler joined Dr. Winiarz's group as a Doctoral Student in Chemistry. He worked on the synthesis of transition metal aerogels under the purview of Dr. Nicholas Leventis. In 2013, he recieved a National Science Foundation Integrative Graduate Education and Research Traineeship (IGERT) to learn and apply neutron scattering to his research under Drs. Helmut Kaiser and Haskell Taub at the University of Missouri. In 2015, he recieved a Department of Energy Office of Science Graduate Student Research (SCGSR) fellowship to study solid-electrolyte interphases under Dr. Gabriel Veith at Oak Ridge National Laboratory.

Tyler successfully defended this doctoral thesis on August 14, 2015. In December, 2015, he received his Doctorate of Philosophy in Chemistry from the Missouri University of Science and Technology.